Report of Investigations 2010-1

TSUNAMI INUNDATION MAPS OF SEWARD AND NORTHERN RESURRECTION BAY, ALASKA

by
E.N. Suleimani, D.J. Nicolsky, D.A. West, R.A. Combellick, and R.A. Hansen

Published by
STATE OF ALASKA
DEPARTMENT OF NATURAL RESOURCES
DIVISION OF GEOLOGICAL & GEOPHYSICAL SURVEYS
2010

Report of Investigations 2010-1

TSUNAMI INUNDATION MAPS OF SEWARD AND NORTHERN RESURRECTION BAY, ALASKA

by
E.N. Suleimani, D.J. Nicolsky, D.A. West, R.A. Combellick, and R.A. Hansen

2010

STATE OF ALASKA
Sean Parnell, *Governor*

DEPARTMENT OF NATURAL RESOURCES
Tom Irwin, *Commissioner*

DIVISION OF GEOLOGICAL & GEOPHYSICAL SURVEYS
Robert F. Swenson, *State Geologist*
Rodney A. Combellick, *Acting Director*

Publications produced by the Division of Geological & Geophysical Surveys can be examined at the following locations. To order publications, contact the Fairbanks office.

Alaska Division of Geological & Geophysical Surveys
3354 College Rd., Fairbanks, Alaska 99709-3707
Phone: (907) 451-5020 Fax (907) 451-5050
dggspubs@alaska.gov
www.dggs.alaska.gov

Alaska State Library
State Office Building, 8th Floor
3354 College Road
Juneau, Alaska 99811-0571

Alaska Resource Library & Information Services (ARLIS)
3150 C Street, Suite 100
Anchorage, Alaska 99503

Elmer E. Rasmuson Library
University of Alaska Fairbanks
Fairbanks, Alaska 99775-1005

University of Alaska Anchorage Library
3211 Providence Drive
Anchorage, Alaska 99508

This publication released by the Division of Geological & Geophysical Surveys was produced and printed in Fairbanks, Alaska, at a cost of $44 per copy. Publication is authorized by Alaska Statute 41, which charges the division “to determine the potential of Alaskan land for production of metals, minerals, fuels, and geothermal resources; the location and supplies of groundwater and construction materials; the potential geologic hazards to buildings, roads, bridges, and other installations and structures; and shall conduct such other surveys and investigations as will advance knowledge of the geology of Alaska.”

CONTENTS

Abstract 1
Introduction 1
Project background: Regional and historical context 2
Setting 2
Tsunami waves in Resurrection Bay, Alaska, on March 27, 1964 3
Regional seismotectonics 6
Landslide Tsunami Hazard in Resurrection Bay 9
Methodology and data 10
Grid development and data sources 10
Numerical model of tsunami wave propagation and runup 12
Numerical model of landslide-generated tsunami waves 14
Tectonic tsunami sources 14
Source functions of the 1964 tsunami 14
Extended 1964 rupture 16
Tectonic tsunami scenarios 16
Scenario 1. Repeat of the 1964 event 16
Scenario 2. Modified 1964 event 16
Scenario 3. Modified 1964 event 18
Scenario 4. Hypothetical event 18
Landslide tsunami sources 21
Multiple submarine slope failures in Resurrection Bay during the 1964 earthquake 21
Landslide tsunami scenarios 22
Scenario 5. Waves generated by three major underwater slide complexes of the 1964 earthquake – Seward downtown slide, Lowell Point slide, and Fourth of July slide 22
Scenario 6. Hypothetical event: Simultaneous underwater slope failures at four locations where sediment accumulated since 1964 22
Scenario 7. Hypothetical event: Simultaneous underwater slope failures at four locations where sediment accumulated since 1964, with added sediment volumes 24
Modeling results 26
Numerical modeling of the 1964 tsunami in Resurrection Bay: Model verification 26
Results of hypothetical tsunami scenarios 26
Time series and other numerical results 29
Sources of errors and uncertainties 29
Summary 29
Acknowledgments 32
References 32

FIGURES

Figure 1. Map of southcentral Alaska with rupture zone of the 1964 Great Alaska Earthquake and segments of the Alaska–Aleutian megathrust 2
2. Location map of Seward in Resurrection Bay 3
3. Imagery of downtown Seward; photos taken before the earthquake of March 27, 1964, one day after the earthquake, and a recent satellite image 4
4. Bathymetry of Resurrection Bay, showing major fan deltas and creeks 5
5. Maximum observed tsunami runup in downtown Seward and at the head of Resurrection Bay 7
6. Earthquakes in southcentral Alaska 8
7. Telescoping embedded numerical grids for calculation of tsunami propagation and runup 11
8. Predicted water level plot for Seward on March 27, 1964 12
9. A diagram that relates different tidal datums and vertical tectonic land changes during and after the 1964 earthquake 13

10. Source function of the 1964 tsunami 15
11. Vertical coseismic displacements for the extended 1964 rupture model 17
12. Scenario 1. Source function of the 1964 tsunami 17
13. Scenario 2. Prince William Sound asperity of SDM 18
14. Scenario 3. Kodiak asperity of SDM 19
15. Geologic setting of the Yakutat block with major faults 19
16. Earthquakes in the vicinity of the Yakutat block 20
17. Scenario 4. Pamplona zone deformation model 21
18. Oblique image of Seward downtown, with offshore shaded-relief bathymetry 22
19. Distribution of initial thickness of the sliding mass 23
20. Scenario 5. The three major slides of the 1964 earthquake 24
21. Scenario 6. Accumulation areas with thicknesses and location of the S2G1 core 25
22. Observed 1964 inundation line and calculated inundation lines from tectonic and landslide sources at Seward 27
23. Observed 1964 inundation line and calculated inundation lines from tectonic and landslide sources at the head of Resurrection Bay 28
24. Maximum calculated drag force in the areas of Seward downtown, harbor, and airport for Scenario 1 30
25. Maximum calculated drag force in the areas of Seward downtown, harbor, and airport for Scenario 5 31

TABLES

Table 1. Nested grids used in the model to compute propagation of tsunami waves generated in the Gulf of Alaska to the city of Seward. The 15-m grid is used to compute the inundation 10
2. Fault parameters for the Yakataga–Yakutat segment 16
3. Fault parameters for scenario 4 21

APPENDIX

FigureA1-1. Locations of time series points 35

SHEETS

(in envelope)

Sheet 1. Tectonic tsunami inundation scenarios, Seward, Alaska
2. Landslide tsunami inundation scenarios, Seward, Alaska
3. Maximum estimated tsunami inundation, Seward, Alaska

Tsunami inundation maps of Seward and northern Resurrection Bay, Alaska

by
E.N. Suleimani[1], D.J. Nicolsky[1], D.A. West[1], R.A. Combellick[2], and R.A. Hansen[1]

Abstract

The purpose of this study is to evaluate tsunami hazard for the community of Seward and northern Resurrection Bay area, Alaska. This report will provide guidance to local emergency managers in tsunami hazard assessment. We used a numerical modeling method to estimate the extent of inundation by tsunami waves generated from earthquake and landslide sources. Our tsunami scenarios included a repeat of the tsunami of the 1964 Great Alaska Earthquake, as well as tsunami waves generated by two hypothetical Yakataga Gap earthquakes in northeastern Gulf of Alaska, hypothetical earthquakes in Prince William Sound and Kodiak asperities of the 1964 rupture, and local underwater landslides in Resurrection Bay. Results of numerical modeling combined with historical observations in the region are intended to help local emergency officials with evacuation planning and public education for reducing future tsunami risk.

INTRODUCTION

Alaska has the greatest earthquake and tsunami potential among the U.S. states. Figure 1 shows one of the most seismically active regions of the state, where the Pacific Plate is subducting under the North American Plate. This subduction zone, known as the Alaska–Aleutian megathrust zone, makes the adjacent coastal areas especially hazardous with regard to tsunami exposure. The coseismic crustal movements that characterize this area have a high potential for producing vertical sea floor displacements, which are highly tsunamigenic. Historic tsunamis that were generated by earthquakes on the Alaska–Aleutian subduction zone have resulted in widespread damage and loss of life along the Alaskan Pacific coast and other exposed locations around the Pacific Ocean. Large seismic events occurring in the vicinity of the Alaska Peninsula, Aleutian Islands, and Gulf of Alaska have a very high potential for generating both local and Pacific-wide tsunamis. Tsunamis originating in Alaska can travel across the Pacific Ocean and impact coastal areas hours after they are generated. However, these waves are considered to be a near-field hazard for Alaska, and can reach Alaskan coastal communities within minutes of the earthquake. Therefore, saving lives and property depends on how well a community is prepared, which makes it essential to estimate the potential flooding of the coastal zone in the case of a local or distant tsunami.

On March 27, 1964, the Prince William Sound area of Alaska was struck by the largest earthquake ever recorded in North America. This magnitude M_w9.2 megathrust earthquake generated the most destructive historic tsunami in Alaska and, farther south, impacted the west coast of the United States and Canada. Of the 131 fatalities associated with this earthquake, 122 were caused by tsunami waves (Lander, 1996). Although tragic, the number of deaths was fortunately far smaller than in the case of the 2004 Indian Ocean tsunami due to low population density on the Alaska coast. In addition to the major tectonic tsunami that was generated by displacement of the ocean floor between the trench and the coastline, more than 20 local tsunamis were generated by submarine and subaerial landslides in coastal Alaska. Local tsunamis caused most of the damage and accounted for 76 percent of tsunami fatalities. Also, they arrived almost immediately after the shaking was felt, leaving no time for warning or evacuation. The community of Seward in Resurrection Bay (fig. 2) suffered from the combined effects of local landslide-generated waves and the major tectonic tsunami that propagated from the main earthquake rupture zone in the Gulf of Alaska. The earthquake triggered a series of slope failures offshore of Seward, which resulted in landsliding of part of the coastline into the water, along with the loss of the port facilities. The town sustained great damage, and 12 people perished due to the tsunamis. During a future earthquake, underwater slides could be triggered almost instantaneously and tsunami waves could arrive without warning, as they did in 1964. Local tsunamis were responsible for most of the damage in Seward during the 1964 earthquake, thus the future potential of similar events must be evaluated for comprehensive inundation mapping.

To help mitigate the risk that earthquakes and tsunamis pose to Alaska coastal communities, the Alaska

[1]Alaska Earthquake Information Center, Geophysical Institute, University of Alaska, P.O. Box 757320, Fairbanks, Alaska 99775-7320
[2]Alaska Division of Geological & Geophysical Surveys, 3354 College Rd., Fairbanks, Alaska 99709-3707

Tsunami Mapping Team (ATMT) was created. It consists of personnel with the Geophysical Institute (GI) of the University of Alaska Fairbanks and the Alaska Division of Geological & Geophysical Surveys (DGGS). The ATMT participates in the National Tsunami Hazard Mitigation Program (NTHMP) by evaluating and mapping potential inundation of selected parts of the Alaska coastline using numerical modeling of tsunami wave dynamics. The communities are selected for inundation modeling in coordination with the Alaska Division of Homeland Security and Emergency Management (DHSEM) with consideration for location, infrastructure, availability and quality of bathymetric and topographic data, and community involvement.

The production of tsunami evacuation maps consists of several stages. First, we construct hypothetical tsunami scenarios on the basis of the parameters of potential underwater earthquakes and landslides. Next, we perform model simulations for each of the source scenarios. The results are compared with any observations from historical tsunamis in the region, if such data exist. Finally, numerical results and historical observations are combined to develop a realistic "worst case" inundation line for every community on a map. This inundation line encompasses the maximum extent of flooding based on model simulations of all source scenarios and historical observations, and becomes a basis for local tsunami hazard planning and creation of evacuation maps.

The Seward and Resurrection Bay tsunami inundation maps described in this report represent the results of the ongoing effort of state and federal agencies to produce inundation maps for many Alaska coastal communities.

In this report, we generally provide both metric and English units of measure. However, where we quote existing data, we report the data in the original units of measure without conversion. To convert kilometers to miles, multiply by 0.6214.

PROJECT BACKGROUND: REGIONAL AND HISTORICAL CONTEXT

SETTING

The town of Seward is near the northwestern corner of Resurrection Bay, about 200 km south of Anchorage (fig. 2). During the construction of the Alaska Railroad

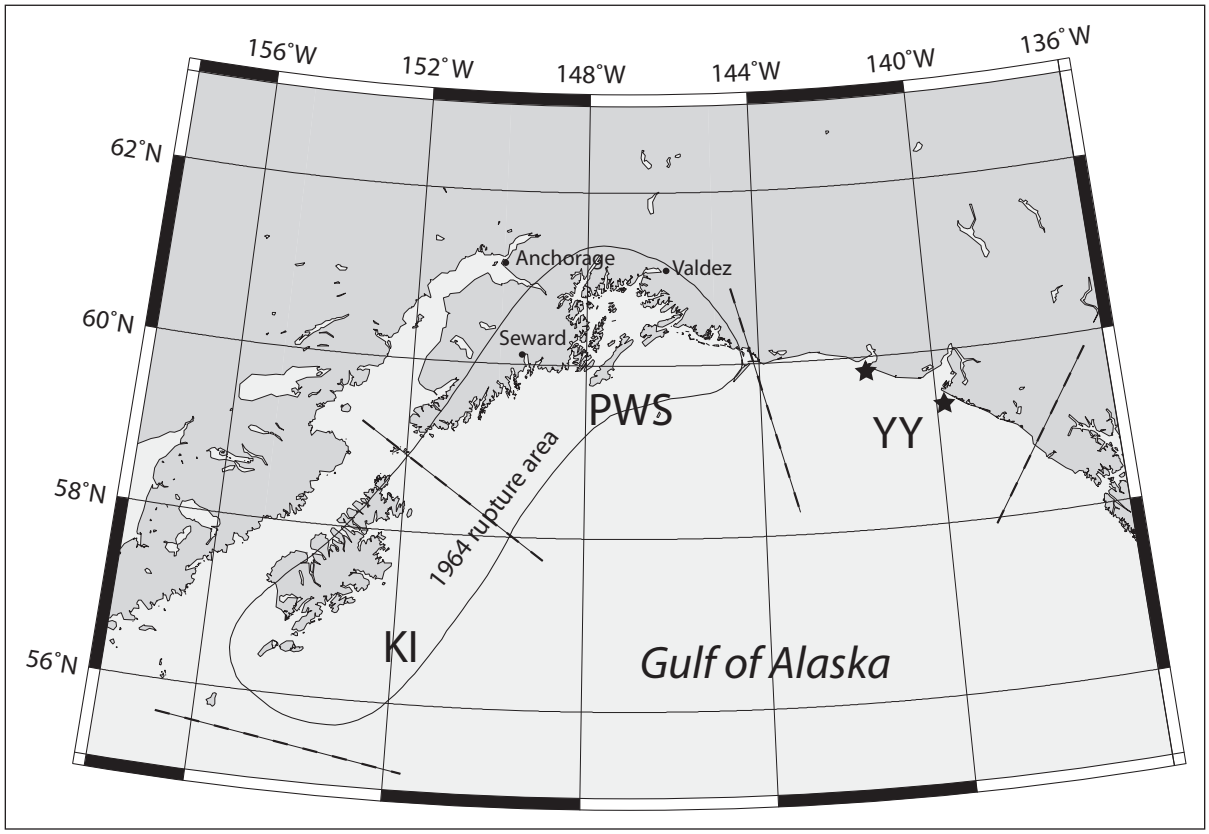

Figure 1. Map of southcentral Alaska with rupture zone of the 1964 Great Alaska Earthquake and segments of the Alaska–Aleutian megathrust: the Prince William Sound (PWS), the Kodiak Island (KI) and the Yakataga–Yakutat (YY) segments. Stars indicate epicenters of two earthquakes of September 1899.

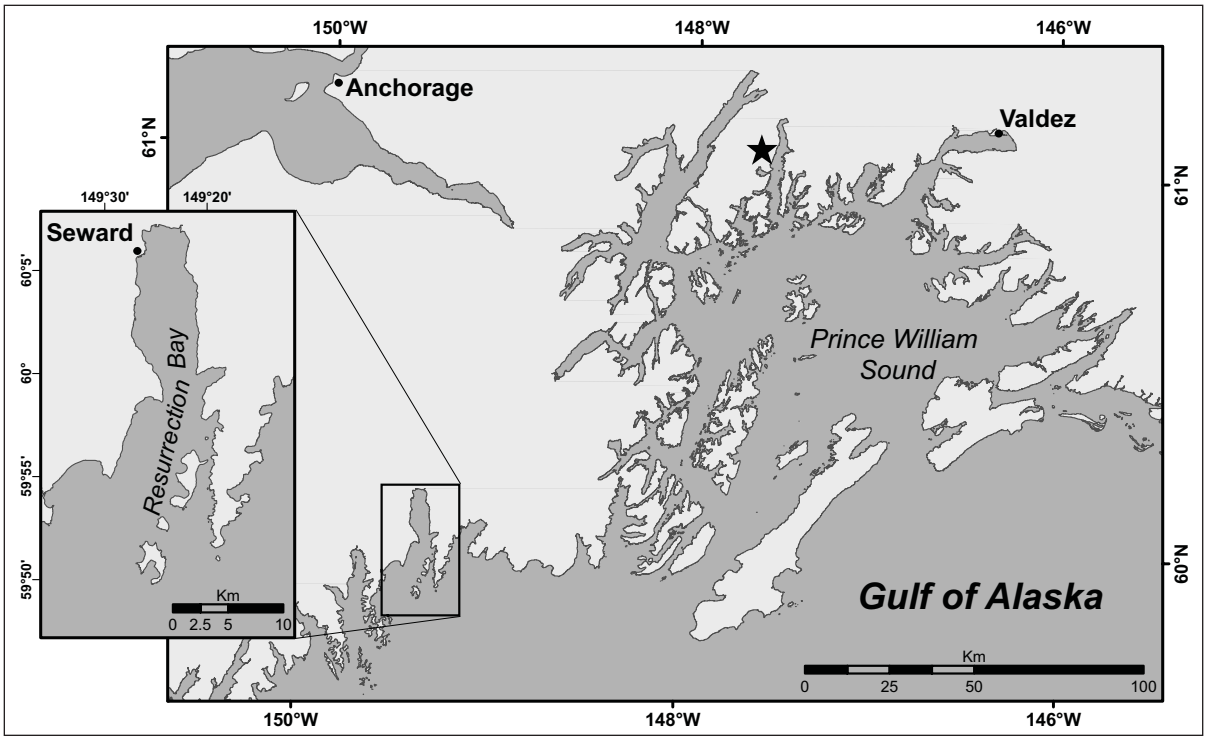

Figure 2. Location of Seward in Resurrection Bay. Star indicates initial epicenter of the 1964 Great Alaska Earthquake.

between 1915 and 1923, Seward became an ocean terminus and supply center for interior Alaska. The economy of Seward has long been dominated by transportation and supply services. At the time of the 1964 earthquake, the economy of Seward was based on shipping, and was heavily dependent on the city's railroad, harbor, and port operations. Seward was severely impacted by the 1964 earthquake and tsunami waves. The loss of harbor facilities from the earthquake and resultant offshore slope failures near the Seward waterfront devastated the economic base of the town (Lemke, 1967).

Seward has grown considerably since the 1964 earthquake. Its economy is more diversified and includes tourism, commercial fishing, and fish processing, as well as oil and gas development. Still, much of the economic activity and infrastructure is located on or near the coast, ports, and harbors. As an ice-free harbor, Seward is an important supply center for Interior Alaska and a port for the state ferry system. Every year, more than 320,000 cruise ship passengers visit the port city (Alaska Division of Community Advocacy, 2005). Figure 3 presents a sequence of Seward photos, taken before and after the 1964 tsunami, and then recently, in 2005. The red line indicates the maximum extent of inundation caused by the 1964 tsunami waves. The bottom image makes it clear that much of the economic and industrial base has been rebuilt in the area inundated by the 1964 tsunami.

Seward is built mostly on the alluvial fan of Lowell Creek. Lowell Point, Tonsina Point, and the area at the mouth of Fourth of July Creek (fig. 4) are also alluvial fans that extend into the bay as fan deltas (Lemke, 1967). The entire head of Resurrection Bay is a fjord-head delta, formed by Resurrection River. Haeussler and others (2007) use the term 'bathtub' to describe a flat depression in the middle of the bay extending north to south (fig. 4). The deepest part of the bathtub is approximately 300 m below sea level. Prior to the 1964 earthquake, the average offshore slopes in the vicinity of Seward ranged from 10 to 20 degrees, decreasing to 5 degrees at the depth of about 200 m (Lemke, 1967). Today, that same area has an average slope of about 25 degrees (Lee and others, 2006). A natural barrier formed by Caines Head and a glacial sill divide the bay into two deep basins, separated by a narrow 'neck' with maximum depth above the sill at 195 m. This sill inhibits sediment transport by tidal currents to the southern part of the bay (Haeussler and others, 2007). Our study focuses on the northern basin of Resurrection Bay, north of the sill area (fig. 4).

TSUNAMI WAVES IN RESURRECTION BAY, ALASKA, ON MARCH 27, 1964

The M_w9.2 Alaska earthquake of March 27, 1964, at Seward was characterized by strong ground motion that lasted 3–4 minutes. During the shaking, a section of the waterfront slid into the bay, taking with it docks and other harbor facilities. At the same time, fuel tanks fractured and oil ignited. Both local, landslide-generated waves

and distant, tectonically generated waves inundated the Seward shoreline and caused tremendous damage (Lemke, 1967). Damage from the strong ground motion alone was minor compared to tsunami-related destruction. As a result of regional tectonic deformation, the Resurrection Bay area subsided about 3.5 feet (1.1 m), which resulted in low-lying coastal areas being inundated at high tide. Thirteen people were killed and five injured in Seward as a combined result of the earthquake and tsunami waves. Eighty-six houses were totally destroyed and 269 were heavily damaged. According to Lemke (1967), the total cost to repair public and private facilities was estimated at $22 million ($153 million in 2009 dollars).

Several types of waves were observed in Resurrection Bay on March 27, 1964: landslide-generated waves, a tectonic tsunami wave train, and probably seiches (Wilson and Tørum, 1968), all resulting in a complicated wave pattern. The Seward tide gauge was positioned on a dock that collapsed into the bay as a result of massive submarine slope failures. The instrument was heavily damaged, and the record was lost. Although the sequence of waves was reconstructed from observations provided by eyewitnesses, there are uncertainties in the time estimates of wave arrivals (Wilson and Tørum, 1968). An initial drawdown of water was observed at the Seward waterfront about 30 seconds after the ground started to shake. At the same time, fuel tanks ruptured, leaked, and subsequently exploded; the tanks slid into the bay, and the receding water was covered with burning oil. The highest wave at Seward was about 6–8 m high, observed about 1.5–2 minutes after the shaking began. The tectonic tsunami wave, covered with burning oil, came into the bay about 25 minutes after the earthquake, spanning

Figure 3. Imagery of downtown Seward: top – aerial photo taken before the earthquake of March 27, 1964 (photo by the U.S. Army Corps of Engineers, mosaic by the USGS); middle - aerial photo taken one day after the earthquake of March 27, 1964 (photo by the U.S. Army Corps of Engineers, mosaic by the USGS); bottom – a recent satellite image of Seward (Digital Globe, 2005). Red line indicates the maximum extent of inundation caused by the 1964 tsunami waves.

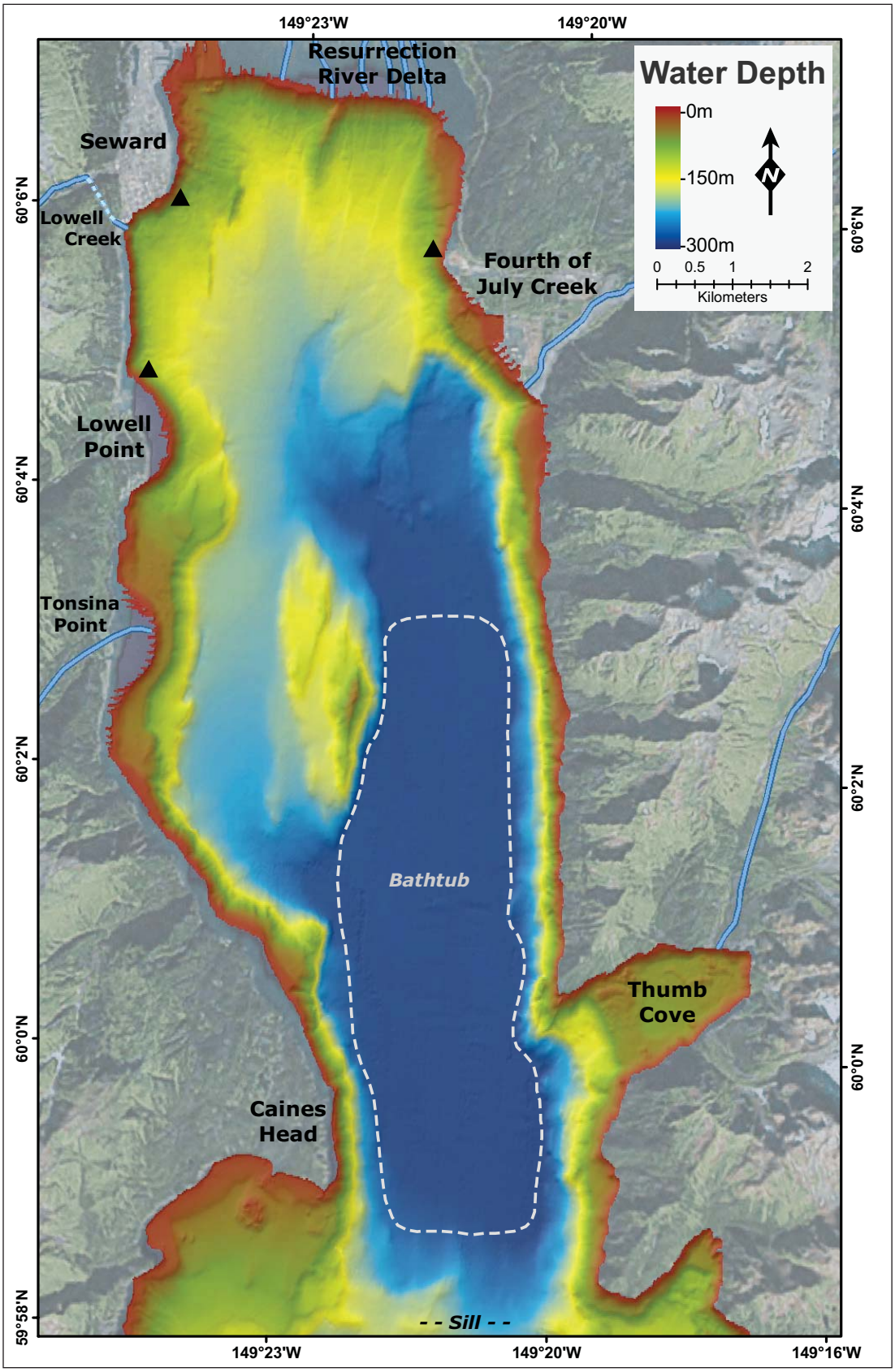

Figure 4. Bathymetry of Resurrection Bay, showing major fan deltas and creeks.

the entire width of the bay (Wilson and Tørum, 1968). This wave was similar in height to the initial landslide-generated waves but extended farther inland toward the river delta at the head of the bay than the local waves. Lemke (1967) summarized results of geologic investigations that were conducted in the Resurrection Bay area following the earthquake, and delineated the maximum observed tsunami inundation in downtown Seward and at the head of Resurrection Bay (fig. 5). The maximum inundation line at the city of Seward represents the combined effects from both the local landslide-generated waves and the major tectonic tsunami, while the observations of maximum runup at the head of the bay delineate the area that was flooded only by seismically generated waves.

Several researchers conducted geologic investigations in the Resurrection Bay area right after the earthquake (Lemke, 1967; Wilson and Tørum, 1968; Plafker and others, 1969; Shannon and Hilts, 1973). From these studies, it was concluded that strong ground motion during the earthquake caused several submarine slope failures along the Seward waterfront and other areas in upper Resurrection Bay. Hampton and others (2002) described the triggering mechanism as dynamic forces imposed by large seismic accelerations that added to the downslope component of the gravitational force on the steep slopes of the Lowell Creek and Resurrection River deltas. Hampton and others (2002) note that the stability of the sediment was also decreased by the low tidal level at the time of the earthquake, and by the rapid drawdown of water following the initial slope failure, which prevented the pore water from draining from the sediment quickly enough to maintain hydrostatic stability. The underwater slope failures generated large waves that were observed during ground shaking (Wilson and Tørum, 1968). The major factors that contributed to the total volume and aerial extent of the slide material were the long duration of ground motion (3 to 4 min), the configuration of underwater slopes, and the type of sediment forming these slopes—unconsolidated and fine-grained materials (Lemke, 1967). Hampton and others (1996) added that high artesian pressure within aquifers of the delta, combined with the extra load caused by waterfront artificial fill and shoreline development, also contributed to the slope failures. The authors summarized all the environmental loads in Resurrection Bay and concluded that although it was a unique combination of conditions, most of them had been documented separately during slope failures in other fjords.

REGIONAL SEISMOTECTONICS

Resurrection Bay occupies an area of very high seismic activity in southcentral Alaska (fig. 1). Tectonic regime is dominated by the convergence of the Pacific and North American plates, which interact along the Aleutian Megathrust (Page and others, 1991). The convergence rate is approximately 56 mm/yr (2.2 in/yr) (DeMets and others, 1990). Resurrection Bay is close to the northeast end of the Aleutian Megathrust, where the megathrust is strongly coupled and has a shallow dip angle of about 7 degrees. This zone has the potential to produce some of the largest earthquakes in the world, as demonstrated by the magnitude M_w9.2 Great Alaska Earthquake of 1964 (fig. 1). These plate motions also have the potential to drive significant seismicity in both the overriding plate and the subducting slab (Doser and Brown, 2001).

Freymueller and others (2000) used GPS measurements of the crustal motions to study the deformation of the region and model the plate interactions. They found that under the eastern portion of the Kenai Peninsula and in Prince William Sound, the plates are nearly completely locked, while under the western portion of the Kenai Peninsula the plates are freely slipping. This correlates with Doser and Brown's (2001) findings that the central and southern Kenai Peninsula has been seismically quiet at the $M_w > 5$ level since the 1964 event, while the Prince William Sound area has continued to have seismic activity similar to that occurring before the 1964 earthquake.

Figure 6 plots seismicity in southcentral Alaska with locations taken from the Alaska Earthquake Information Center catalog. The events with moment magnitude less than 6 are shown as small dots and color-coded according to depth, and the red box indicates the location of the region of interest. Prior to installation of the seismic network in Alaska in the early 1970s, only relatively larger events were reliably located ($M > \approx 6$). After installation of the network, events of much smaller sizes were regularly located.

Shennan and others (2008) presented geologic evidence of six prehistoric great earthquakes in the Kenai Peninsula area of southcentral Alaska in the past 4,000 years (seven including 1964), based on radiocarbon ages of tidal marsh deposits at Girdwood. Their evidence indicates that recurrence intervals for great earthquakes in this area range from a minimum of 180–720 years to a maximum of 790–920 years. On the basis of all published paleoseismic data for the region, Carver and Plafker (2008) calculated that the average median recurrence interval for great earthquakes in the Prince William Sound segment of the eastern Aleutian seismic zone over this period is 589 years.

According to the segmentation model of Nishenko and Jacob (1990), southcentral Alaska includes three segments of the megathrust: the Yakataga–Yakutat (YY), Prince William Sound (PWS), and Kodiak Island (KI) segments (fig. 1). The YY segment at the eastern end of the megathrust represents a complex collision zone where the Yakutat microplate moves northwest toward

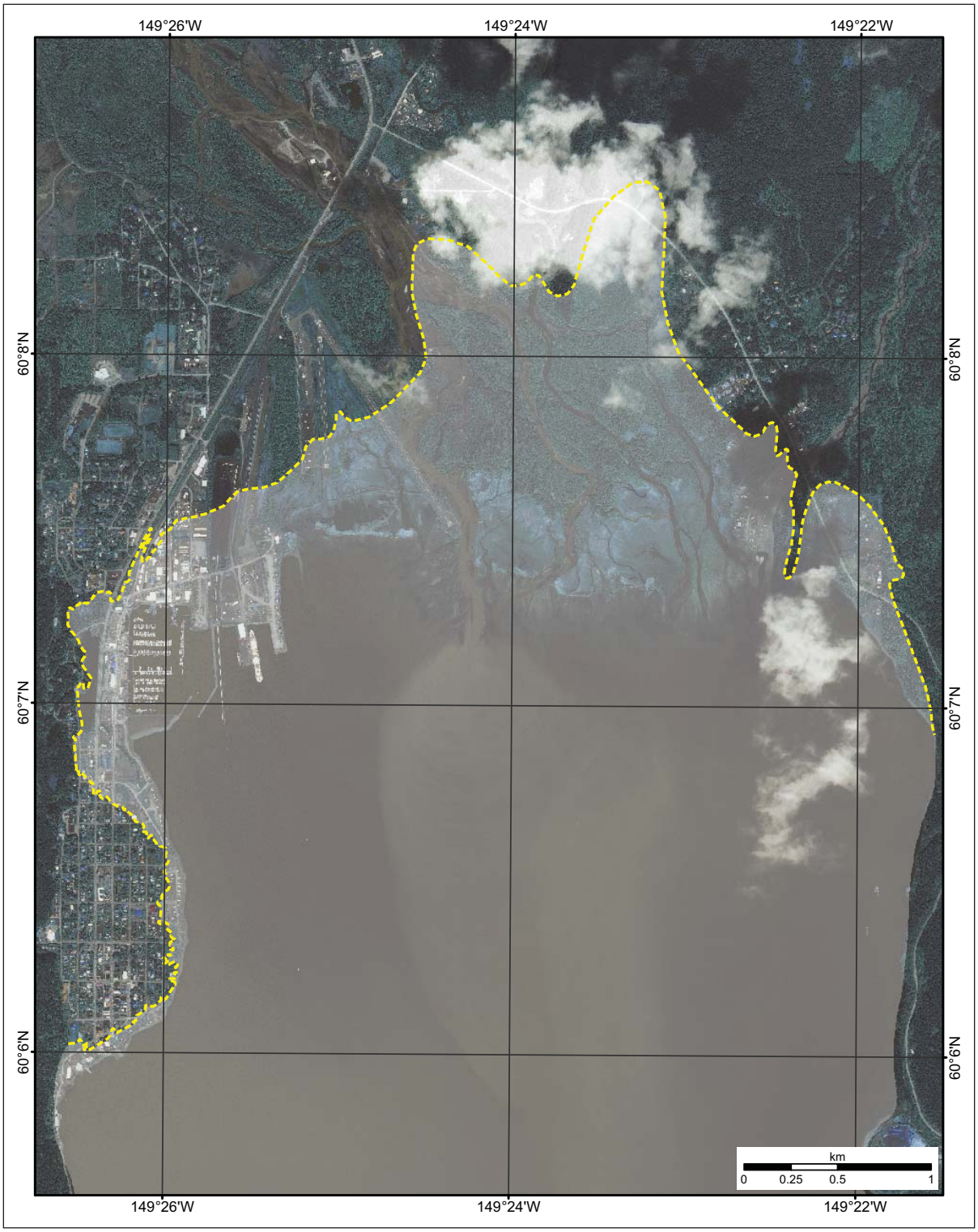

Figure 5. Maximum observed tsunami runup in downtown Seward and at the head of Resurrection Bay in 1964 (from Lemke, 1967).

central Alaska at 48 mm/yr (Carver and Plafker, 2008). This segment translates the predominantly strike-slip motion east of it to shallow-dipping subduction to the west (Nishenko and Jacob, 1990). The interaction between the Yakutat block and the Pacific and North American plates is complex and not well characterized. The southern and eastern boundaries of the Yakutat block are well defined, but a collection of distributed fold and thrust zones, splay faults, and regions of mountain building complicates the northern and western edges of the block. Plafker and Thatcher (2008) reevaluated the mechanisms of the two great Yakutat Bay earthquakes of September 1899 (fig. 1) and showed that coseismic deformation was mostly uplift and onshore, which explained the absence of tsunami in the Gulf of Alaska. There were several local tsunamis observed in bays and fjords that were triggered by submarine slides and collapses of glacier walls. Plafker and Thatcher (2008)

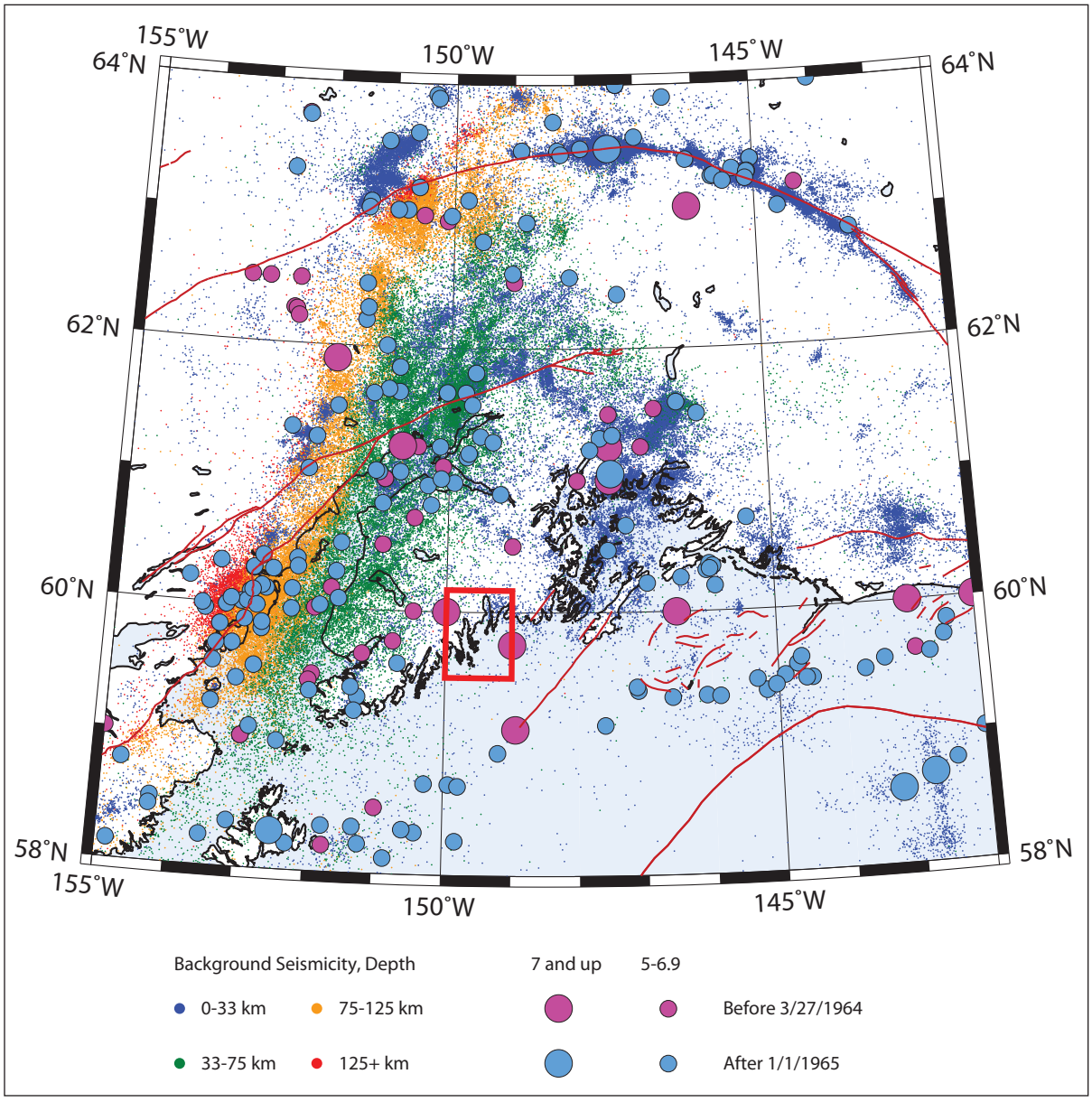

Figure 6. Earthquakes in southcentral Alaska, from the Alaska Earthquake Information Center catalog. The red rectangle delineates the computational grid of 8-arc-second resolution surrounding Resurrection Bay. Small dots correspond to earthquakes with magnitude less than 5. Large circles show significant earthquakes (magnitude 5 and greater) before (purple) and after (light blue) the Great Alaska Earthquake of March 27, 1964. The main shock and aftershocks of this event are not included in the plot.

concluded that the 1899 earthquake sequence most likely did not fill the offshore portion of the Yakataga seismic gap between the 1964 rupture area and the focal area of the 1899 earthquakes. This finding suggests that the YY segment has a high potential for a future tsunamigenic earthquake.

In the paleoseismic study of regional land subsidence at Kenai Peninsula sites, Hamilton and Shennan (2005) estimated coseismic subsidence during the 1964 earthquake and two earlier events. It was shown that the earthquake dated to ~1500–1400 cal. yr BP produced more than two times the subsidence caused by the 1964 earthquake. By comparing the Kenai Peninsula sites with other sites around Cook Inlet, the authors found that each of the three great earthquakes in the study had a unique pattern of coseismic subsidence. This result demonstrates that understanding the most recent great earthquake in the area is not sufficient for comprehensive tsunami hazard assessment in southcentral Alaska, and detailed studies of multiple great earthquakes are required. The recent work by Shennan and others (2008) tests the hypothesis that in some seismic cycles megathrust segments can combine, as proposed in the segmentation model by Nishenko and Jacob (1990), and produce earthquakes greater than any in the recorded history. The paper presents paleoseismic evidence that earthquakes ~900 and ~1,500 yr BP simultaneously ruptured three adjacent segments of the Aleutian Megathrust: the PWS and KI segments, and the Yakutat microplate (the YY segment). The rupture area of these earthquakes was calculated to be 23,000 km^2 greater than that of the 1964 earthquake, with a 15 percent increase in seismic moment. The authors suggested that increase in seismic moment is less significant than increased tsunami potential of this multi-segment rupture, due to coseismic uplift over a large area of shallow continental shelf off the Yakataga coast. We built a hypothetical tsunami source function for the extended rupture and performed a numerical modeling experiment to estimate the impact of tsunami waves generated by this event at Seward. The source function and modeling results are described in section 4 of "Methodology and data."

LANDSLIDE TSUNAMI HAZARD IN RESURRECTION BAY

Resurrection Bay is a deep glacial fjord, typical of many in southcentral and southeastern Alaska. Kulikov and others (1998) analyzed tsunami catalog data for the North Pacific coast and showed that this region has a long recorded history of tsunami waves generated by submarine and subaerial landslides, avalanches, and rockfalls. The authors also found that, in the majority of cases, tectonic tsunamis that arrive in bays and fjords from the open ocean have relatively small amplitudes, but a great number of local landslide-generated tsunamis have much larger wave amplitudes. For example, as a result of the 1964 earthquake, about 20 local submarine and subaerial landslide tsunamis were generated in Alaska (Lander, 1996). Following the earthquake, Seward was the only place hit by both landslide-generated tsunamis and a major tectonic tsunami (Haeussler and others, 2007), while several other communities experienced only locally generated waves (Plafker and others, 1969). Kulikov and others (1998) also noted that, due to the sparse population of the area, the actual number of historical landslide tsunami events is unknown, and probably much greater than the number of events observed or recorded. Bornhold and others (2001) addressed the problem of estimation of hazard from landslide-generated tsunami waves for the coast of Alaska and British Columbia. They outlined specific features of long-term prediction of landslide-generated tsunamis at selected sites, and developed an approach for estimating tsunami hazard. The long-term approach consists of two steps: (1) analysis of historical events and verification of model results with runup observations at the site, and (2) numerical simulation of hypothetical tsunami scenarios. Although for many communities historical observations do not exist, Seward is an exception. The effects of the 1964 earthquake and tsunami waves in Resurrection Bay, including wave amplitudes and extent of inundation, are well documented (Lemke, 1967; Wilson and Tørum, 1968) and are ideal for numerical modeling studies.

Tsunamis caused by submarine slope failures are a serious hazard in glacial fjords of coastal Alaska where rapidly deposited sediments accumulate on steep underwater slopes (Lee and others, 2006). Bornhold and others (2001) identify earthquakes, extreme low tides, and construction activities in ports and harbors as the most common triggering mechanisms for underwater slope failures. Estimation of landslide tsunami risk for a coastal community requires assessment of locations of potential underwater failures using high-resolution bathymetry, actual physical parameters of the underwater materials, and an adequate numerical model. The most probable locations of unstable sediment bodies in Resurrection Bay are the underwater slopes of the Resurrection River delta, and abnormally steep submarine slopes located elsewhere in the bay (Lee and others, 2006).

Engineering studies conducted after the 1964 earthquake (Lemke, 1967; Coulter and Migliaccio, 1966; Shannon and Hilts, 1973) showed that additional onshore and submarine landslides can be expected along the Seward waterfront in the event of another large earthquake, and that sediment from the Resurrection River and smaller creeks will continue to accumulate on underwater slopes of Resurrection Bay. These studies also concluded that underwater slope failures have not

improved slope stability, meaning that the same slopes could fail again during a large earthquake. Moreover, some of the streams draining into Resurrection Bay, such as Lowell Creek and Fourth of July Creek, have been rerouted by humans. These creeks are now depositing sediments in new locations, which may lead to new unstable sediment accumulations and future submarine slides.

The recent results of sediment chemistry monitoring in Port Valdez, located in a glacial fjord setting similar to that of Resurrection Bay (fig. 2), demonstrated high sediment accumulation rates of about 1.5 cm/yr at the head of the fjord (Savoie and others, 2006). Sediment could be released not only by the ground shaking due to an earthquake, but also by other triggering events, such as extreme low tide conditions and construction activities. Because short-term prediction of landslide tsunamis is not practical for tsunami hazard assessment (Bornhold and others, 2001), we will use the long-term approach for estimating local tsunami hazard at Seward. The most essential components of this approach are numerical modeling of historical landslide tsunami events, and simulation of future hypothetical underwater slope failures.

METHODOLOGY AND DATA

GRID DEVELOPMENT AND DATA SOURCES

To support inundation modeling of coastal areas in Alaska, we use a series of nested telescoping grids, or digital elevation models (DEMs), as input layers for tsunami inundation modeling and mapping. These grids of increasing resolution allow us to propagate waves, generated by both distant and local sources, to Resurrection Bay. In order to propagate a wave from its source to various coastal locations we use embedded grids, placing a large, coarse grid in deep water and coupling it with smaller, finer grids in shallow water areas. This embedding technique allows us to dramatically increase resolution in the area where inundation calculations are performed, and save computational resources by using lower resolution grids in the deep ocean region. The extent of each grid used for Seward mapping is shown in figure 7 and table 1. The coarsest resolution 2-arc-minute grid (see table 1 for grid spacing) spans the Gulf of Alaska, while the highest resolution 15 m grid is restricted to upper Resurrection Bay. This grid is used for Seward inundation mapping; it also includes Lowell Point and Fourth of July Point (fig. 4). In this grid, the seamlessly combined bathymetric and topographic data allow for calculation of tsunami inundation of previously dry land.

The grids used for modeling were gathered from three sources:

15-m Grid: This "high resolution" grid contains bathymetric and topographic data merged into one DEM. It was developed by Labay and Haeussler (2008) from the following input surveys:

- Low-altitude LIDAR (Light Detection and Ranging) topography collected for the Kenai Watershed Forum in 2006
- U.S. Army Corps of Engineers (USACE) harbor soundings for the Seward City Marina and surroundings collected in 2006
- Multibeam bathymetric surveys of Resurrection Bay, conducted by NOAA's National Ocean Service (NOS) in 2001

Survey data were first adjusted to a common Mean High Water vertical datum before being combined into one ESRI point feature class. Where available, the more recent USACE harbor data were used in place of 2001 NOS survey data to represent the significant reconstruction of the harbor infrastructure between 2001 and 2006. Significant gaps between the survey areas were then filled in using interpolation routines. Topographic data in this grid are a combination of the 2006 LIDAR collection in the northern part of the bay, and the 10-m USGS DEM in the rest of the area, which was not covered by

Table 1. Nested grids used in the model to compute propagation of tsunami waves generated in the Gulf of Alaska to the city of Seward. The 15-m grid is used to compute the inundation.

Resolution	Spacing along longitude at 60°N	Spacing along latitude	West–East boundaries	North–South boundaries
2 arc-minutes	1,850 m	3,700 m	138°00'W – 169°00'W	52°00'N – 63°00'N
24 arc-seconds	370.5 m	741 m	147°00'W – 155°00'W	55°00'N – 62°00'N
8 arc-seconds	123.5 m	247 m	149°00'W – 150°00'W	59°30'N – 60°10'N
3 arc-seconds	48.5 m	97 m	149°14'W – 149°37'W	59°42'N – 60°10'N
15 meters	15 m	15 m	149°16'W – 149°27'W	59°57'N – 60°09'N

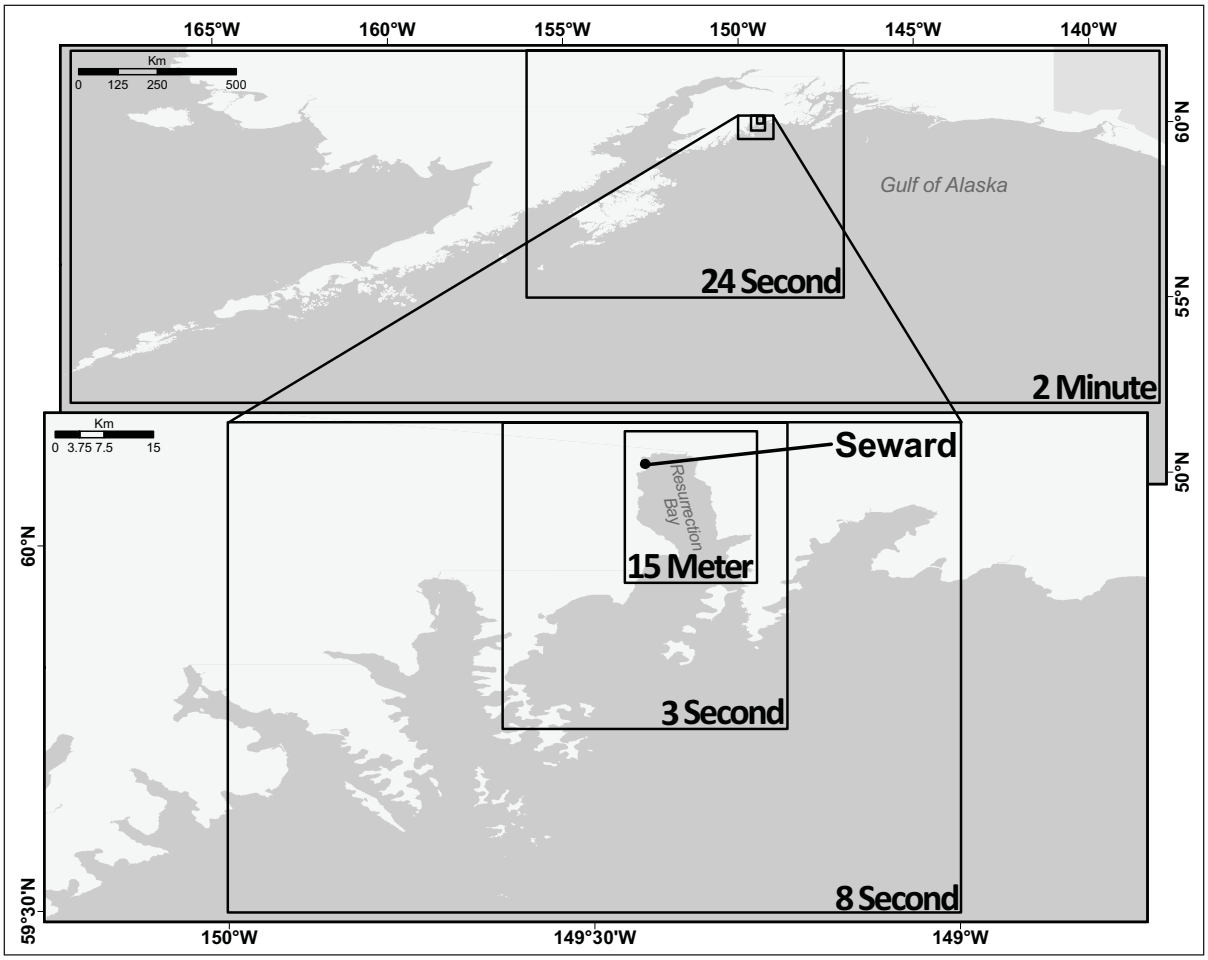

Figure 7. Telescoping embedded numerical grids for calculation of tsunami propagation and runup.

LIDAR. The northern section of the bay contains the most significant population and infrastructure centers. The resulting seamless dataset was exported and delivered in ESRI digital raster and ASCII xyz format with 15 m resolution.

3-Arc-Second, 8-Arc-Second and 24-Arc-Second Grids: Angie Venturato of the Pacific Marine Environmental Laboratory, National Oceanic & Atmospheric Administration (PMEL/NOAA) constructed these grids using bathymetry collected from NOS survey and chart data as well as shoreline data from USACE and Alaska Railroad surveys. These input surveys represent a variety of collection methods over a wide timescale from 1972 to 2004. Root mean squared error (RMSE) applies to systematic and random errors in the dataset and is used to define the vertical accuracy of these grids. The accuracy of bathymetric soundings is generally expected to be within 2 percent of depth.

The surveys were first converted into ESRI-compatible point data formats before depths were adjusted to Mean High Water from their respective origin vertical datums. The surveys were then clipped to a standard shoreline vector before being merged through the creation of a triangular irregular network (TIN). This compiled TIN dataset was used to export directly from ArcView 3.2 software into ASCII xyz format.

2-Arc-Minute Grid: This grid was created by Robert Kamphaus of PMEL/NOAA. Bathymetry for the Gulf of Alaska level extent was extracted directly from the publicly available ETOPO2 data set (NOAA, National Geophysical Data Center).

One of the challenges in near-field modeling of tsunami waves generated by a historic earthquake is to account for coseismic and post-seismic tectonic land changes, and also for a difference between the datum of the numerical grid and the stage of tide at the time of the earthquake. The high-resolution numerical grid of combined bathymetry and topography data for Resurrection Bay by Labay and Haeussler (2008) was referenced to the tidal datum of Mean High Water (MHW). Accord-

ing to observations (Lemke, 1967), tide was low at the time of the main shock. Low tide was one of the major factors that contributed to the large scale of landsliding, but at the same time helped to lessen the amount of damage from the first tectonic wave that arrived on low tide. Figure 8 is a predicted water-level plot at Seward on the day of the earthquake, obtained from NOAA tide calculator. It shows that the first tectonic wave arrived on the local minimum of the tidal curve, which corresponds to 0.175 m below Mean Lower Low Water (MLLW). The time mark 20:00 actually corresponds to 7 pm local time in Seward on March 27, 1964, since the State of Alaska moved to a different time zone in 1983 (one hour ahead).

Different tidal datums and tectonic land changes at Seward are demonstrated in figure 9. We call tidal range (TR) the difference between MHW and MLLW, and 'tide' is the sea level at the time of the earthquake. The landmass in the Seward area experienced coseismic subsidence (CS) of about 1.15 m (Lemke, 1967); as a result, many areas that were never flooded by tides before the earthquake are now under water. Larsen and others (2003) analyzed relative sea level changes from tide gauge records at 15 sites along the Pacific–North American plate boundary in southcentral Alaska, to determine vertical crustal motions in the period from 1937 to 2001. In several years immediately following the earthquake, the Seward site showed oscillatory uplift, and then uplift rates increased steadily thereafter. From their analysis, the total postseismic uplift (PU) at Seward could be estimated at about 20 cm. The following equation therefore provides the relationship between the water depth in Resurrection Bay at the time of the earthquake, H_{EQ}, and the present water depth, H_{now}, which was measured in 2001 by NOAA multibeam bathymetry survey:

$$H_{EQ} = H_{now} - TR - tide - CS + PU$$

By using the adjusted vertical datum in the bathymetry grid, the numerical model will reproduce the effects of tsunami inundation occurring at Seward under conditions close to those that were present at the time of the 1964 earthquake.

NUMERICAL MODEL OF TSUNAMI WAVE PROPAGATION AND RUNUP

Recently, NOAA published a technical memorandum that outlines major requirements for numerical models used in inundation mapping and tsunami forecasting, and describes a procedure for model evaluation (Synolakis and others, 2007). There are two major components in this process. The first is model validation, which is ensuring that the model solves equations of motion correctly by comparing model results with known solutions. This is achieved through analytical and laboratory benchmarking. The second component is model verification, which is testing the model, using observations of real events through field data benchmarking. The numerical

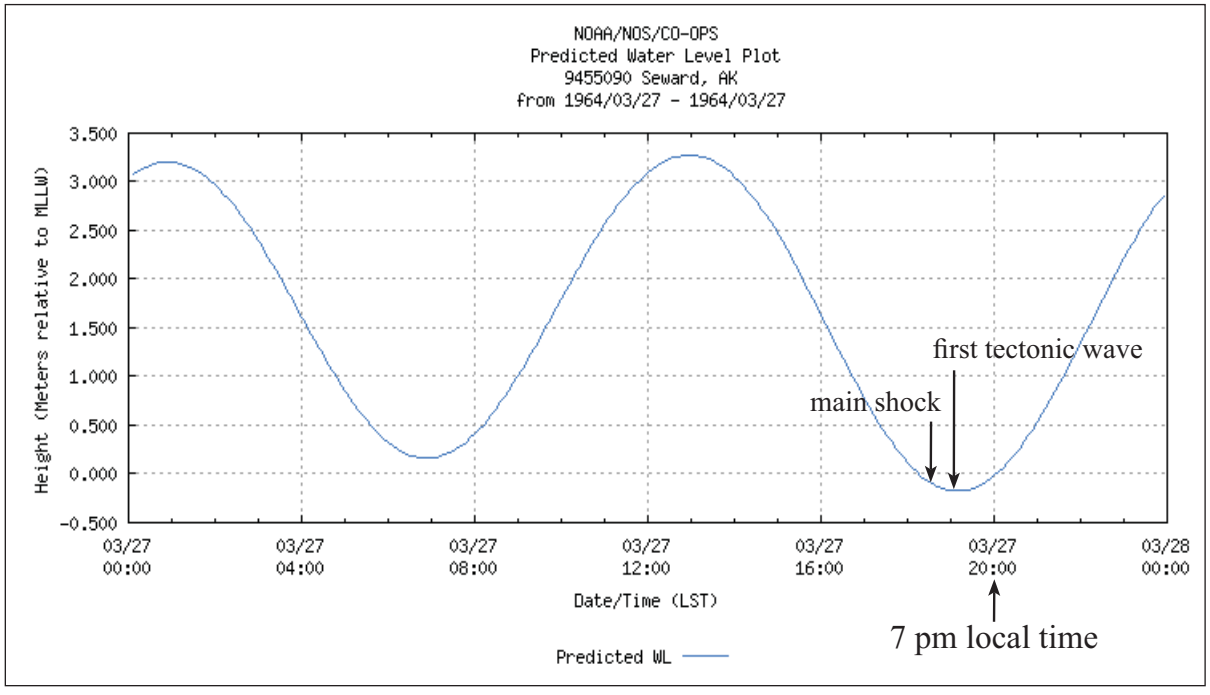

Figure 8. Predicted water level plot for Seward on March 27, 1964. Time is Local Standard Time (UTC-9); arrows indicate times of the main shock of the 1964 earthquake, and arrival of the first tectonic wave.

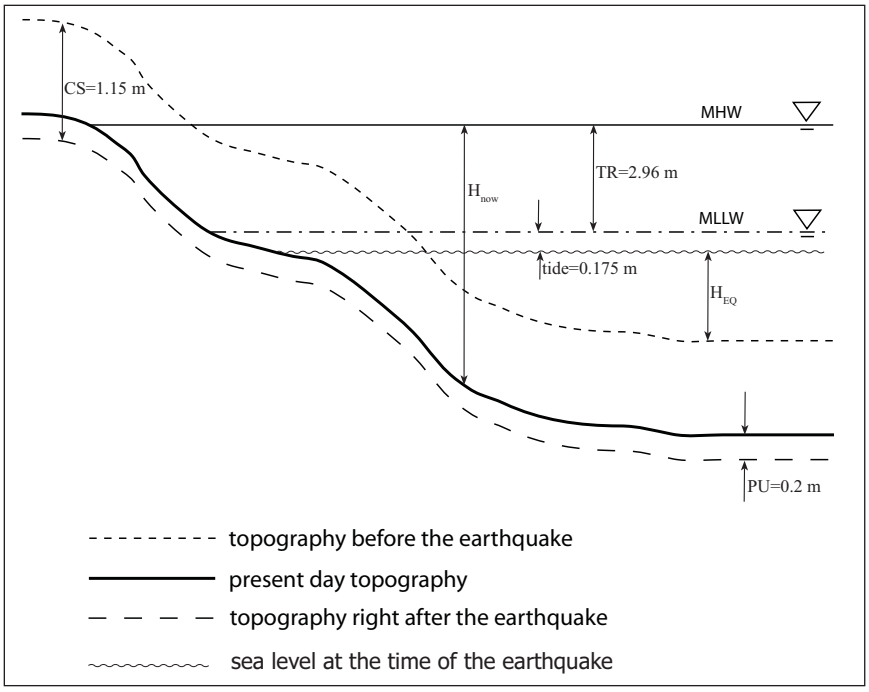

Figure 9. A diagram that relates different tidal datums and vertical tectonic land changes during and after the 1964 earthquake.

model currently used by AEIC for tsunami inundation mapping has been validated through a set of analytical benchmarks, and tested against laboratory and field data (Nicolsky and others, in press). The model solves nonlinear shallow water equations using a finite-difference method on a staggered grid. For any coarse–fine pair of computational grids, we apply an explicit-in-time numerical scheme as follows. First, we compute the water flux (WF) in a coarse-resolution grid. These values of WF are used to define the WF on a boundary of the fine-resolution grid. Consequently, the sea surface height (SSH) and then the WF are calculated in the fine-resolution grid. Finally, the SSH computed in the fine-resolution grid is used to define the SSH within the area of the coarse-resolution grid that coincides with the fine grid. Despite the fact that developed nested grids decrease the total number of grid cells and preserve an accuracy of computations within certain regions of interest, real life simulations are still prohibitive if parallel computing is not implemented. We use Portable Extensible Toolkit for Scientific computation (PETSc) which provides sets of tools for the parallel numerical solution of shallow-water equations. In particular, each computational grid listed in table 1 can be subdivided between an arbitrary number of processors. The above-mentioned passing of information between WF and SSH is implemented efficiently using PETSc subroutines.

We assess hazard related to tectonic and landslide-generated tsunamis in Resurrection Bay by performing model simulations for each hypothetical earthquake and landslide source scenario. In the output of the numerical model, each of the grid points has either a value of 0 where no inundation occurs or 1 if seawater reaches the grid point at any time. The inundation line approximately follows the 0.5 contour between these 0 and 1 point values but was adjusted visually to accommodate obstacles or local variations in topography that are not represented by the DEM. Although the location of the inundation line has an accuracy of approximately plus or minus 15 m horizontally relative to the grid spacing, the true location accuracy is unknown because the lines are the result of a complex modeling process whose accuracy depends on many factors. These factors include suitability of the earthquake source model, accuracy of the bathymetric and topographic data, and the adequacy of the numerical model in representing the generation, propagation, and run-up of tsunami waves. We did not attempt to adjust the modeled inundation limits to account for these uncertainty factors.

There are several limitations of the model. It does not take into account the periodic change of sea level due to tides. We conducted all model runs using bathymetric data that correspond to Mean High Water (MHW), with the exception of numerical modeling of the 1964 tsunami for the purpose of model validation. Those runs were conducted using the stage of tide at the time of the earthquake, approximately Mean Low Water. For the generation mechanism, we modeled earthquakes and landslides as potential sources of tsunami waves. In this region it was important to include landslide tsunami sources, because underwater landslides and the resulting tsunamis caused a significant portion of the damage in Resurrection Bay during the 1964 Great Alaska Earthquake.

NUMERICAL MODEL OF LANDSLIDE-GENERATED TSUNAMI WAVES

To simulate tsunami waves produced by multiple underwater slope failures in Resurrection Bay on March 27, 1964, we used a three-dimensional numerical model of a viscous underwater slide with full interactions between the deforming slide and the water waves that it generates. This model was initially proposed by Jiang and LeBlond (1992). Fine and others (1998) improved the model by including realistic bathymetry, and by correcting errors in the governing equations. The model's assumptions and applicability in simulating underwater mudflows are discussed by Jiang and LeBlond (1992, 1994) in their formulation of the viscous slide model. The model uses long-wave approximation for water waves and the deforming slide, which means that the wavelength is much greater than the local water depth, and the slide thickness is much smaller than the characteristic length of the slide along the slope (Jiang and LeBlond, 1994). Assier-Rzadkiewicz and others (1997) argued that the long-wave approximation could be inaccurate for steep slopes, which are slopes greater than 10 degrees. Rabinovich and others (2003) studied the validity of the long-wave approximation for slopes greater than 10 degrees and found that for a slope of 16 degrees the possible error was 8 percent, and for the maximum slope in their study (23 degrees), the possible error was 15 percent. Based on this analysis, for the average pre-earthquake offshore slopes that ranged from 10 to 20 degrees in the vicinity of Seward, the possible error introduced by a slide moving down these higher gradient slopes could be around 10 percent.

The advantage of this vertically integrated model, which includes two horizontal dimension effects, is its ability to simulate real landslide tsunami events using high-resolution numerical grids based on multibeam bathymetry data. Although model runs require the use of high-performance computing, the computational times are still reasonable. This model was successfully applied to simulate tsunami waves in Skagway Harbor, Alaska, generated by a submarine landslide on November 3, 1994 (Fine and others, 1998; Thomson and others, 2001). The results of numerical simulations were in good agreement with the tide gauge record in Skagway Harbor, one of the numerous fjords in southeastern Alaska. Rabinovich and others (2003) simulated potential underwater landslides in British Columbia fjords with settings similar to Resurrection Bay, and demonstrated that this model can be used for tsunami-hazard assessment.

TECTONIC TSUNAMI SOURCES

SOURCE FUNCTIONS OF THE 1964 TSUNAMI

The 1964 Great Alaska Earthquake generated one of the most destructive tsunamis ever observed in Alaska and the northwestern Pacific coast. This major tectonic tsunami was generated in the trench and upper plate fold and thrust belt area of the subduction zone (Plafker and others, 2000) and affected many communities in Alaska. Both the Prince William Sound and the Kodiak Island segments ruptured in the 1964 earthquake, producing the area of surface deformation of about 285,000 km^2 (Plafker, 1969). Christensen and Beck (1994) demonstrated that there were two areas of high moment release, representing the two major asperities of the 1964 rupture zone: the PWS asperity with an average slip of 18 m, and the KI asperity with an average slip of 10 m. Analysis of historical earthquake data in PWS and KI segments (Nishenko and Jacob, 1990) showed that the KI segment produced both large and great earthquakes more frequently and also independently of the PWS segment.

The 1964 tsunami was studied in depth by several investigators (Plafker, 1967; Wilson and Tørum, 1968; Lemke, 1967); observed inundation patterns for a number of Alaska communities are available for model calibration. We use a displacement of the ocean surface that results from an underwater earthquake as the initial condition for calculation of tsunami propagation. The amplitude of this initial disturbance is one of the major factors that affect the runup amplitudes along the shoreline. The fault parameters required to compute sea floor deformation are location of the epicenter, area, dip, rake, strike, and amount of slip on the fault. In all model runs, the initial topography was modified to account for residual seismic deformation of land due to the earthquake. We assumed that the initial displacement of the ocean surface from the equilibrium position was equal to vertical displacement of the ocean floor due to the earthquake rupture process. The model does not take into account the propagation of the moving rupture along the fault. We assumed here that the bottom movement was instantaneous. The model propagates the initial sea surface displacement from the source to coastal locations through a set of embedded grids of increasing resolution.

In this study we used two coseismic deformation models of the 1964 earthquake (Johnson and others, 1996; Suito and Freymueller, 2009) to generate the initial sea surface disturbance caused by vertical displacements of the sea floor during the earthquake. The following abbreviations will be referenced throughout this report: JDM, for deformation model by Johnson and others (1996) and SDM, for deformation model by Suito and Freymueller (2009).

A detailed analysis of the 1964 rupture zone was presented by Johnson and others (1996) through joint inversion of far-field tsunami waveforms and geodetic data. The authors derived a detailed slip distribution for the 1964 earthquake, which has eight subfaults representing the Kodiak asperity and nine subfaults in the Prince

William Sound asperity. One subfault was assigned to represent the Patton Bay fault, although contribution of this fault to the far-field tsunami waveforms was negligible. We used the equations of Okada (1985) to calculate distribution of coseismic uplift and subsidence resulting from this slip distribution. Then we used the derived surface deformation (fig. 10) as the initial condition for the tsunami propagation model. The source function based on JDM was previously applied to calculation of 1964 tsunami inundation in Kodiak and Kachemak Bay communities. The results are described in Suleimani and others (2002, 2005).

Plafker (1967) gives a detailed description of the motion observed on the Patton Bay fault during the Great Alaska Earthquake of 1964. He provides a full report of surface rupture and fault motion, as well as several pieces of evidence suggesting that the fault continues on the ocean floor well past the region where it is currently mapped. Holdahl and Sauber (1994) applied Plafker's description to construct their model of the Patton Bay fault, which was used in an inversion of geodetic data. Johnson and others (1996) used the results of Holdahl and Sauber to augment their joint inversion of geodetic and tsunami data. These two studies used only the mapped extent of the fault, approximately 72 km, despite significant evidence that the fault may extend much farther to the southwest.

Suito and Freymueller (2009) developed a new coseismic deformation model of the 1964 earthquake, which is based on a three-dimensional viscoelastic model, incorporating a realistic geometry with an elastic slab having very low dip angle. This coseismic model is not based on an inversion, but it resembles the recently published inversion model (Ichinose and others, 2007) and past proposed models (Holdahl and Sauber, 1994; Johnson and others, 1996; Santini and others, 2003). The main difference between JDM and SDM is that the SDM predicts slightly higher slip near the downdip end of the rupture to explain horizontal displacements. Additionally, the rupture in the SDM is assumed to occur at greater depths than in the JDM. As a result, the deeper subfaults in the SDM produce smoother variations of sea floor deformation than in the JDM. Both models use the Patton Bay fault to explain the excessive uplift at Montague Island (Plafker, 1967). It is assumed in the JDM that the extent of the splay fault was not much larger than its subaerial outcrop on Montague Island. In contrast, the SDM assumes that the Patton Bay splay fault extended much farther to the west than previously assumed by Holdahl and Sauber (1994) and Johnson

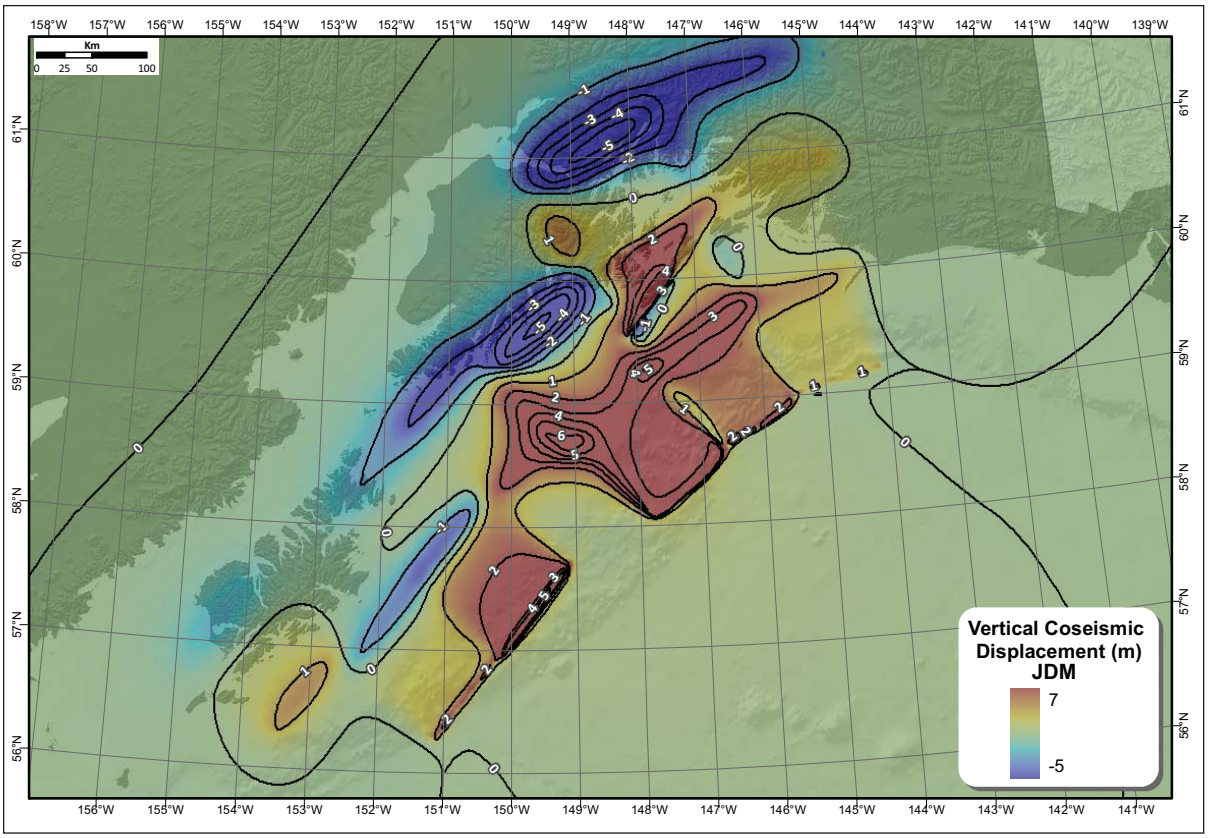

Figure 10. Source function of the 1964 tsunami based on Johnson and others (1996) (JDM).

and others (1996). Although the Patton Bay fault slipped approximately 10 m at the southwestern tip of Montague Island, there have been no comprehensive submarine surveys documenting the extent of that splay fault. Suito and Freymueller (2009), however, found that they could not fit all the GPS data accurately unless they extended the fault past the end of the Kenai Peninsula.

Results of numerical modeling of Seward inundation using the JDM source function vastly overestimate the observed 1964 inundation (see "Modeling results", section 1), therefore we use SDM in the tsunami scenarios that represent the 1964 event.

EXTENDED 1964 RUPTURE

A recent study by Shennan and others (2008) presents geologic evidence that the Prince William Sound and Kodiak Island segments of the 1964 rupture area and a portion of the Yakutat microplate may rupture simultaneously (see discussion in "Regional seismotectonics"). In order to evaluate whether this event would make a plausible future tsunami scenario for Seward, we have constructed a source function of the extended 1964 rupture. We applied the following constraints based on the hypothetical earthquake model of Shennan and others (2008):

- The extended source function includes three segments of the Aleutian Megathrust: the PWS, KI, and YY segments (fig. 1);
- The rupture area is about 23,000 km^2 greater than that of the 1964 earthquake;
- The total seismic moment is 15 percent greater than that of the 1964 earthquake;
- The new source function produces coseismic vertical uplifts along the Gulf of Alaska coastline segment between the Copper River basin and Yakataga, to match the coseismic deformation pattern to paleoseismic data (Shennan and others, 2008).

We have constructed a rupture model for the Yakataga–Yakutat segment using the constraints described above. The model consists of four subfaults with the fault parameters listed in table 2. We calculated coseismic deformations produced by this segment using Okada's algorithm (Okada, 1985), and then superposed them with the 1964 coseismic deformations produced by the SDM. The resulting coseismic deformation pattern for the extended 1964 rupture is shown in figure 11.

Results of numerical modeling of Seward inundation using the extended 1964 rupture model are not different from the inundation caused by the 1964 deformation model. Waves generated by the uplift of the sea floor in the area of Yakutat block arrive at Resurrection Bay much later than the wave generated in the PWS segment that arrives first and produces the maximum inundation zone.

TECTONIC TSUNAMI SCENARIOS

Scenario 1. Repeat of the 1964 event: Source function based on coseismic deformation model by Suito and Freymueller (2009) (SDM).

This source function represents the entire rupture area of the 1964 earthquake, with vertical coseismic deformations derived from the SDM (fig. 12).

Christensen and Beck (1994) demonstrated that there were two areas of high moment release, representing the two major asperities of the 1964 rupture zone: the Prince William Sound asperity with an average slip of 18 m, and the Kodiak asperity with an average slip of 10 m. The results of joint inversion of tsunami and geodetic data from the 1964 earthquake (Johnson and others, 1996) support the division of the rupture zone into two different segments, the Kodiak block and the Prince William Sound (PWS) block. These zones have different recurrence intervals, with estimates of the recurrence interval for the Kodiak segment being as low as 60 years (Johnson and others, 1996). Therefore we consider these two segments of the 1964 rupture area to be separate hypothetical tsunami source scenarios. We also consider a third hypothetical event involving the rupture of the Pamplona deformation zone, which represents another source of tsunami waves capable of reaching Resurrection Bay.

Scenario 2. Modified 1964 event: Prince William Sound asperity of the SDM.

This source function represents the Prince William Sound asperity from the deformation model by Suito and Freymueller (2009). Vertical coseismic deformations for this scenario are shown in figure 13.

Table 2. Fault parameters for the Yakataga–Yakutat segment

Lat [deg. N]	Lon [deg. W]	Depth [km]	Length [km]	Width [km]	Strike [deg.]	Dip [deg.]	Rake [deg.]	Slip [m]
59.17	144.12	1	50.1	190	256	12	90	15
59.36	143.23	3	51.1	141	250.4	10	90	15
59.54	142.42	5	47.8	114.8	245.8	6	90	15
59.94	141.21	5	79.7	99.6	237.8	8	90	15

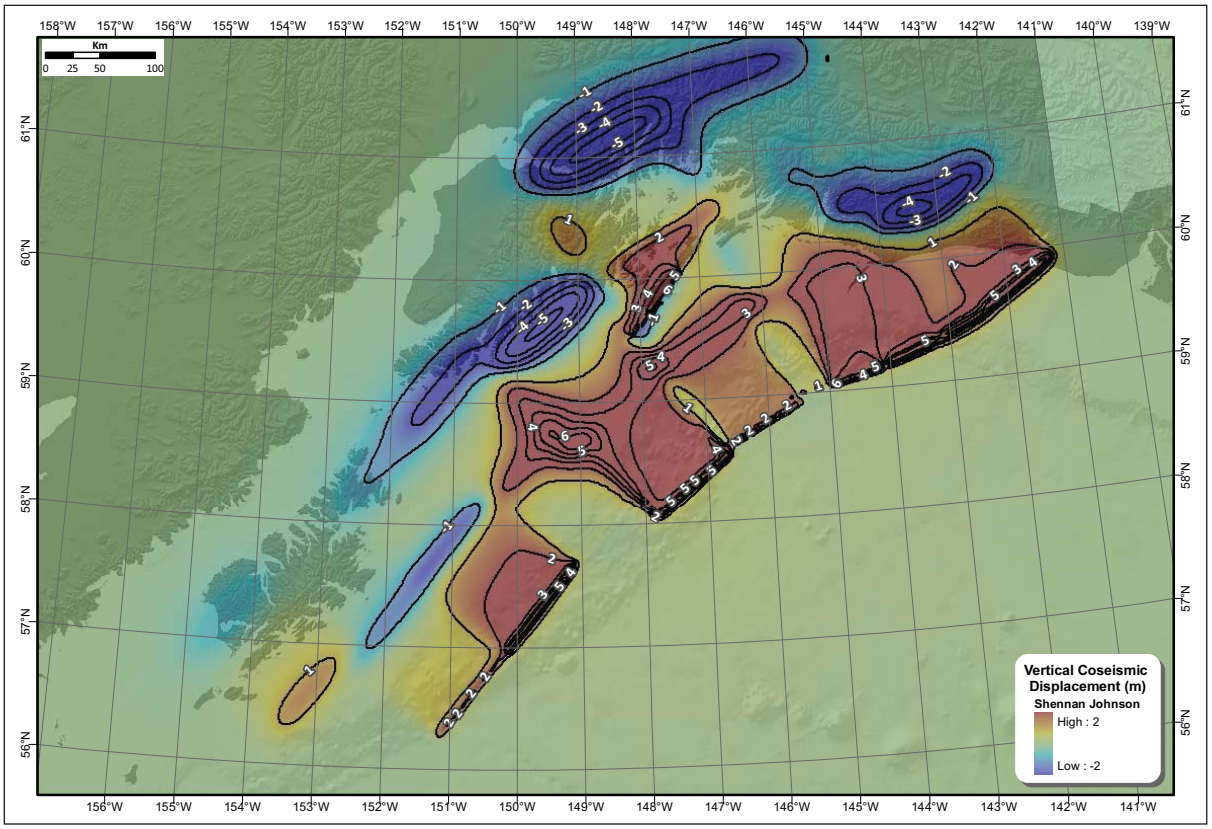

Figure 11. Vertical coseismic displacements for the extended 1964 rupture model.

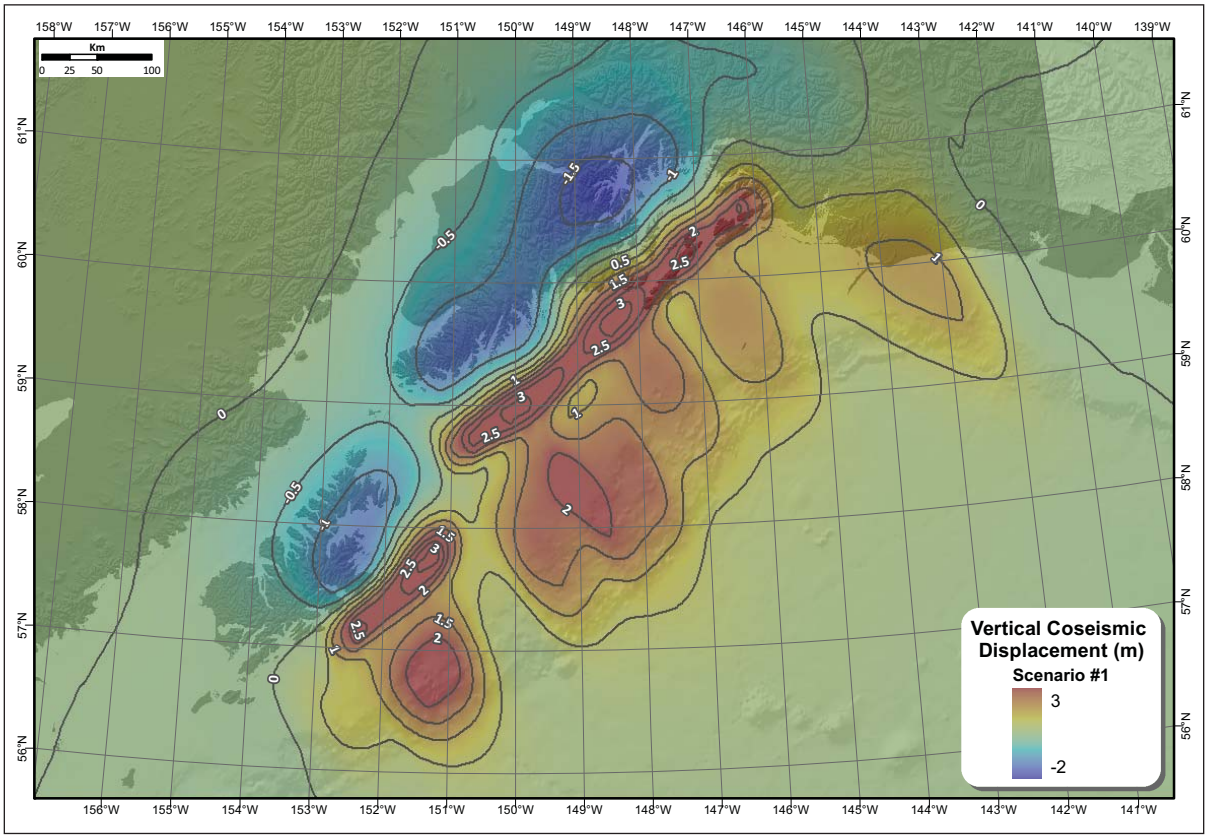

Figure 12. Scenario 1. Source function of the 1964 tsunami based on Suito and Freymueller (2008) (SDM).

Scenario 3. Modified 1964 event: Kodiak asperity of the SDM.

This source function represents the Kodiak asperity from the deformation model by Suito and Freymueller (2009). Vertical coseismic deformations for this scenario are shown in figure 14.

Scenario 4. Hypothetical event: Rupture of the Pamplona zone between the Yakutat block and the North American Plate.

This is a hypothetical earthquake that ruptures the Pamplona zone between the Malaspina fault and the Aleutian megathrust at the northwestern edge of the Yakutat block in a thrust event (fig. 15).

The Pamplona zone is a region of distributed fold and thrust features near the northwestern edge of the Yakutat block (fig. 15). There is a trend of moderate to strong historic seismicity in the area between the location of the 1979 M_w7.2 St. Elias earthquake and the end of the 1964 rupture zone (shown in fig. 16). This seismic zone is aligned with the Malaspina thrust fault and is well oriented to accommodate convergence between the Yakutat block and North American plate. Sauber and others (1997) identified this as the region most likely to rupture and fill the Yakataga seismic gap. Sauber and Molnia (2004) showed that the retreat of glaciers in the Wrangell Mountains increases the likelihood of seismic release on thrust faults in the region. We consider a hypothetical M_w ~8.8 event with fault parameters detailed in table 3. The vertical coseismic deformations for this scenario are shown in figure 17.

The Kodiak inundation mapping study (Suleimani and others, 2002) includes a scenario that represents a distant tsunami source, the Cascadia subduction zone rupture. The results of numerical modeling demonstrated that the major part of the tsunami energy will be directed west and southwest, toward Hawaii, and a very limited amount toward coastlines of Alaska. In this study, we performed numerical simulation of tsunami waves generated by a M_w9.2 earthquake in the Cascadia subduction zone. The results were consistent with those in the Kodiak report. Since this scenario produced negligible inundation at Seward, we did not include it in the list of tectonic scenarios.

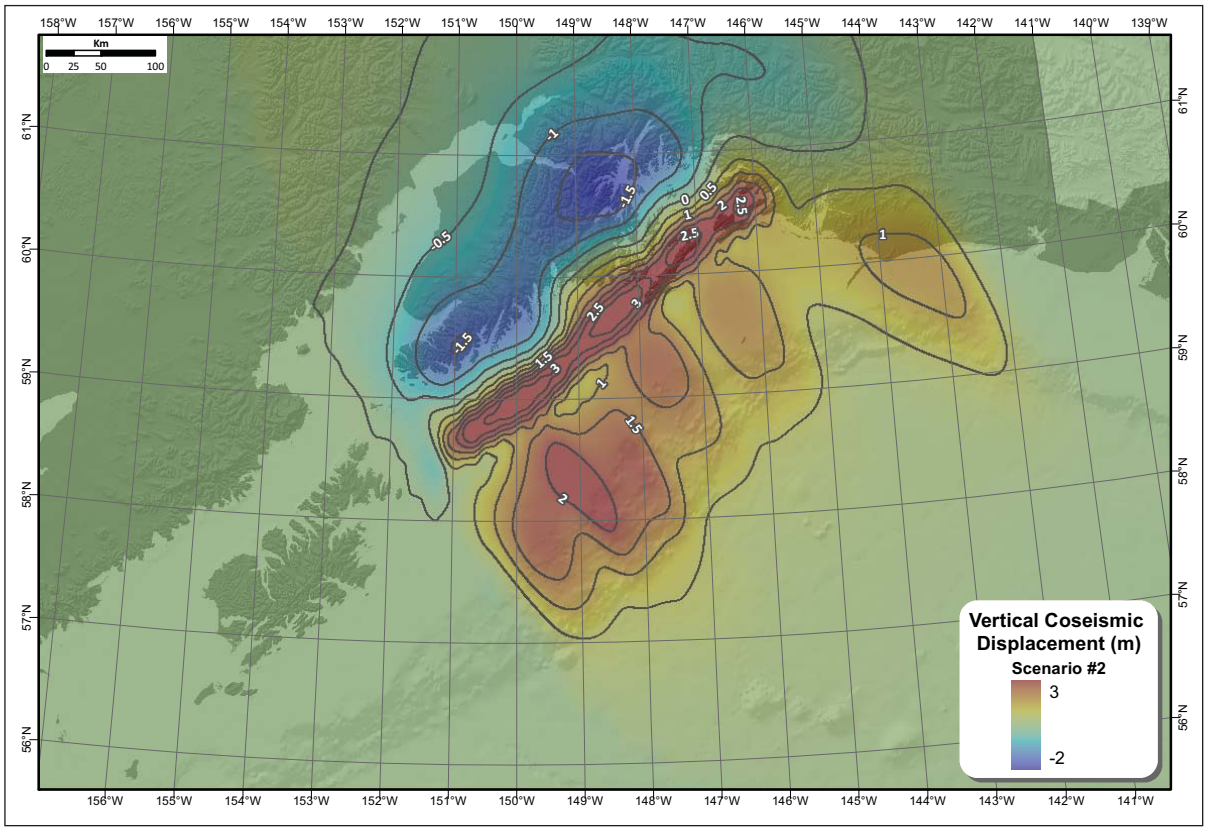

Figure 13. Scenario 2. Prince William Sound asperity of SDM.

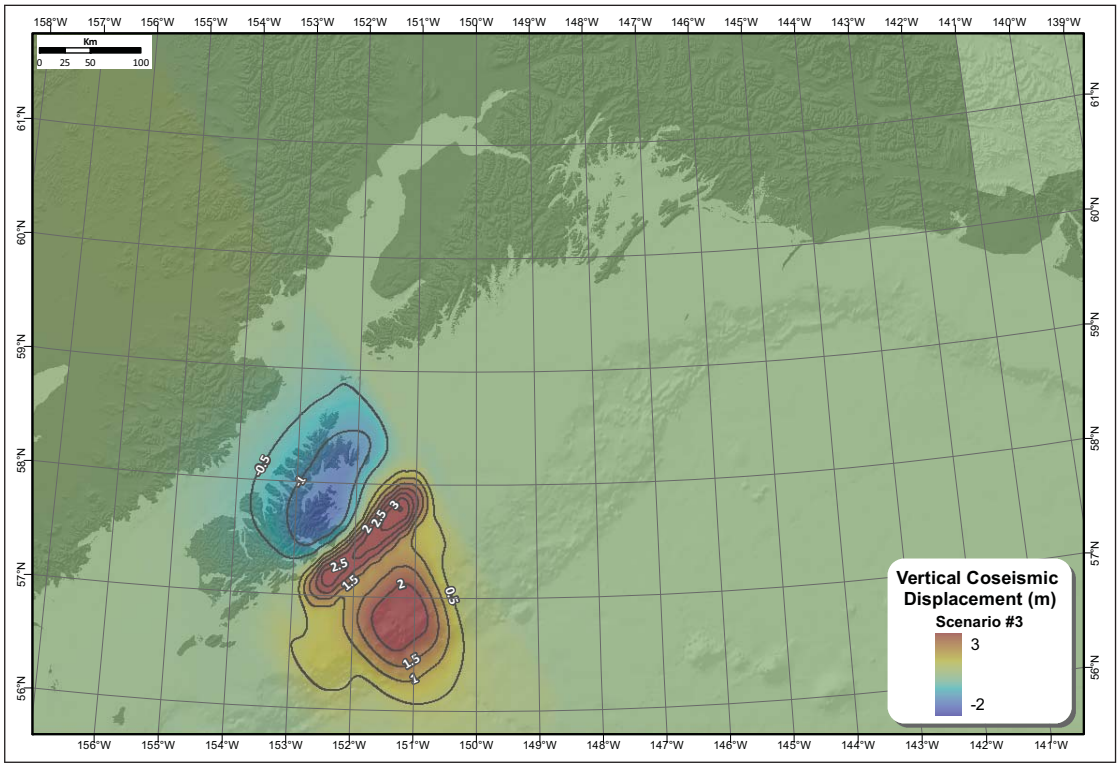

Figure 14. Scenario 3. Kodiak asperity of SDM.

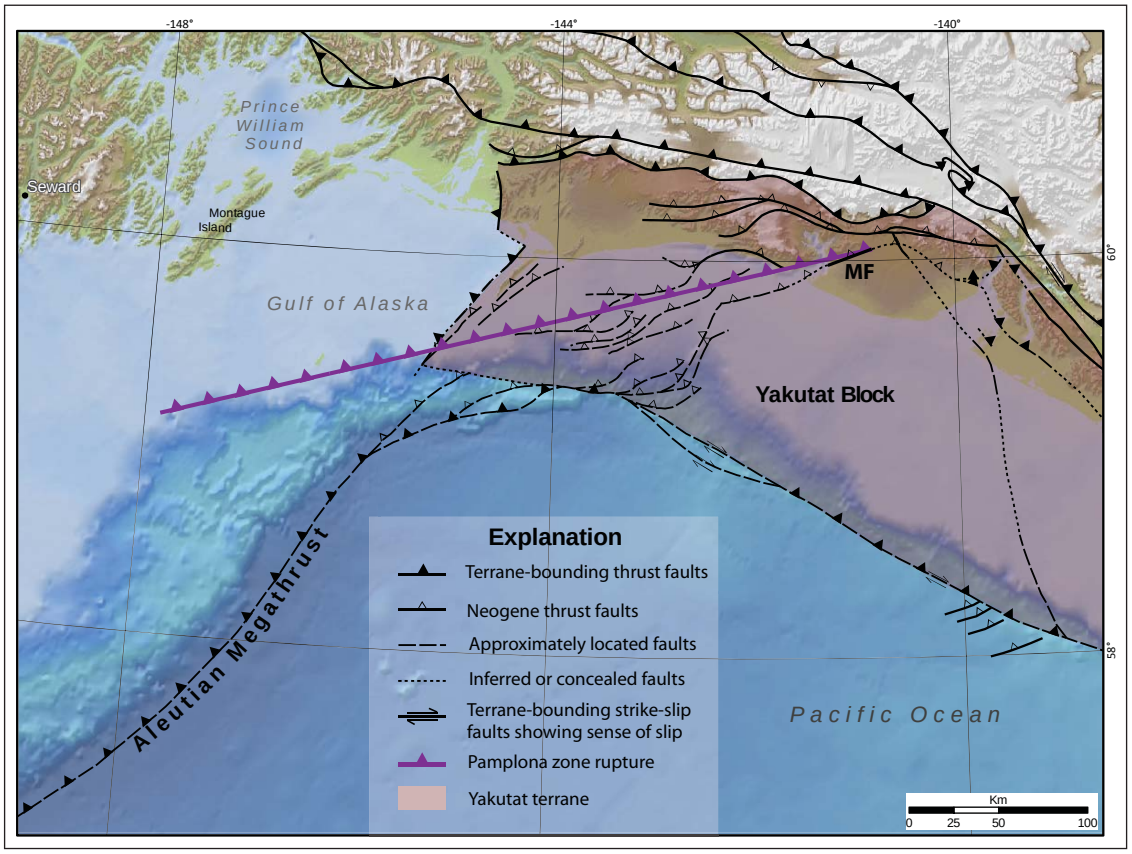

Figure 15. Geologic setting of the Yakutat block with major faults, from Plafker and Thatcher (2008). The hypothetical Pamplona zone rupture (Scenario 4) is shown by a purple line; Malaspina fault is indicated by "MF."

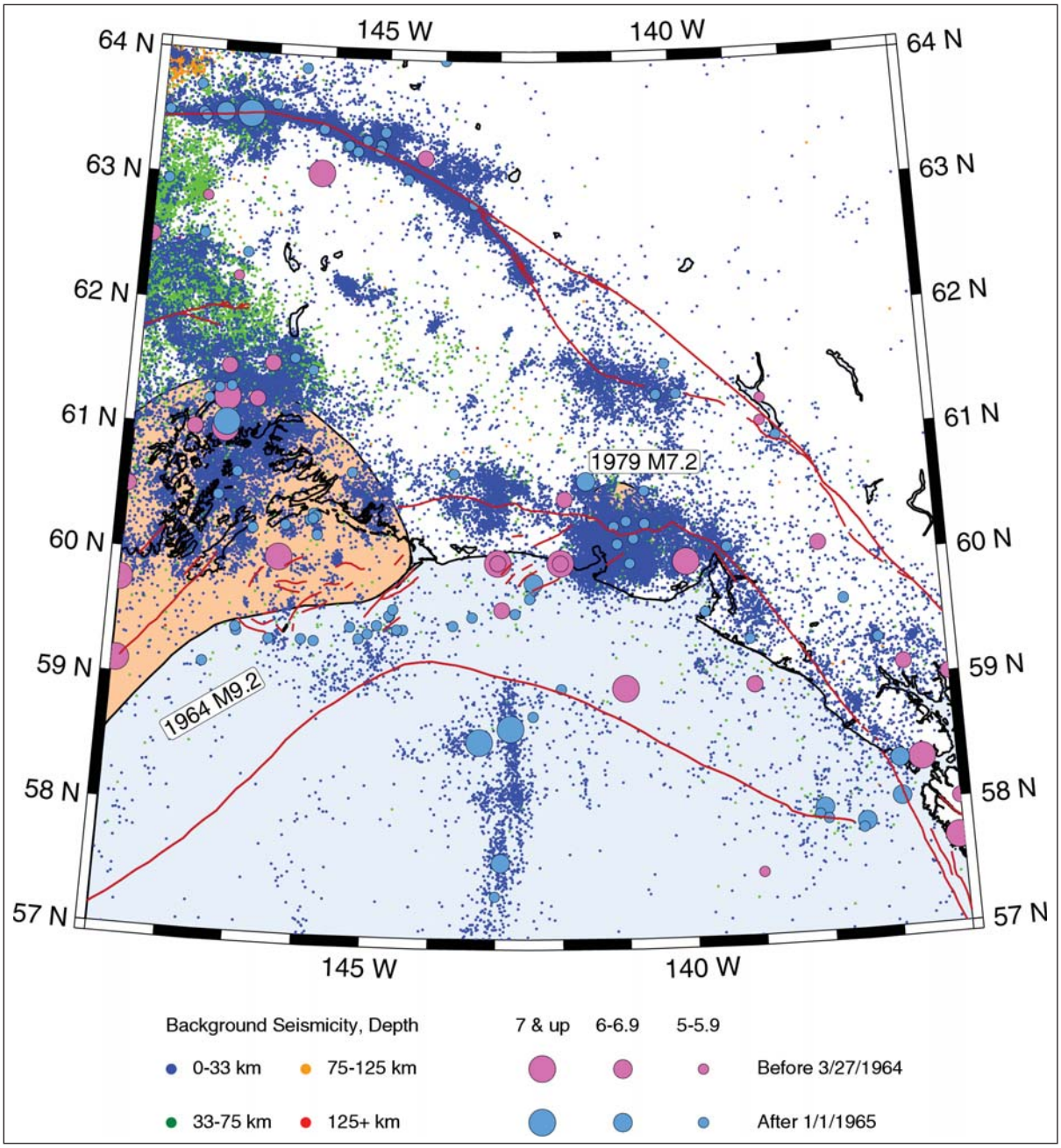

Figure 16. Earthquakes in the vicinity of the Yakutat block, from the Alaska Earthquake Information Center catalog. Major faults are shown by red lines; areas shaded in beige are rupture zones of the 1964 Great Alaska Earthquake and the 1979 earthquake. Small dots correspond to earthquakes with magnitude greater than 1 and less than 5. Large circles show significant earthquakes (magnitude 5 and greater) before (purple) and after (light blue) the great Alaska earthquake of March 27, 1964. The main shock and aftershocks of this event are not included in the plot.

Table 3. Fault parameters for scenario 4.

Lat [deg. N]	Lon [deg. W]	Depth [km]	Length [km]	Width [km]	Strike [deg.]	Dip [deg.]	Rake [deg.]	Slip [m]
60.05	140.83	5	410	175	255	12	90	10

LANDSLIDE TSUNAMI SOURCES

MULTIPLE SUBMARINE SLOPE FAILURES IN RESURRECTION BAY DURING THE 1964 EARTHQUAKE

Studies by Lee and others (2006) and Haeussler and others (2007) provided analysis of pre- and post-earthquake bathymetric data and high-resolution sub-bottom profiles of Resurrection Bay and showed convincing evidence of massive submarine landsliding during the 1964 earthquake. They utilized a 2001 NOAA high-resolution multibeam bathymetric survey of Resurrection Bay to study the morphology and depth changes of the fjord bottom. A shaded relief map derived from this bathymetric data shows a variety of seafloor features related to submarine slides. Lee and others (2006) identified remains of the Seward waterfront that failed in 1964 as a result of strong ground shaking. These remains are visible as blocky debris extending offshore from Seward for about 750 m (fig. 18). The authors also identified dispersed debris flows that correspond to failures of the Resurrection River delta, and they concluded that the 1964 earthquake could potentially have triggered different failure types simultaneously. Haeussler and others (2007) concluded that several failures initiated along the fjord walls at relatively shallow depths, and the mass flows produced by these failures transported most of the material as far as 6 to 13 km into the bathtub (see fig. 4), covering the entire basin with a flow deposit. The authors created a bathymetric difference grid that shows depth changes in the bay resulting from the 1964 slope failures. The estimated total volume of slide material is 211 million cubic meters. A map of the slide thickness, derived from the bathymetric difference grid, is shown in figure 19. The first numerical modeling study of local tsunamis in Resurrection Bay (Suleimani and others, 2009) utilized these findings and concluded

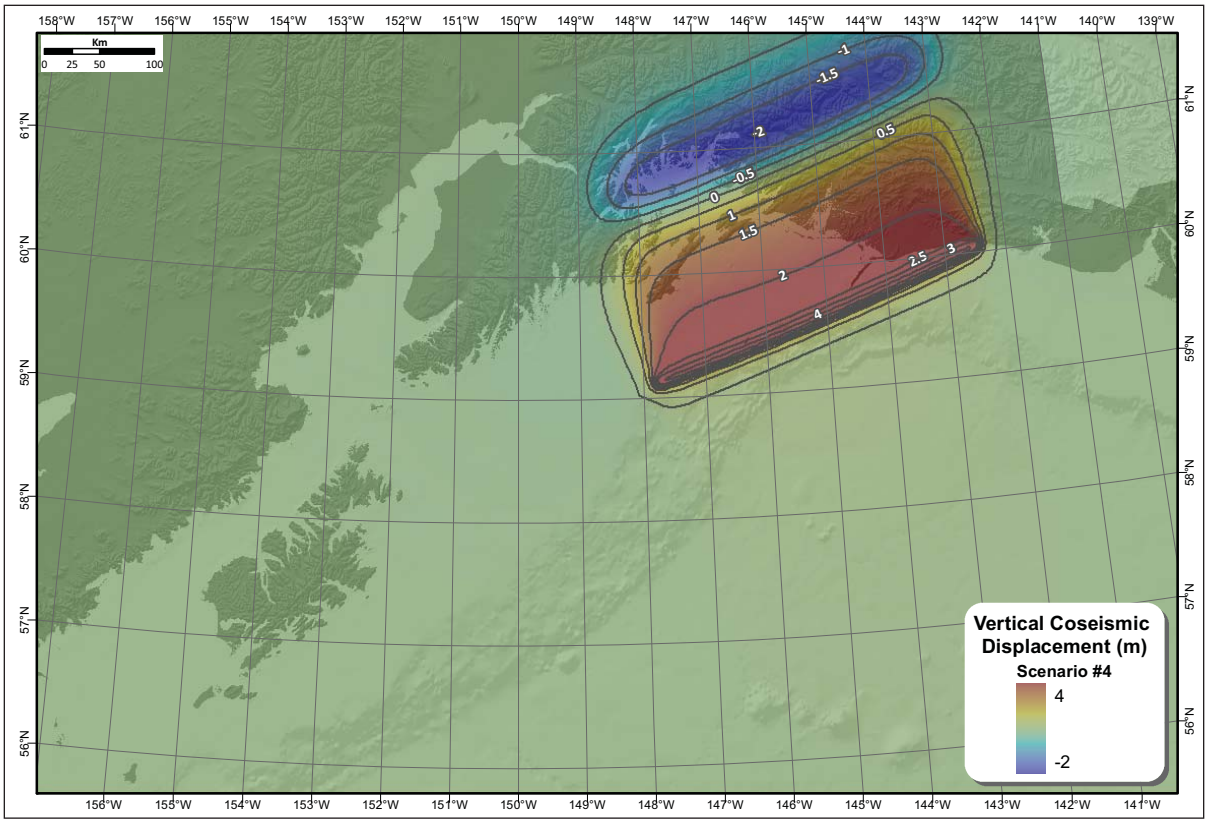

Figure 17. Scenario 4. Pamplona zone deformation model.

that the waves observed at the Seward waterfront and in several other locations in Resurrection Bay resulted from multiple submarine slope failures. Suleimani and others (2009) conducted a numerical experiment to investigate how individual underwater slides contributed to observed tsunami amplitudes in the bay. They showed that slides in the northern part of the bay were the major contributors to the tsunami amplitudes at Seward, and that the contribution from other slide complexes was negligible.

LANDSLIDE TSUNAMI SCENARIOS

Scenario 5. Waves generated by three major underwater slide complexes of the 1964 earthquake – Seward downtown slide, Lowell Point slide, and Fourth of July slide.

Figure 20 shows three slide complexes in the upper bay that were the major contributors to the locally generated waves that inundated Seward (Suleimani and others, 2009). The slide thicknesses were derived by Haeussler and others (2007) from the bathymetric difference grid. This distribution of the slide material serves as an initial condition for tsunami simulation. The total volume for these three slide complexes was approximately 80.6 million cubic meters.

Scenario 6. Hypothetical event: Simultaneous underwater slope failures at four locations where sediment accumulated since 1964.

The bathymetric difference grid derived by Haeussler and others (2007) shows four major areas in upper Resurrection Bay where sediment accumulated since 1964: (1) a new location of sediment deposition from the rerouted Lowell Creek; (2) and (3) accumulation areas at the fjord head delta; and (4) a new location of sediment deposition from the rerouted Fourth of July Creek (fig. 21). The total volume of sediments in all locations is approximated at 6.5 million cubic meters. We assume that the slope failures occur at the same time, and that the failure surfaces correspond to the post-earthquake bottom of Resurrection Bay. This means that the volume of the failed material will be equal to the volume of sediments accumulated after the 1964 earthquake.

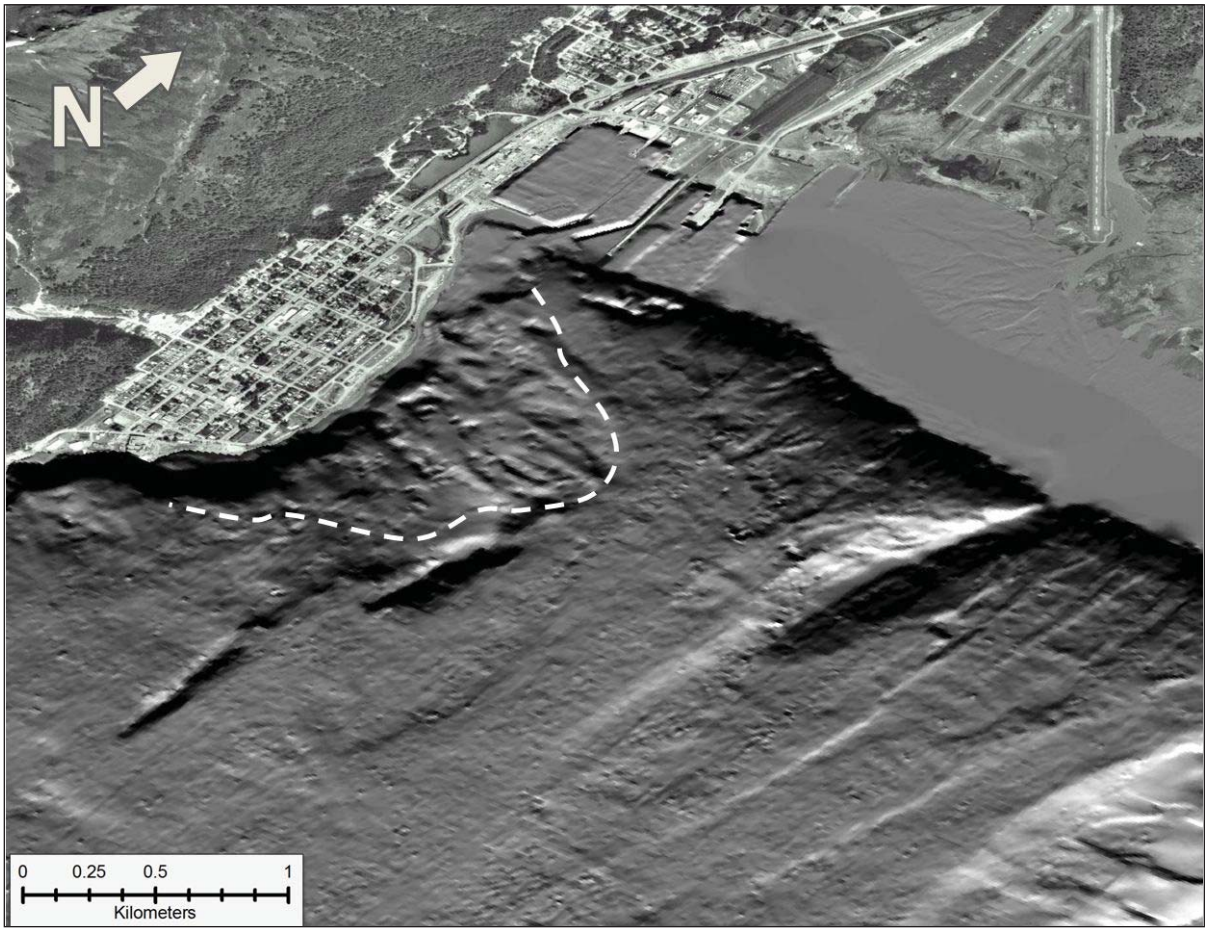

Figure 18. Oblique image of Seward downtown, with offshore shaded-relief bathymetry. Dashed white lines indicates the approximate margin of debris resulting from a submarine landslide that was triggered by the 1964 earthquake.

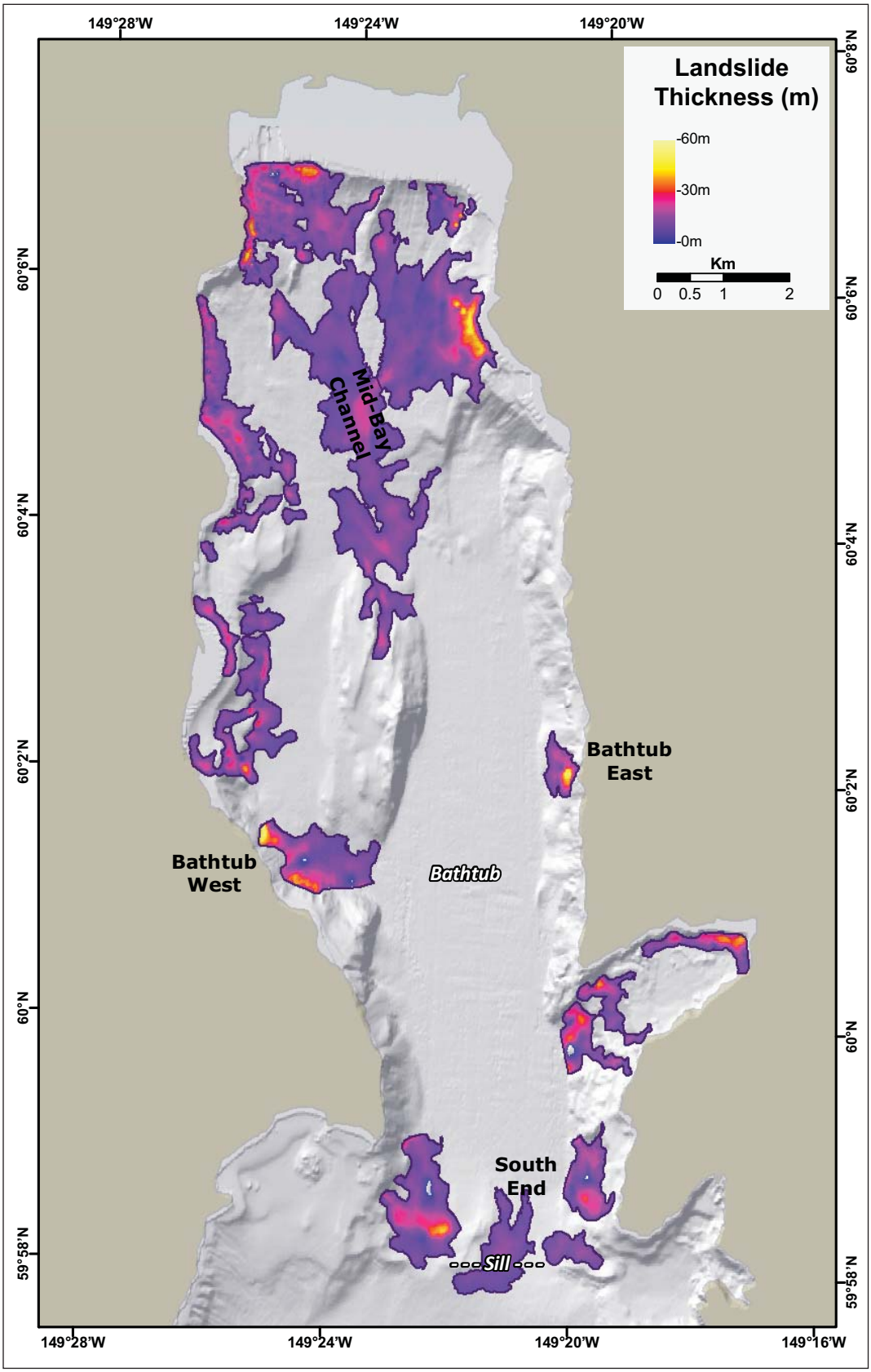

Figure 19. Distribution of initial thickness of the sliding mass.

Scenario 7. Hypothetical event: Simultaneous underwater slope failures at four locations where sediment accumulated since 1964, with added sediment volumes.

Recent coring surveys conducted in Resurrection Bay (Clark Alexander, oral commun.) provide information on morphology of slide deposits and on sediment accumulation rates in the fjord. One of the cores was taken offshore at the fjord head delta front (fig. 21), and its Pb-210 and Cs-137 isotope profiles suggest that this area did not fail during the 1964 earthquake. This core also shows the highest accumulation rate among other cores in Resurrection Bay, about 2 cm per year. We base this second hypothetical landslide scenario on the same areas of sediment accumulation shown in figure 21, with an addition of extra volume of sediments that will

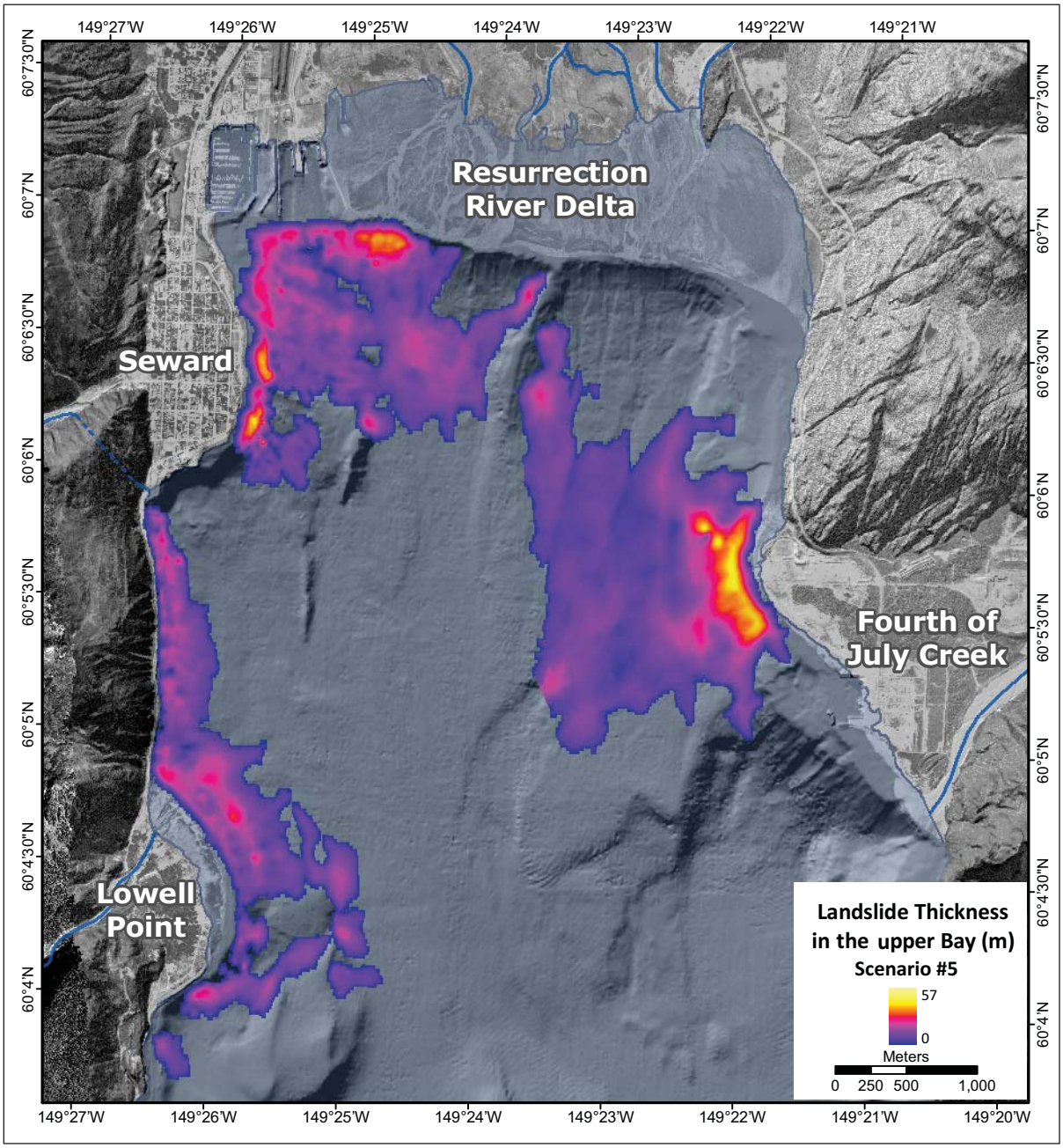

Figure 20. Scenario 5. The three major slides of the 1964 earthquake-triggered massive slope failures in Resurrection Bay, which produced the greatest contribution to tsunami amplitudes at Seward. Other submarine landslides triggered in Resurrection Bay in 1964 produced negligible effects.

be accumulated over decades. Also, future earthquakes can release lower layers of sediment that remained intact during the 1964 earthquake. Since it is not possible to predict potential failure surfaces without comprehensive slope stability analysis, we account for that additional failing mass by adding extra volume to the existing accumulated volume. This hypothetical scenario includes four slides, with the total volume approximately 100 million cubic meters.

MODELING RESULTS

NUMERICAL MODELING OF THE 1964 TSUNAMI IN RESURRECTION BAY: MODEL VERIFICATION

In this section, we compare results of inundation modeling of the 1964 tsunami in Resurrection Bay with observations collected shortly after the event. Because the source of local waves in Resurrection Bay ceased at the end of ground shaking (Wilson and Tørum, 1968),

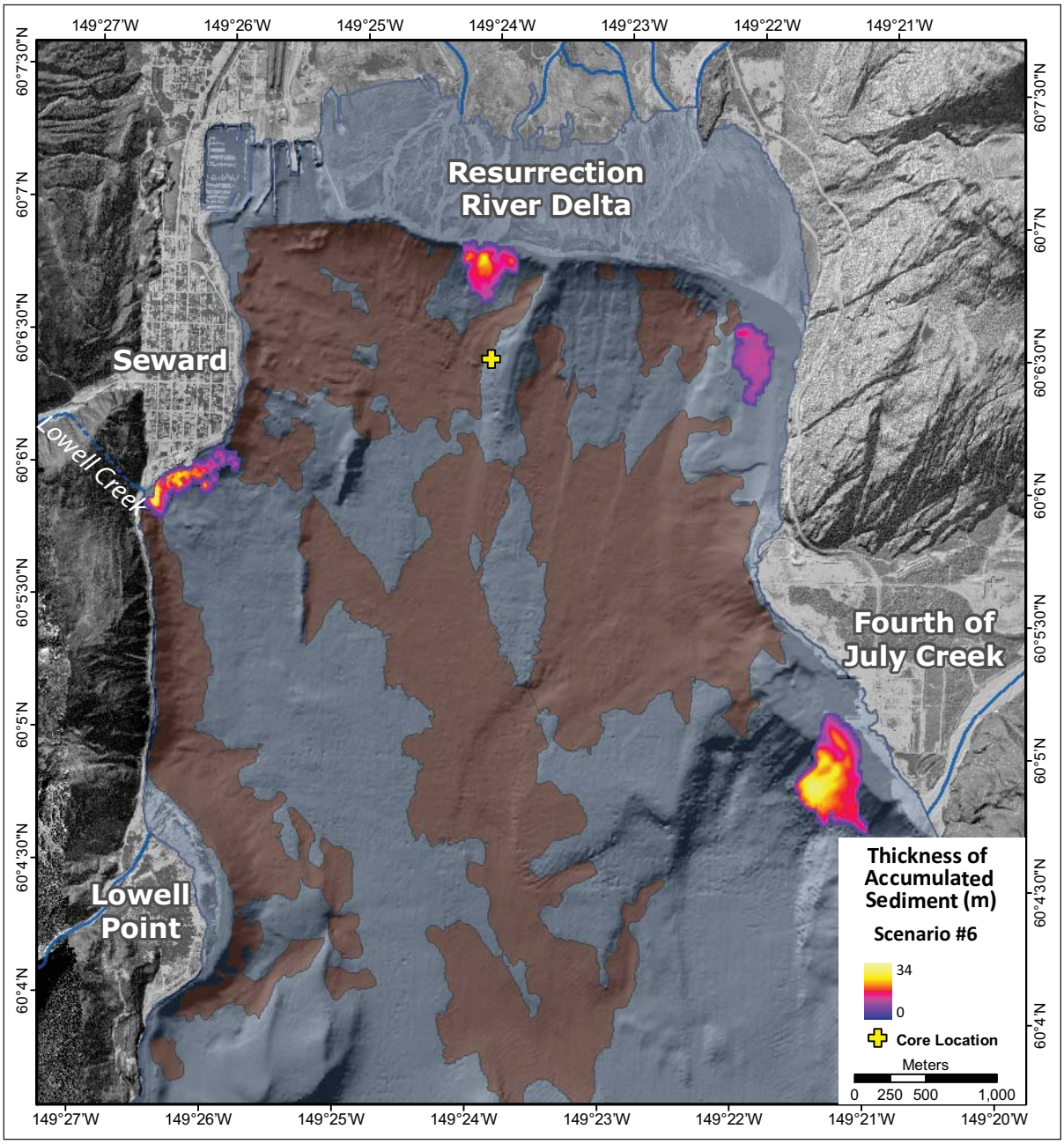

Figure 21. Scenario 6. Accumulation areas with thicknesses and location of the S2G1 core studied by Clark Alexander (oral commun.). Brown areas indicates the original positions of landslide masses released during the 1964 earthquake.

about 20 minutes before the arrival of the tectonic tsunami, we can assume that these events are independent and model them separately. The union of inundation areas computed independently for tectonic and landslide-generated waves will be compared to the observed composite inundation pattern.

The numerical grid used in inundation modeling covers the northern part of Resurrection Bay (fig. 20). We assume that the slides were initially at rest, then triggered by ground shaking at t = 0, and moved thereafter only under the force of gravity. At the southern open boundary of the grid, we specify the radiation boundary condition for the water waves. The boundary condition for the slide mass allows the slide to leave the computational domain without reflection. The moving boundary condition at the shoreline allows for wetting and drying of land. Shannon and Hilts (1973) conducted a subsurface geotechnical investigation of materials that failed in Resurrection Bay during the 1964 earthquake. They found that the density of the slide material ranged from 2.0g/cm^3 to 2.11g/cm^3. We do not have any measurements of the slide viscosity, but sensitivity studies by Rabinovich and others (2003) demonstrated that the influence of kinematic viscosity on tsunami wave heights is small. We assume slide density of $\rho = 2.0$g/cm^3 and slide viscosity of $\mu = 0.05$m^2/s. The upper and lower surfaces of the slide mass are defined by the initial slide thickness distribution (fig. 20). The slide thicknesses are added to the bathymetry values in order to define the pre-earthquake depths in Resurrection Bay. Although it is possible that individual slides were triggered at different times after the initial ground shaking, there is no independent evidence to support this hypothesis. Therefore we assume in the model that all slides start moving at the same time.

The recent numerical study by Suleimani and others (2009) confirms the observations that Seward was inundated by locally generated waves within 5 minutes of the main shock. We run numerical simulation of landslide tsunamis for 5 minutes of physical time with a time step $\Delta t = 0.01$ seconds. The yellow line in figure 22 delineates the observed inundation area at Seward downtown. The inundation line was digitized from the U.S. Army Corps of Engineers aerial photo of Seward that was taken one day after the earthquake (Lemke, 1967). The maximum observed extent of inundation at the head of the bay is shown by a yellow line in figure 23. This line, digitized from a geologic map (Plate 1, Lemke, 1967), documents the maximum runup from one or more waves, therefore representing the composite inundation pattern. Green lines in figures 22 and 23 show calculated extent of inundation from 1964 local landslide-generated tsunami waves at Seward and at the head of the bay, respectively. The results show little inundation in the delta area at the head of the bay, and significant inundation in downtown Seward. This can be explained by directionality of the waves that were induced by the slides (fig. 20), and by topographic changes that have occurred since 1964. Suleimani and others (2009) showed that the highest observed wave at the Seward waterfront was generated by the Fourth of July Creek slope failure. The same wave traveled as an edge wave at the head of the bay. Simulated locally generated waves did not cause much inundation in the harbor area, because the topographic data reflect the present conditions. There were significant changes to the harbor area since 1964, and the new topographic data set includes breakwaters that did not exist in 1964.

Figures 22 and 23 also show calculated extent of inundation from a tectonic tsunami. The blue line corresponds to the tectonic wave that was modeled using JDM, and the purple line corresponds to the wave modeled using SDM. The tectonic wave produced by JDM penetrates deeper inland and completely inundates the airport. These results vastly overestimate inundation of the airport area after the 1964 Great Alaska Earthquake (fig. 23). The wave associated with SDM produces an inundation zone that matches observations very well. In Seward downtown, the wave associated with JDM also penetrates deeper inland than the wave associated with SDM (fig. 22). The landslide-generated waves travel farther inland in the downtown area than the SDM-produced waves, but do not produce much inundation in the harbor area. This can be explained by the fact that the harbor area has substantially changed since 1964, and this primarily affected the modeling results for shorter wave lengths, that is, for landslide-generated waves. The union of inundation areas computed independently for tectonic and landslide-generated waves is in good agreement with observations.

RESULTS OF HYPOTHETICAL TSUNAMI SCENARIOS

We performed numerical calculations for all scenarios described above. In every case, the initial water disturbance propagated through the set of embedded grids of increasing resolution. In a final grid of 15m resolution, where bathymetric and topographic data are combined in a continuous data set, we computed the extent of inundation using a moving boundary condition.

Sheet 1 shows inundation limits for all tectonic scenarios. Scenarios 1 and 2 (SDM and the Prince William Sound asperity of SDM) represent a source model of the 1964 earthquake and both predict high inundation. The inundation area that corresponds to the entire 1964 rupture zone coincides almost entirely with the inundation zone that corresponds to the Prince William Sound asperity alone. That allows us to conclude that the largest tectonic waves of the 1964 Alaska tsunami observed at

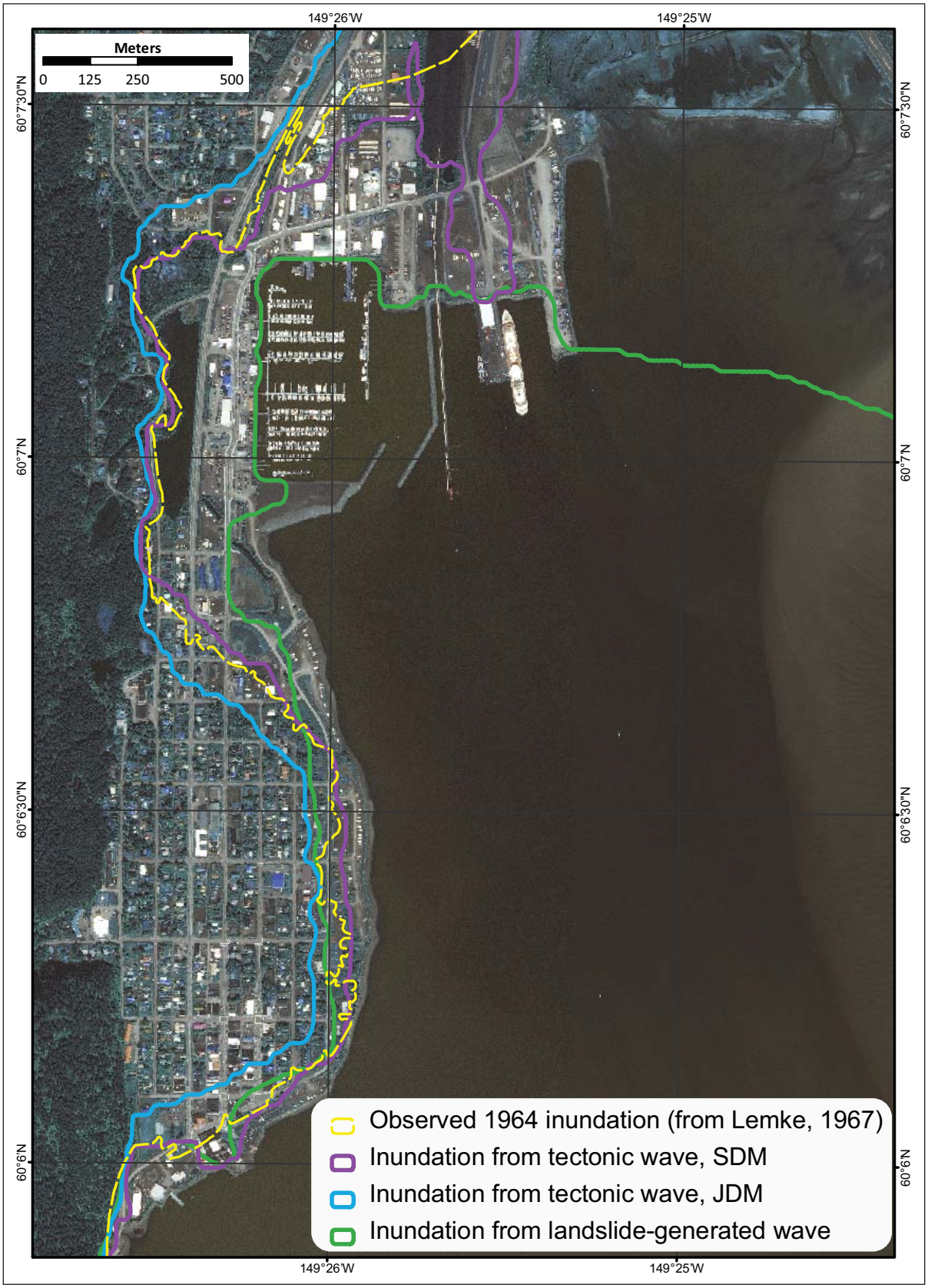

Figure 22. Observed 1964 inundation line (from Lemke, 1967) and calculated inundation lines from tectonic and landslide sources at Seward.

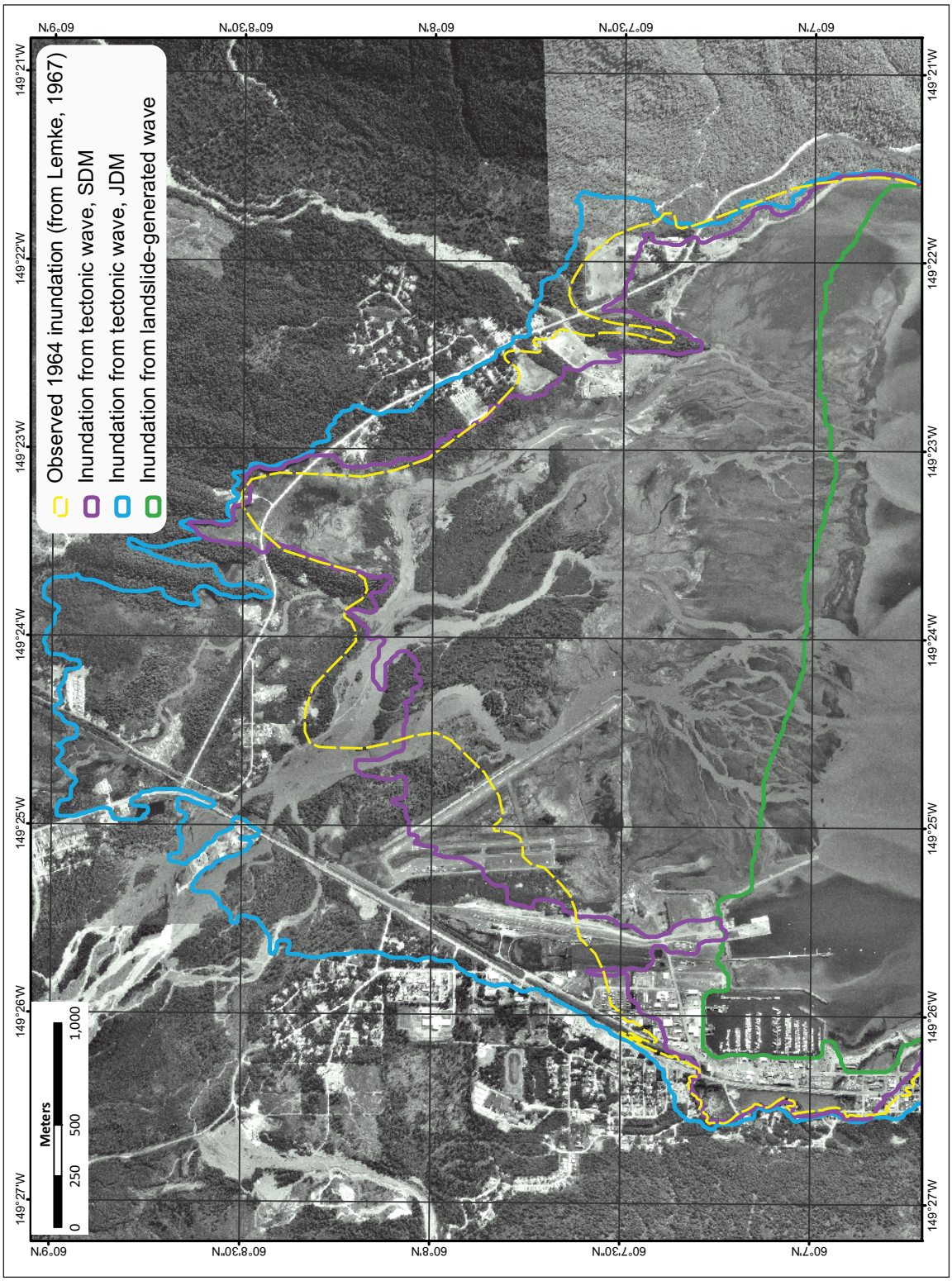

Figure 23. Observed 1964 inundation line (from Lemke, 1967) and calculated inundation lines from tectonic and landslide sources at the head of Resurrection Bay.

Seward were generated by sea floor displacements above the Prince William Sound asperity of the 1964 rupture. The numerical results for Scenarios 3 and 4 (the Kodiak asperity of SDM and the Pamplona zone rupture) predict only moderate inundation, with the Pamplona inundation zone being larger than the Kodiak zone.

Sheet 2 displays inundation lines calculated for the hypothetical landslide scenarios 5–7. The largest inundation area corresponds to a scenario that involves three major slide complexes of the 1964 slope failure. This scenario was calculated using MHW datum.

Sheet 3 shows the maximum composite calculated extent of inundation for all scenarios, and the maximum composite flow depths over dry land. For easier visual reference, on the scale for flow depths we indicated the values of 0.5 m, which approximately corresponds to knee height, and 2 m, which is just above the average person's body height. In several areas in the northeastern section of the tidal flats, the mapped 1964 inundation limit (Lemke, 1967) extends beyond the maximum estimated inundation. We did not adjust the maximum calculated inundation extent in these areas to match the 1964 limit, because the observed inundation line there obviously was not georeferenced well, crossing areas of very high elevations.

TIME SERIES AND OTHER NUMERICAL RESULTS

To provide more accurate assessment of tsunami hazard for any particular community, we have supplemented the inundation maps with information about the calculated time history of the tsunami wave action in the region. The time of arrival of the first wave, the maximum wave amplitude, and duration of the wave action are important factors that should be considered by emergency managers during evacuation planning.

Appendix 1 contains plots of sea level and velocity time series for all scenarios at a number of locations in Resurrection Bay, shown in figure A1-1. The zero time corresponds to the epicenter origin time, and zero water level corresponds to the post-earthquake MHW level. Since velocity magnitude is calculated as water flux divided by water depth, the velocity value becomes physically meaningless when water depth is less than 10 cm. Therefore, we plot velocity values only for water depths greater than 10 cm. Also, for each scenario we provide plots of maximum flow depths in inundation areas and plots of maximum drag force. At each grid point that corresponds to initially dry land, the flow depth is computed at every time step during the tsunami propagation time interval (8 hours), and the maximum value is kept.

Tsunami flow depth is one of the important indicators of potential damage, and must be differentiated from runup height (Synolakis and Bernard, 2006). For use in engineering applications, the flow depths must be supplemented with the momentum flux, which is proportional to the drag force (Yeh, 2006). We calculate drag force as a product of water depth and velocity squared. The plot of maximum drag force for Scenario 1 (repeat of 1964 tectonic waves, SDM) is shown in figure 24. The maximum values occur during the drawdown of the long tectonic wave, mostly affecting the boat harbor area between the jetties, and the shallow intertidal zone. Figure 25 shows drag force for Scenario 5 (repeat of 1964 landslide-generated waves). Because landslide-generated waves are shorter than tectonic waves, the maximum values occur in the generation area, where the slide starts moving down the slope.

SOURCES OF ERRORS AND UNCERTAINTIES

The hydrodynamic model that was used to calculate tsunami propagation and runup is a nonlinear flux-formulated shallow water model (Nicolsky and others, in press). It passed the major analytical, laboratory and field benchmarks that are required for models used in production of tsunami inundation maps (Synolakis and others, 2007).

The source mechanism remains the biggest unknown in the problem of tsunami modeling. Since the initial condition for the modeling is determined by the displacement of the ocean bottom, the largest source of errors is the earthquake model. When the tsunami is generated in the vicinity of the coast, the direction of the incoming waves, their amplitudes, and times of arrival are determined by the initial displacements of the ocean surface in the source area, because the distance to the shore is too small for the waves to disperse. Therefore, the near-field inundation modeling results are especially sensitive to the fine structure of the tsunami source. The modeling process is subject to many more errors when the complexity of the source function is combined with the proximity of the coastal zone.

The 15-m resolution of the inundation modeling is limited by the resolution of the topographic and bathymetric data used for the grid construction. This resolution is high enough to describe major relief features, seawalls, jetties, and other marine structures, although very small topographic features, buildings, and other facilities cannot be accurately resolved by the existing model.

SUMMARY

We present the results of numerical modeling of earthquake-generated tsunami waves for the Seward area and northern Resurrection Bay, Alaska. We considered several tectonic and landslide scenarios and provided an estimate of maximum credible tsunami inundation. These results are useful for state and local emergency managers to identify areas that should be evacuated in

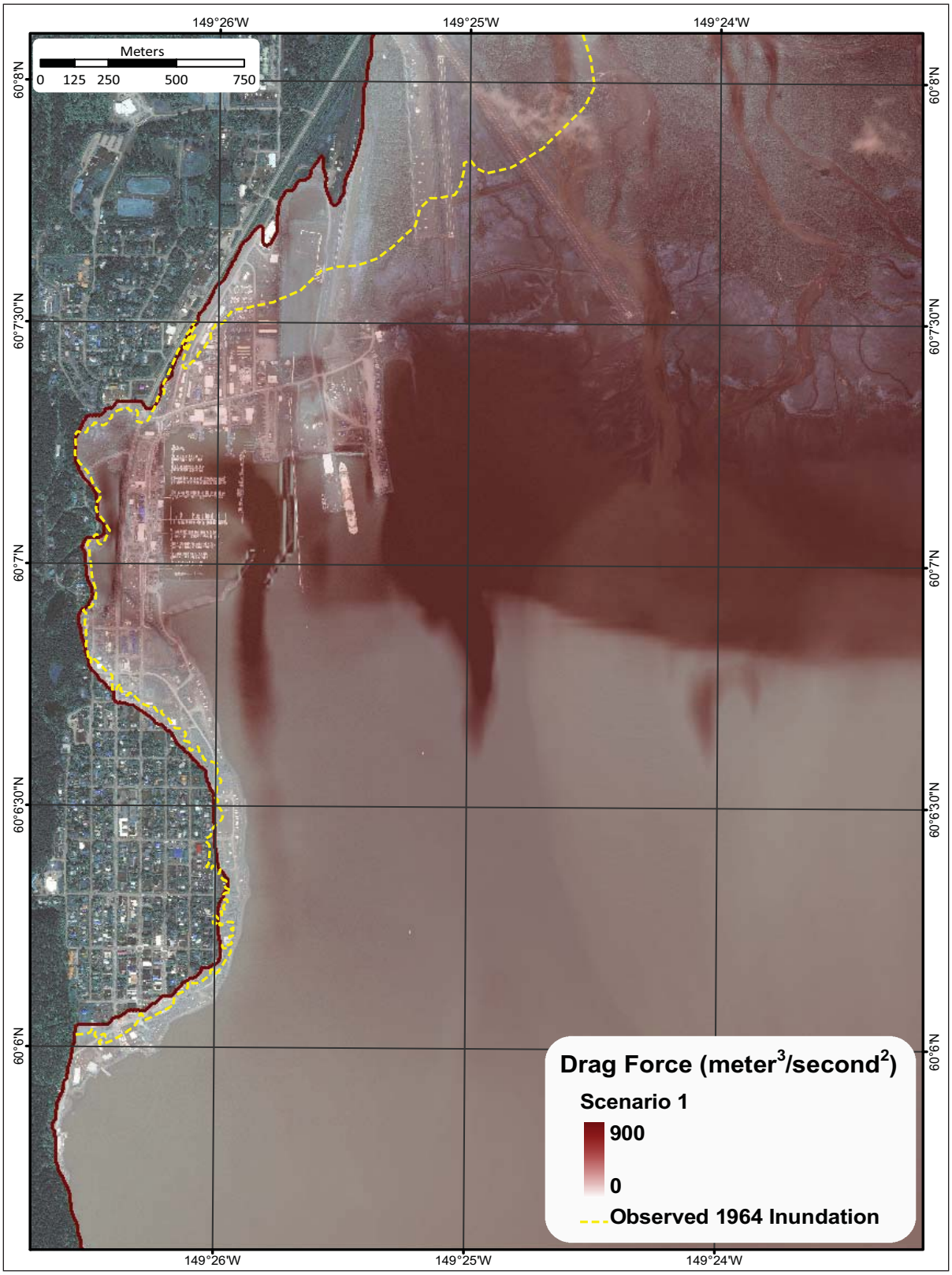

Figure 24. Maximum calculated drag force in the areas of Seward downtown, harbor, and airport for Scenario 1.

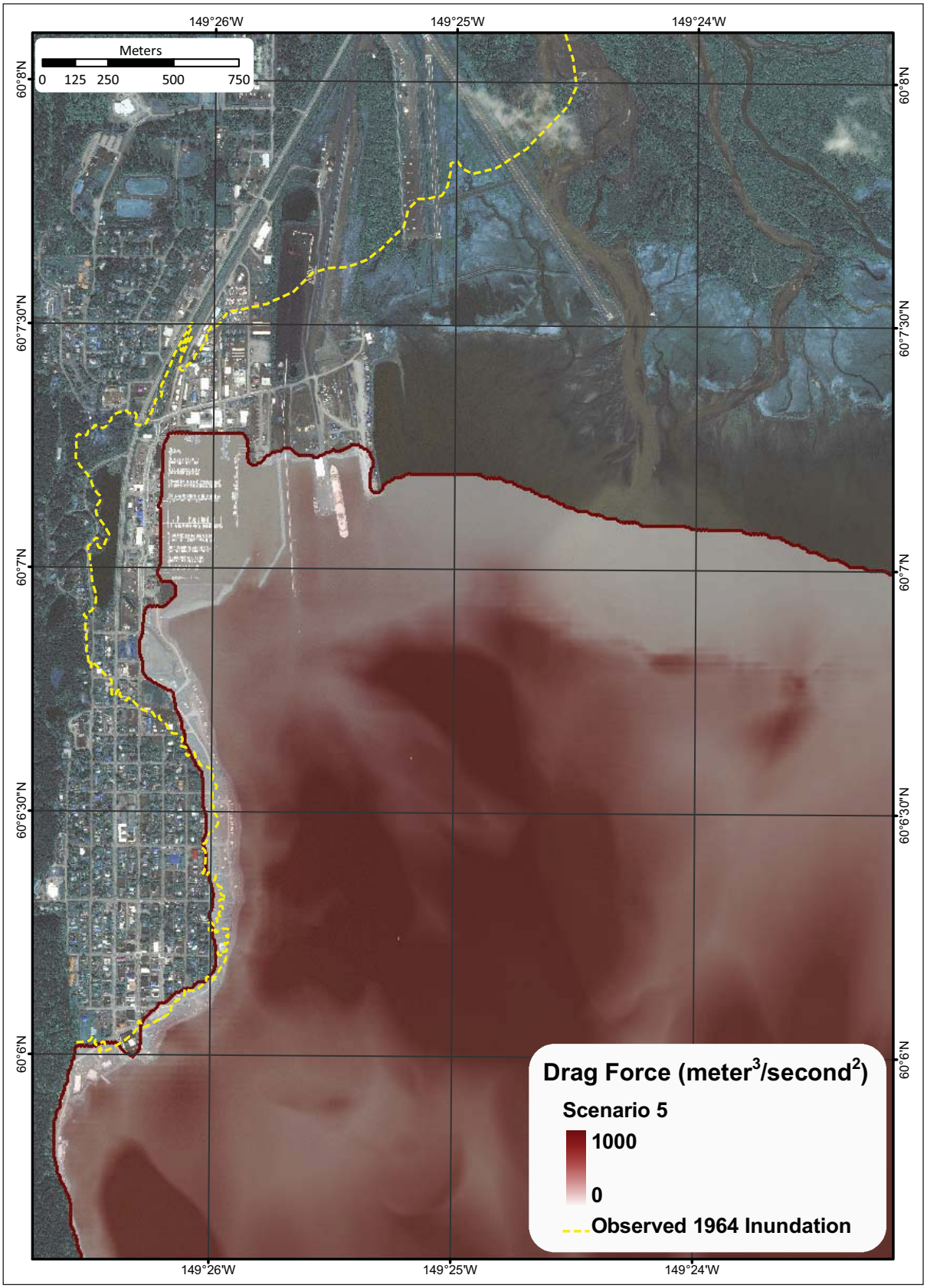

Figure 25. Maximum calculated drag force in the areas of Seward downtown, harbor, and airport for Scenario 5.

the event of a major tsunamigenic earthquake. Because of the uncertainties inherent in this type of modeling, these results are not intended for land-use regulation.

ACKNOWLEDGMENTS

This project was supported by National Oceanic and Atmospheric Administration grants 27-014d and 06-028a through Cooperative Institute for Arctic Research. Numerical calculations for this work were supported by a grant of High Performance Computing (HPC) resources from the Arctic Region Supercomputing Center (ARSC) at the University of Alaska Fairbanks as part of the U.S. Department of Defense HPC Modernization Program. We thank Dr. Robert C. Witter and Dr. Aggeliki Barberopoulou for their thoughtful reviews of the draft manuscript and maps.

REFERENCES

Alaska, State of, Department of Commerce, Community & Regional Affairs, Division of Community Advocacy, 2005, Community Database Online; Seward Community Overview: http://www.commerce.state.ak.us/dca/commdb/CF_BLOCK.cfm, accessed 3/2/2010.

Assier-Rzadkiewicz, S., Mariotti, C., and Heinrich, Philippe, 1997, Numerical simulation of submarine landslides and their hydraulic effects: Journal of Waterway, Port, Coastal and Ocean Engineering, v. 123, no. 4, p. 149–157.

Bornhold, B.D., Thomson, R.E., Rabinovich, A.B., Kulikov, E.A., and Fine, I.V., 2001, Risk of landslide-generated tsunamis for the coast of British Columbia and Alaska, in 2001, An Earth Odyssey; Proceedings of the 54th Canadian Geotechnical Conference, Calgary, Alberta: Alliston, Ontario, Canada, Canadian Geotechnical Society, p. 1,450–1,454.

Carver, Gary, and Plafker, George, 2008, Paleoseismicity and neotectonics of the Aleutian subduction zone—An overview, *in* Freymueller, J.T., Haeussler, P.J., Wesson, R.L, and Ekström, Goran, eds., Active tectonics and seismic potential of Alaska: American Geophysical Union Geophysical Monograph 179, p. 43–63.

Christensen, D.H., and Beck, S.L., 1994, The rupture process and tectonic implications of the Great 1964 Prince William Sound Earthquake: Pure and Applied Geophysics, v. 142, no. 1, p. 29–53.

Coulter, H.W., and Migliaccio, R.R., 1966, Effects of the earthquake of March 27, 1964, at Valdez, Alaska: U.S. Geological Survey Professional Paper 542-C, 36 p.

DeMets, Charles, Gordon, R.G., Argus, D.F., and Stein, Seth, 1990, Current plate motions: Geophysical Journal International, v. 101, no. 2. p. 425–478.

Doser, D.I., and Brown, W.A., 2001, A study of historic earthquakes of the Prince William Sound, Alaska, region: Bulletin of the Seismological Society of America, v. 91, p. 842–857.

Fine, I.V., Rabinovich, A.B., Kulikov, E.A., Thomson, R.E., and Bornhold, B.D., 1998, Numerical modeling of landslide-generated tsunamis with application to the Skagway Harbor tsunami of November 3, 1994, in Proceedings, International Conference on Tsunamis, Paris, p. 211–223.

Freymueller, J.T., Cohen, S.C., and Fletcher, H.J., 2000, Spatial variations in present-day deformation, Kenai Peninsula, Alaska, and their implications: Journal of Geophysical Research, v. 105, no. B4, p. 8,079–8,101.

Haeussler, P.J., Lee, H.J., Ryan, H.F., Labay, K.A., Kayen, R.E., Hampton, M.A., and Suleimani, E.N., 2007, Submarine slope failures near Seward, Alaska, during the M9.2 1964 earthquake, *in* Lykousis, Vasilios, Sakellariou, Dimitris, and Locat, Jacques, eds., Submarine mass movements and their consequences: Springer, p. 269–278.

Hamilton, Sarah, and Shennan, Ian, 2005, Late Holocene great earthquakes and relative sea-level change at Kenai, southern Alaska: Journal of Quaternary Science, v. 20, no. 2, p. 95–111.

Hampton, M.A., Lee, H.J., and Locat, Jacques, 1996, Submarine landslides: Reviews of Geophysics, v. 34, no. 1, p. 33–59.

Hampton, M.A., Lemke, R.W., and Coulter, H.W., 2002, Submarine landslides that had a significant impact on man and his activities—Seward and Valdez, Alaska, *in* Schwab, W.C., Lee, H.J., and Twichell, D.C., eds., Submarine landslides; Selected studies in the U.S. Exclusive Economic Zone: U.S. Geological Survey Bulletin 2002, p. 123–134.

Holdahl, S.R., and Sauber, Jeanne, 1994, Coseismic slip in the 1964 Prince William Sound earthquake—A new geodetic inversion: Pure and Applied Geophysics, v. 142, no. 1, p. 55–82.

Ichinose, Gene, Somerville, Paul, Thio, H.K., Graves, Robert, and O'Connell, Dan, 2007, Rupture process of the 1964 Prince William Sound, Alaska, earthquake from the combined inversion of seismic, tsunami, and geodetic data: Journal of Geophysical Research, v. 112, no. B07, p. 306.

Jiang, Lin, and LeBlond, P.H., 1992, The coupling of a submarine slide and the surface waves which it generates: Journal of Geophysical Research, v. 97, no. C8, p. 12,731–12,744.

———Three-dimensional modeling of tsunami generation due to a submarine mudslide: Journal of Physical Oceanography, v. 24, no. 3, p. 559–572.

Johnson, J.M., Satake, Kenji, Holdahl, S.R., and Sauber, Jeanne, 1996, The 1964 Prince William Sound

earthquake—Joint inversion of tsunami waveforms and geodetic data: Journal of Geophysical Research, v. 101, no. B1, p. 523–532.

Kulikov, E.A., Rabinovich, A.B., Fine, I.V., Bornhold, B.D., Thomson, R.E., 1998, Tsunami generation by landslides at the Pacific coast of North America and the role of tides: Oceanology, v. 38, no. 3, p. 323–328.

Labay, K.A., and Haeussler, P.J., 2008, Combined high-resolution LIDAR topography and multibeam bathymetry for northern Resurrection Bay, Seward, Alaska: U.S. Geological Survey Digital Data Series 374, 7 p., data sets, http://pubs.er.usgs.gov/usgspubs/ds/ds374.

Lander, J.F., 1996, Tsunamis affecting Alaska 1737–1996: National Geophysical Data Center (NGDC) Key to Geophysical Research Documentation no. 31, 195 p.

Larsen, C.F., Echelmeyer, K.A., Freymueller, J.T., and Motyka, R.J., 2003, Tide gauge records of uplift along the northern Pacific–North American plate boundary, 1937 to 2001: Journal of Geophysical Research, v. 108, no. B4, p. 2216, doi:10.1029/2001JB001685.

Lee, Homa, Ryan, Holly, Kayen, R.E., Haeussler, P.J., Dartnell, Peter, and Hampton, M.A., 2006, Varieties of submarine failure morphologies of seismically-induced landslides in Alaska fjords: Norwegian Journal of Geology, v. 86, p. 221–230.

Lemke, R.W., 1967, Effects of the earthquake of March 27, 1964, at Seward, Alaska: U.S. Geological Survey Professional Paper 542-E, 48 p.

Nicolsky, D.J., Suleimani, E.N., and Hansen, R.A., in press, Validation and verification of a numerical model for tsunami propagation and runup: Pure and Applied Geophysics.

Nishenko, S.P., and Jacob, K.H., 1990, Seismic potential of the Queen Charlotte–Alaska–Aleutian seismic zone: Journal of Geophysical Research, v. 95, no. B3, p. 2,511–2,532.

Okada, Yoshimitsu, 1985, Surface deformation due to shear and tensile faults in a half-space: Bulletin of the Seismological Society of America, v. 75, p. 1,135–1,154.

Page, R.A., Biswas, N.N., Lahr, J.C., and Pulpan, Hans, 1991, Seismicity of continental Alaska, in Slemmons, D.B., Engdahl, E.R., Zoback, M.D., and Blackwell, D.D., eds., Neotectonics of North America: Boulder, Colorado, Geological Society of America, Decade Map Volume 1.

Plafker, George, 1967, Surface faults on Montague Island associated with the 1964 Alaska Earthquake: U.S. Geological Survey Professional Paper 543-G, 42 p.

Plafker, George, 1969, Tectonics: U.S. Geological Survey Professional Paper 543-I, 74 p.

Plafker, George, and Thatcher, Wayne, 2008, Geological and geophysical evaluation of the mechanisms of the great 1899 Yakutat Bay earthquakes, *in* Freymueller, J.T., Haeussler, P.J., Wesson, R.L., and Ekström, Goran, eds., Active tectonics and seismic potential of Alaska: Geophysical Monograph Series, v. 179, 431 p., ISBN 978-0-87590-444-3, AGU Code GM1794443.

Plafker, George, Carver, G.A., and Clarke, S.H., Jr., 2000, Seismotectonics of the 1964 Alaska earthquake as an analog for future tsunamigenic southern Cascadia subduction earthquakes, *in* Clague, J.J., Atwater, B.F., Wang, Kelin, Wang, Yumei, and Wong, I.G., eds., Proceedings of the Geological Society of America Penrose Conference, Great Cascadia Earthquake Tricentennial: Oregon Department of Geology and Mineral Industries Special Paper 33, p. 96–97.

Plafker, George, Kachadoorian, Reuben, Eckel, E.B., and Mayo, L.R., 1969, Effects of the earthquake of March 27, 1964, on various communities: U.S. Geological Survey Professional Paper 542-G, 50 p., 2 sheets, scale 1:250,000.

Rabinovich, A.B., Thomson, R.E., Bornhold, B.D., Fine, I.V., and Kulikov, E.A., 2003, Numerical modeling of tsunamis generated by hypothetical landslides in the Strait of Georgia, British Columbia: Pure and Applied Geophysics, v. 160, no. 7, p. 1,273–1,313.

Santini, Stefano, Dragoni, Michele, and Spada, Giorgio, 2003, Asperity distribution of the 1964 great Alaska earthquake and its relation to subsequent seismicity in the region: Tectonophysics, v. 367, no. 3–4, p. 219–233.

Sauber, J.M., and Molnia, B.F., 2004, Glacier ice mass fluctuations and fault instability in tectonically active southern Alaska, *in* James, T.S., Jacka, T.H., Morelli, A., and Dietrich, R, eds., Ice sheets and neotectonics: Global and Planetary Change, v. 42, no. 1–4, p. 279–293.

Sauber, J.M., McClusky, Simon, and King, Robert, 1997, Relation of ongoing deformation rates to the subduction zone process in southern Alaska: Geophysical Research Letters, v. 24, no. 22, p. 2,853–2,856.

Savoie, M.A., Savoie, J.M., Trefry, J.H., Semmler, C.M., Woodall, D.W., Trocine, R.P., Brooks, J.M., and McDonald, Tom, 2006, Port Valdez sediment coring program—Final 2004 monitoring report: Kinnetic Laboratories, Inc., Contract No. 961.04.1 for Prince William Sound Regional Citizens' Advisory Council, 76 p., http://www.pwsrcac.org/docs/d0024500.pdf.

Shannon, W.L., and Hilts, D.E., 1973, Submarine landslide at Seward, in The Great Alaska Earthquake

of 1964: Washington, D.C., Engineering, National Academy of Sciences, p. 144–156.

Shennan, Ian, Barlow, Natasha, and Combellick, R.A., 2008, Paleoseismological records of multiple great earthquakes in southcentral Alaska—A 4,000-year record at Girdwood, *in* Freymueller, J.T., Haeussler, P.J., Wesson, R.L, and Ekström, Goran, eds., Active Tectonics and Seismic Potential of Alaska: American Geophysical Union Geophysical Monograph 179, p. 185–199.

Suito, Hisashi, and Freymueller, J.T., 2009, A viscoelastic and afterslip postseismic deformation model for the 1964 Alaska earthquake: Journal of Geophysical Research, v. 114, B11404, doi:10.1029/2008JB005954.

Suleimani, E.N., Hansen, R.A., Combellick, R.A., Carver, G.A., Kamphaus, R.A., Newman, J.C., and Venturato, A.J., 2002, Tsunami hazard maps of the Kodiak area, Alaska: Alaska Division of Geological & Geophysical Surveys Report of Investigations 2002-1, 16 p., 4 sheets, scale 1:12,500.

Suleimani, E.N., Combellick, R.A., Marriott, D.A., Hansen, R.A., Venturato, A.J., and Newman, J.C., 2005, Tsunami hazard maps of the Homer and Seldovia areas, Alaska: Alaska Division of Geological & Geophysical Surveys Report of Investigations 2005-2, 28 p., 2 sheets, scale 1:12,500.

Suleimani, E.N., Haeussler, P.J., and Hansen, R.A., 2009, Numerical study of tsunami generated by multiple submarine slope failures in Resurrection Bay, Alaska, during the M9.2 1964 earthquake: Pure and Applied Geophysics, v. 166, p. 131–152.

Synolakis, C.E., and Bernard, E.N., 2006, Tsunami science before and beyond Boxing Day 2004: Philosophical Transactions of the Royal Society A, v. 364, no. 1845, p. 2,231–2,265.

Synolakis, C.E., Bernard, E.N., Titov, V.V., Kânoğlu, Utku, and González, F.I., 2007, Standards, criteria, and procedures for NOAA evaluation of tsunami numerical models: Seattle, WA, NOAA Technical Memo OAR PMEL-135, NOAA/Pacific Marine Environmental Laboratory, 55 p.

Thomson, R.E., Rabinovich, A.B., Kulikov, E.A., Fine, I.V., and Bornhold, B.D., 2001, On numerical simulation of the landslide-generated tsunami of November 3, 1994, in Skagway Harbor, Alaska, *in* Hebenstreit, G.T., ed., Tsunami research at the end of a critical decade: Kluwer, p. 243–282.

Wilson, B.W., and Tørum, Alf, 1968, The tsunami of the Alaskan Earthquake, 1964—Engineering evaluation: U.S. Army Corps of Engineers, Technical memorandum no. 25, 401 p.

Yeh, Harry, 2006, Maximum fluid forces in the tsunami runup zone: Journal of Waterway, Port, Coastal and Ocean Engineering, v. 132, no. 6, p. 496–500.

Appendix A

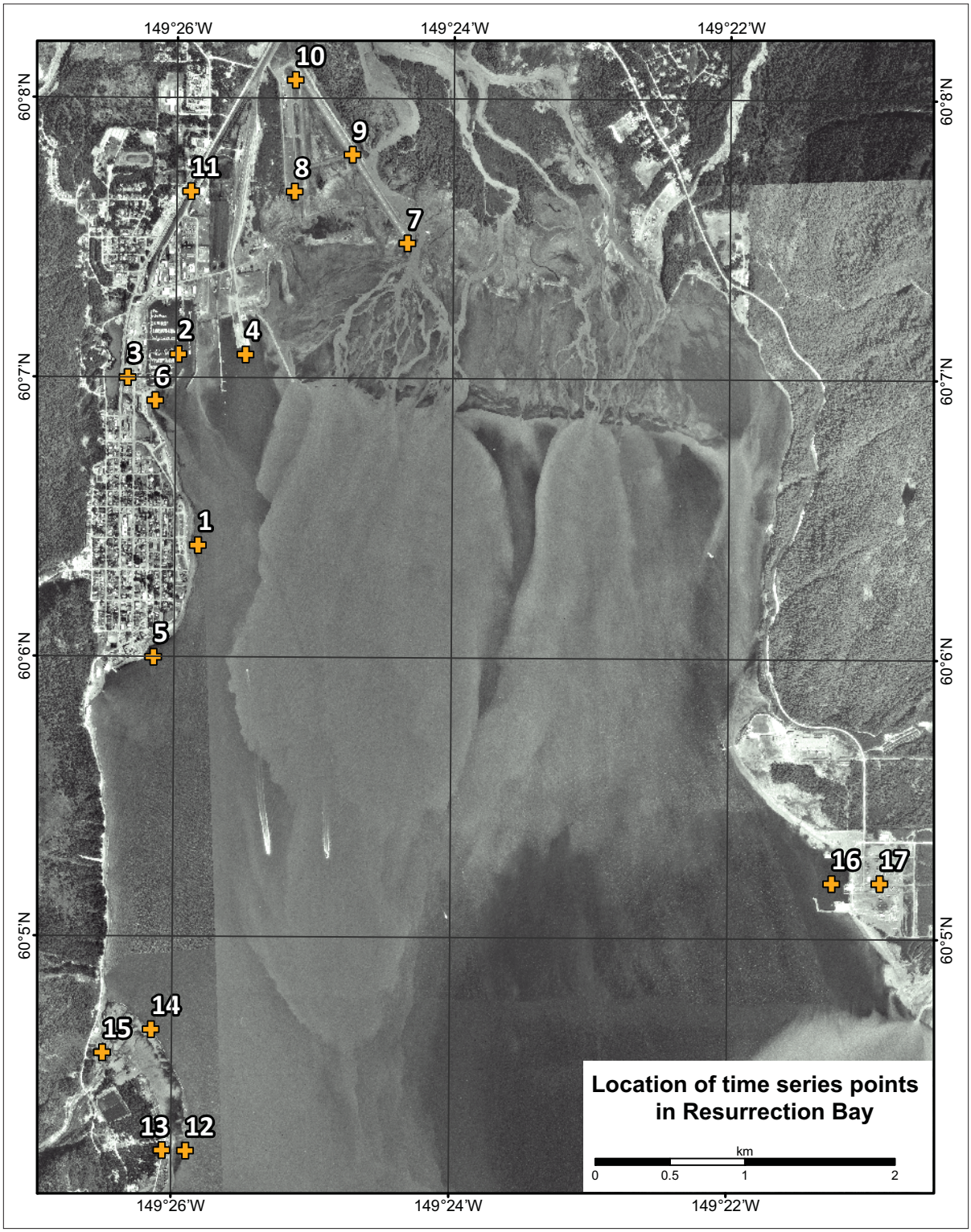

Figure A1-1. Locations of time series points.

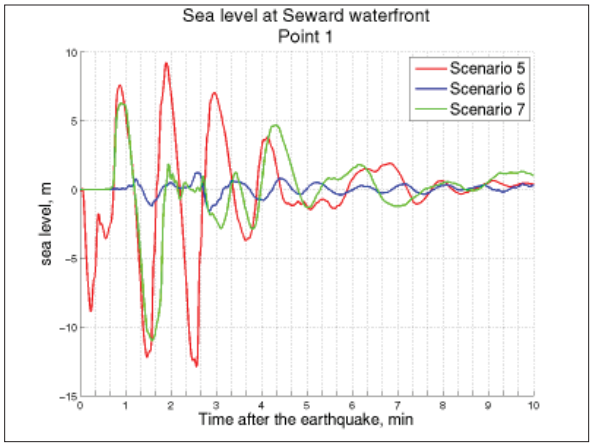
Sea level at Seward waterfront
Point 1
Scenario 5
Scenario 6
Scenario 7
sea level, m
Time after the earthquake, min

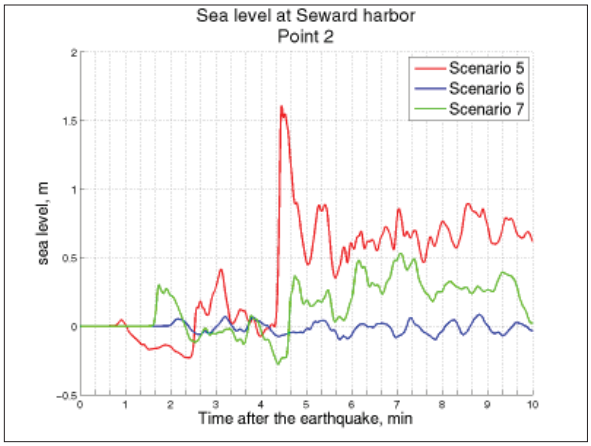
Sea level at Seward harbor
Point 2
Scenario 5
Scenario 6
Scenario 7
sea level, m
Time after the earthquake, min

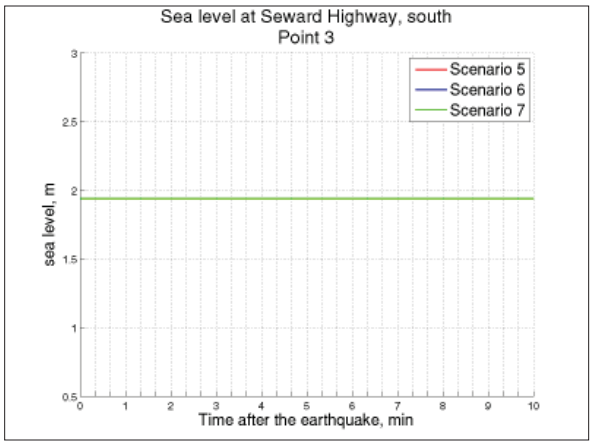
Sea level at Seward Highway, south
Point 3
Scenario 5
Scenario 6
Scenario 7
sea level, m
Time after the earthquake, min

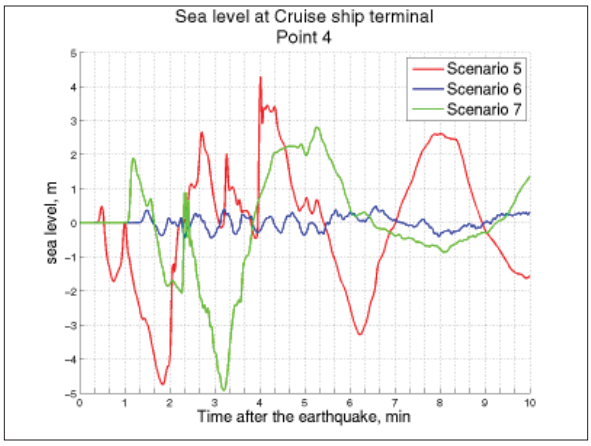
Sea level at Cruise ship terminal
Point 4
Scenario 5
Scenario 6
Scenario 7
sea level, m
Time after the earthquake, min

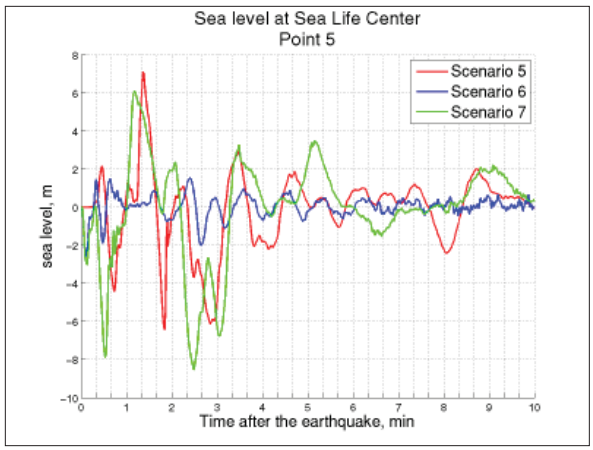
Sea level at Sea Life Center
Point 5
Scenario 5
Scenario 6
Scenario 7
sea level, m
Time after the earthquake, min

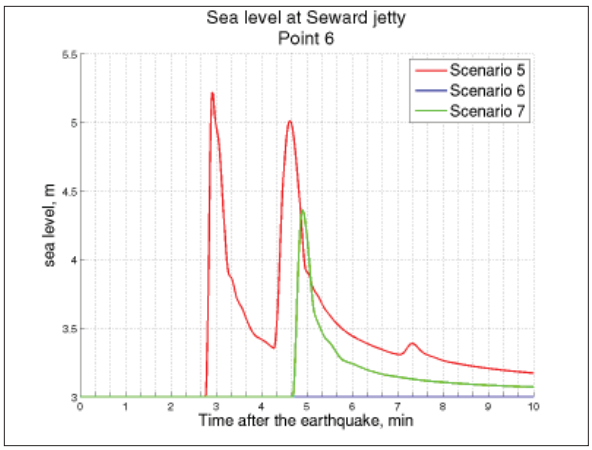
Sea level at Seward jetty
Point 6
Scenario 5
Scenario 6
Scenario 7
sea level, m
Time after the earthquake, min

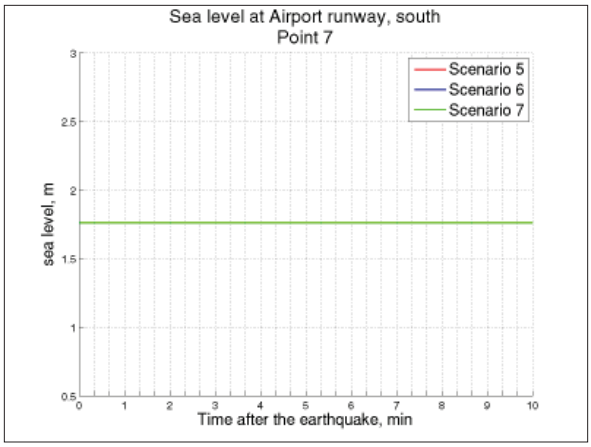
Sea level at Airport runway, south
Point 7
Scenario 5
Scenario 6
Scenario 7
sea level, m
Time after the earthquake, min

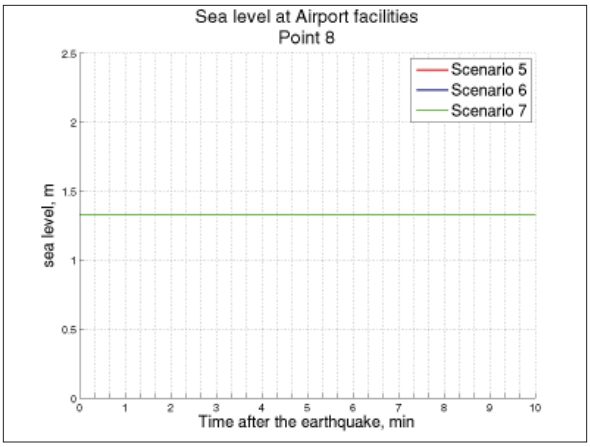
Sea level at Airport facilities
Point 8
Scenario 5
Scenario 6
Scenario 7
sea level, m
Time after the earthquake, min

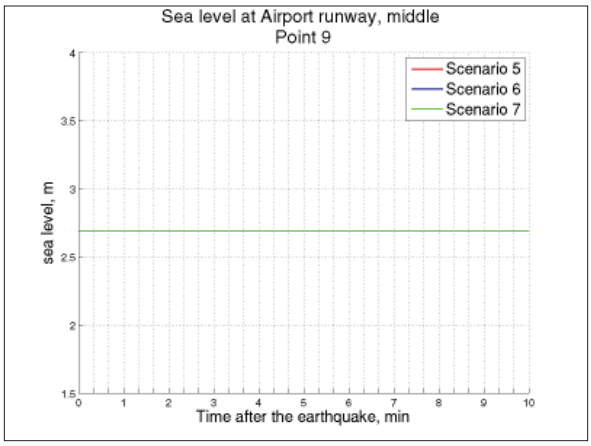
Sea level at Airport runway, middle
Point 9
Scenario 5
Scenario 6
Scenario 7
sea level, m
Time after the earthquake, min

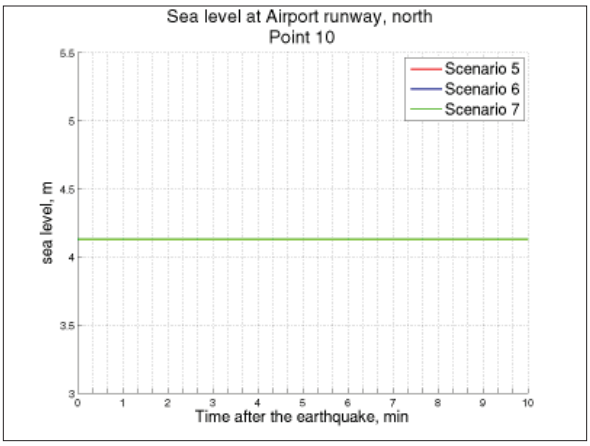
Sea level at Airport runway, north
Point 10
Scenario 5
Scenario 6
Scenario 7
sea level, m
Time after the earthquake, min

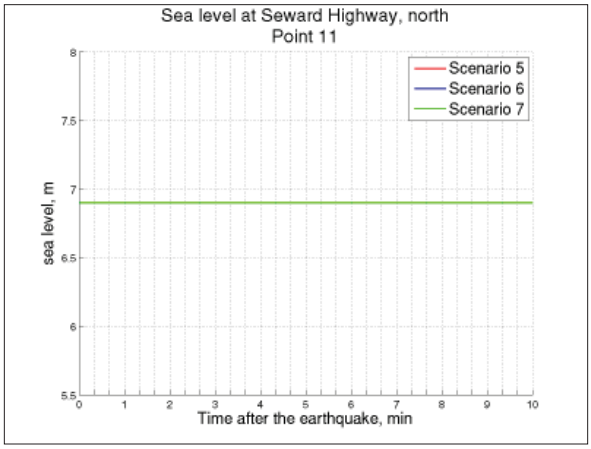
Sea level at Seward Highway, north
Point 11
Scenario 5
Scenario 6
Scenario 7
sea level, m
Time after the earthquake, min

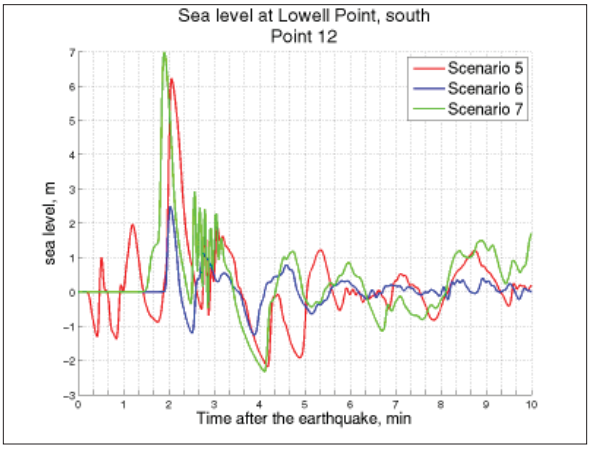
Sea level at Lowell Point, south
Point 12
Scenario 5
Scenario 6
Scenario 7
sea level, m
Time after the earthquake, min

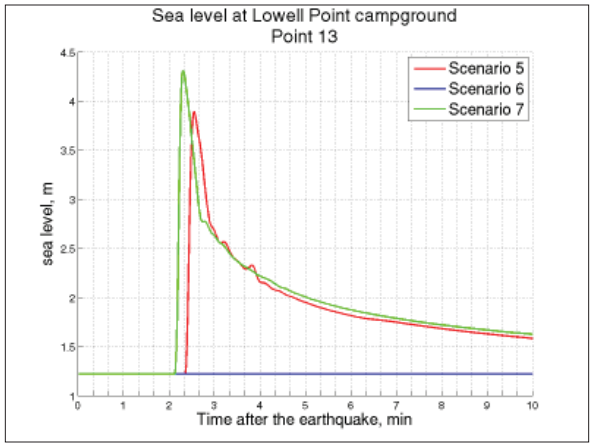
Sea level at Lowell Point campground
Point 13
Scenario 5
Scenario 6
Scenario 7
sea level, m
Time after the earthquake, min

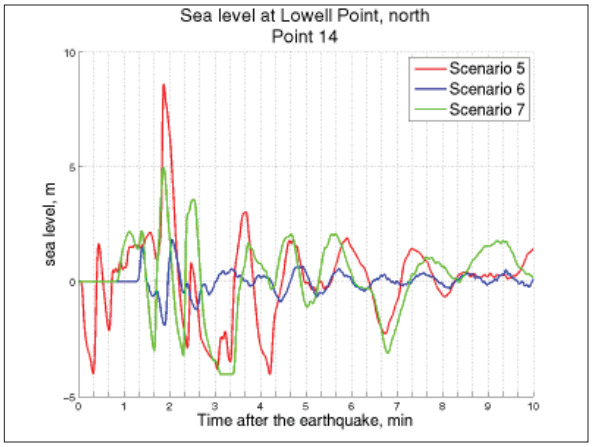
Sea level at Lowell Point, north
Point 14
Scenario 5
Scenario 6
Scenario 7
sea level, m
Time after the earthquake, min

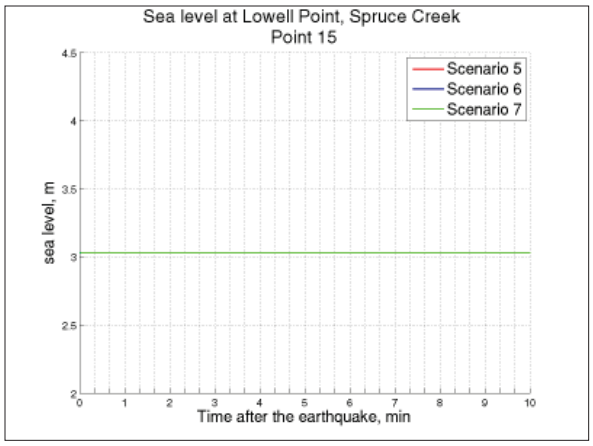
Sea level at Lowell Point, Spruce Creek
Point 15
Scenario 5
Scenario 6
Scenario 7
sea level, m
Time after the earthquake, min

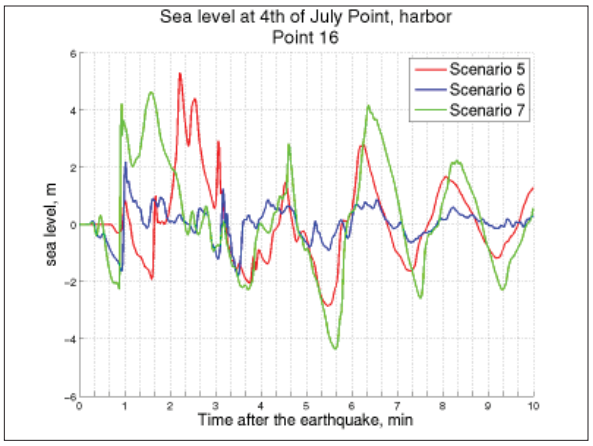
Sea level at 4th of July Point, harbor
Point 16
Scenario 5
Scenario 6
Scenario 7
sea level, m
Time after the earthquake, min

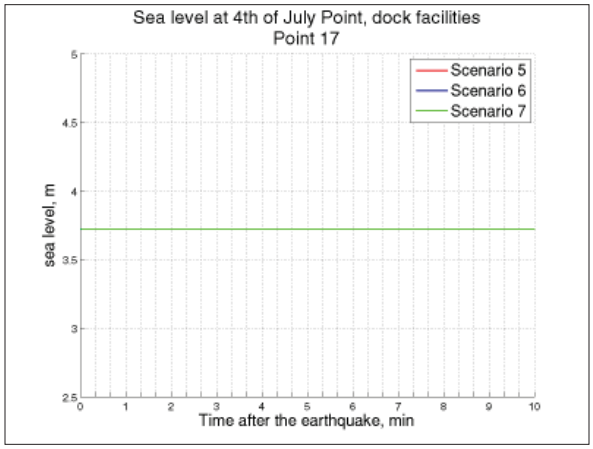
Sea level at 4th of July Point, dock facilities
Point 17
Scenario 5
Scenario 6
Scenario 7
sea level, m
Time after the earthquake, min

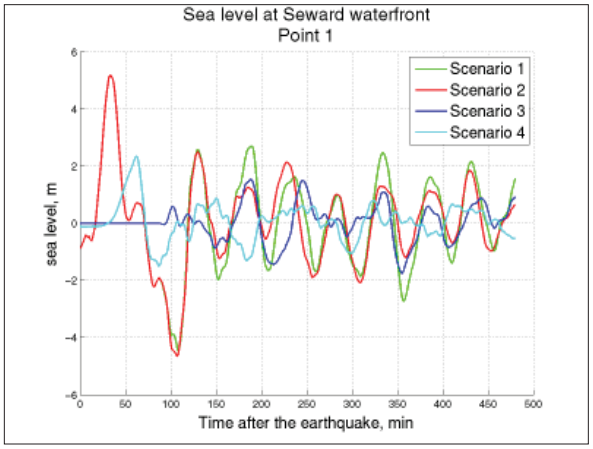
Sea level at Seward waterfront
Point 1
Scenario 1
Scenario 2
Scenario 3
Scenario 4
sea level, m
Time after the earthquake, min

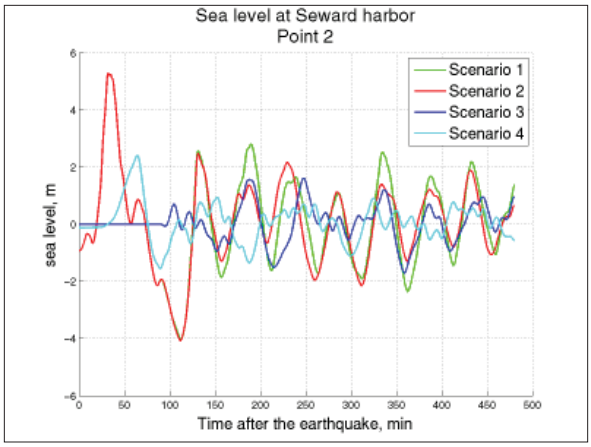
Sea level at Seward harbor
Point 2
Scenario 1
Scenario 2
Scenario 3
Scenario 4
sea level, m
Time after the earthquake, min

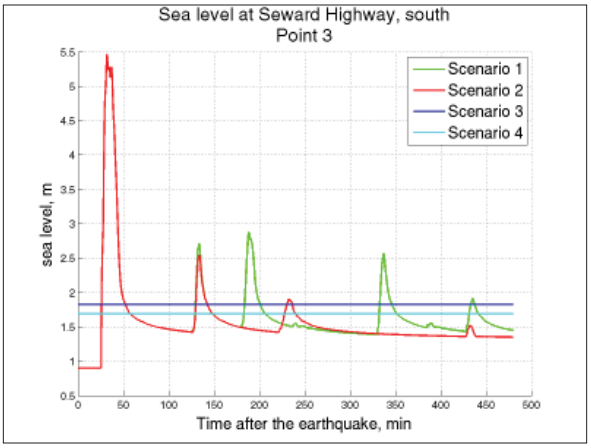
Sea level at Seward Highway, south
Point 3
Scenario 1
Scenario 2
Scenario 3
Scenario 4
sea level, m
Time after the earthquake, min

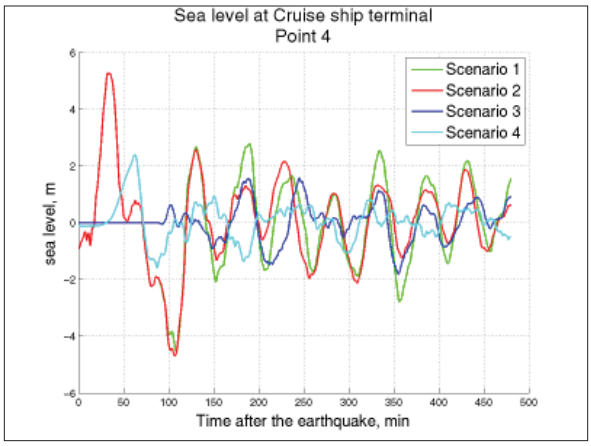
Sea level at Cruise ship terminal
Point 4
Scenario 1
Scenario 2
Scenario 3
Scenario 4
sea level, m
Time after the earthquake, min

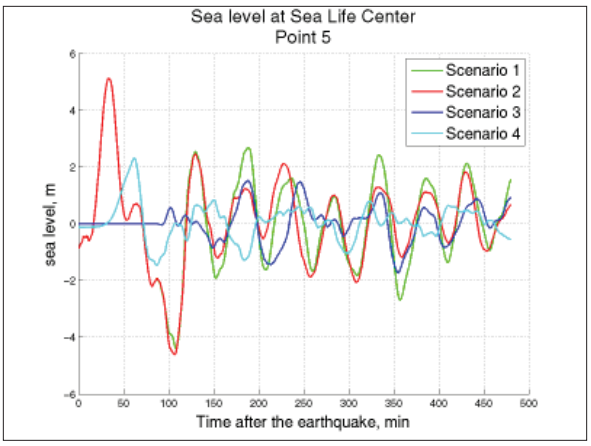
Sea level at Sea Life Center
Point 5
Scenario 1
Scenario 2
Scenario 3
Scenario 4
sea level, m
Time after the earthquake, min

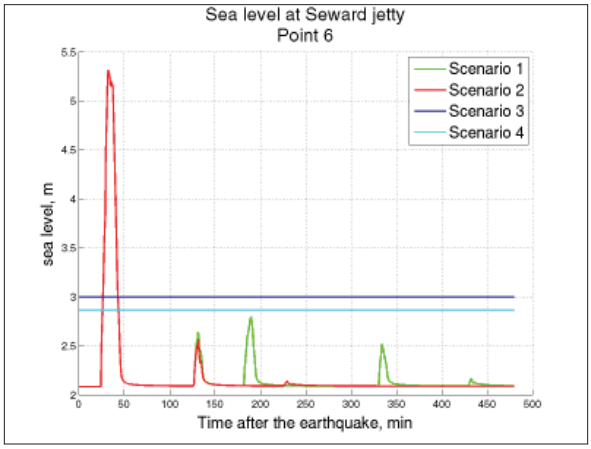
Sea level at Seward jetty
Point 6
Scenario 1
Scenario 2
Scenario 3
Scenario 4
sea level, m
Time after the earthquake, min

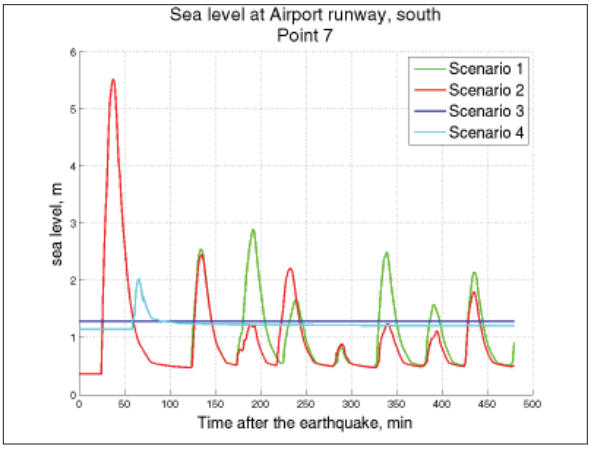
Sea level at Airport runway, south
Point 7
Scenario 1
Scenario 2
Scenario 3
Scenario 4
sea level, m
Time after the earthquake, min

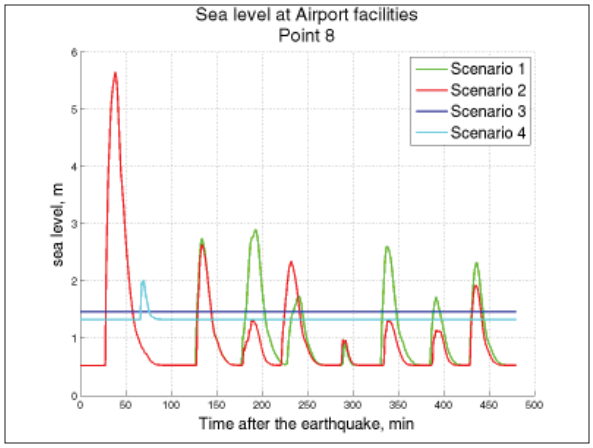
Sea level at Airport facilities
Point 8
Scenario 1
Scenario 2
Scenario 3
Scenario 4
sea level, m
Time after the earthquake, min

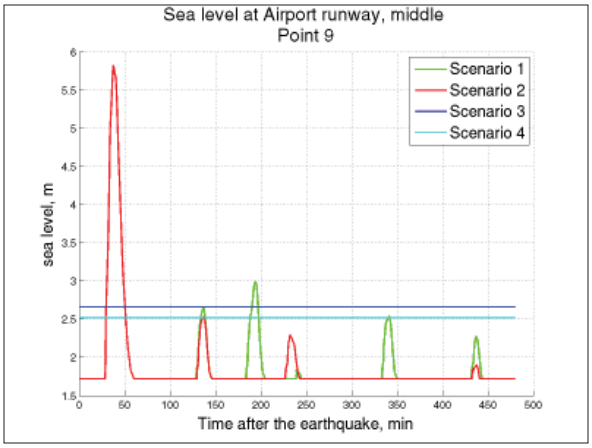
Sea level at Airport runway, middle
Point 9
Scenario 1
Scenario 2
Scenario 3
Scenario 4
sea level, m
Time after the earthquake, min

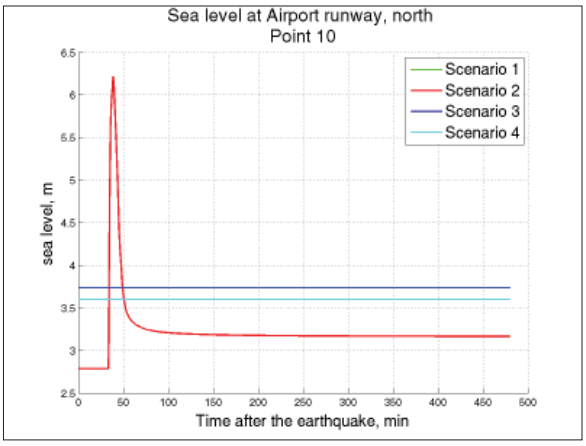
Sea level at Airport runway, north
Point 10
Scenario 1
Scenario 2
Scenario 3
Scenario 4
sea level, m
Time after the earthquake, min

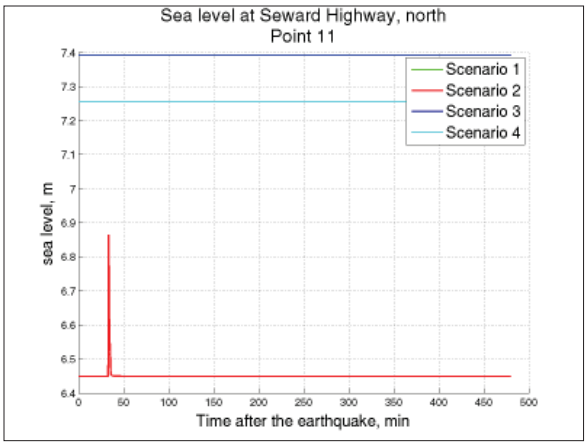
Sea level at Seward Highway, north
Point 11
Scenario 1
Scenario 2
Scenario 3
Scenario 4
sea level, m
Time after the earthquake, min

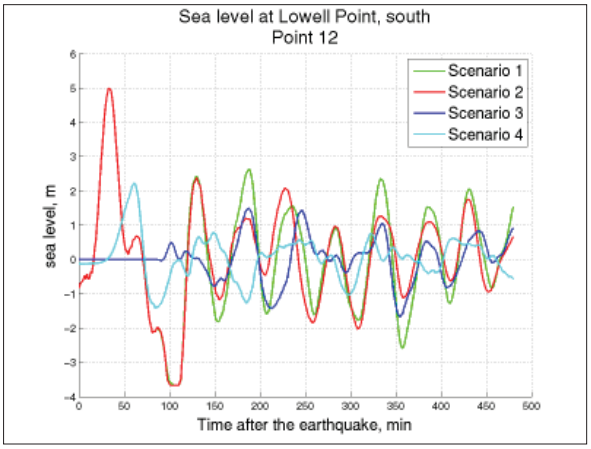
Sea level at Lowell Point, south
Point 12
Scenario 1
Scenario 2
Scenario 3
Scenario 4
sea level, m
Time after the earthquake, min

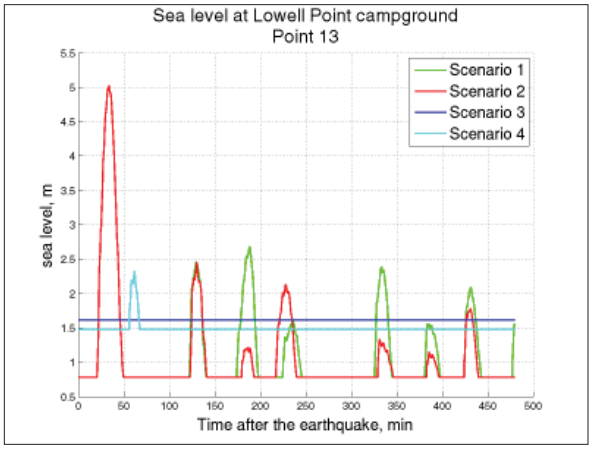
Sea level at Lowell Point campground
Point 13
Scenario 1
Scenario 2
Scenario 3
Scenario 4
sea level, m
Time after the earthquake, min

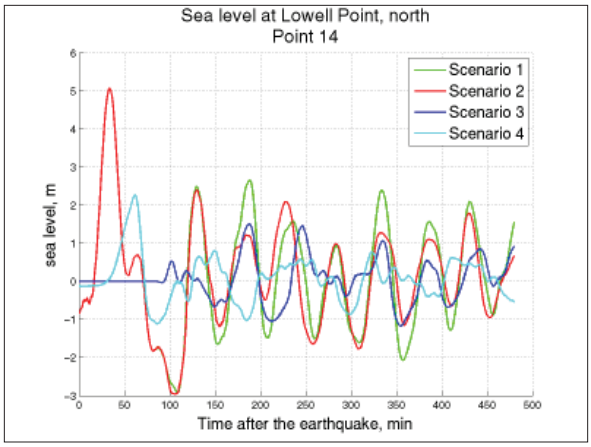
Sea level at Lowell Point, north
Point 14
Scenario 1
Scenario 2
Scenario 3
Scenario 4
sea level, m
Time after the earthquake, min

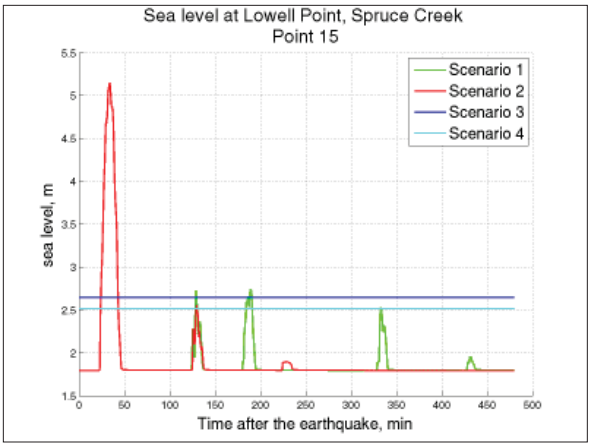
Sea level at Lowell Point, Spruce Creek
Point 15
Scenario 1
Scenario 2
Scenario 3
Scenario 4
sea level, m
Time after the earthquake, min

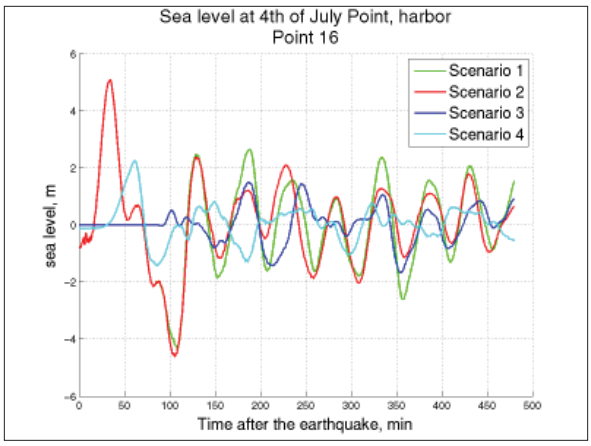
Sea level at 4th of July Point, harbor
Point 16
Scenario 1
Scenario 2
Scenario 3
Scenario 4
sea level, m
Time after the earthquake, min

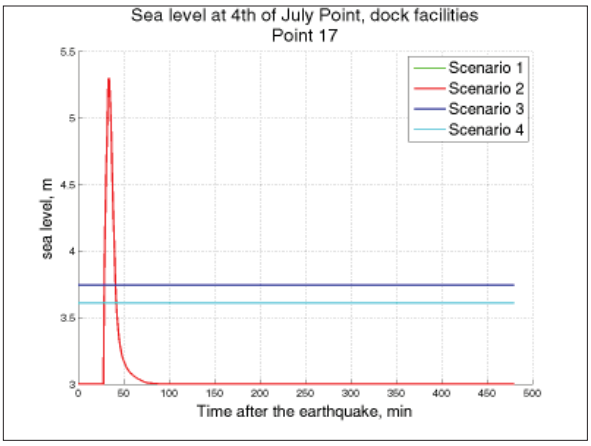
Sea level at 4th of July Point, dock facilities
Point 17
Scenario 1
Scenario 2
Scenario 3
Scenario 4
sea level, m
Time after the earthquake, min

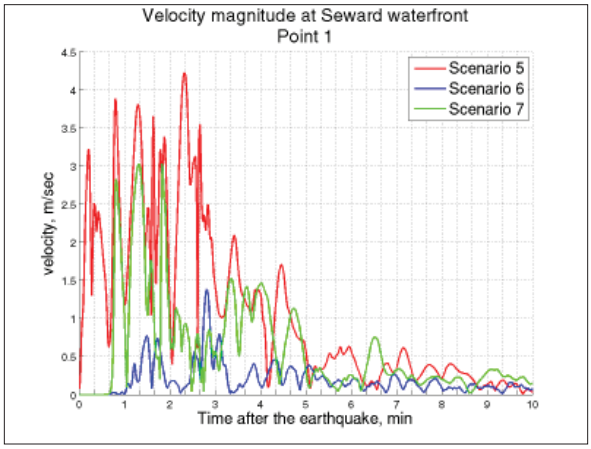
Velocity magnitude at Seward waterfront
Point 1
Scenario 5
Scenario 6
Scenario 7
velocity, m/sec
Time after the earthquake, min

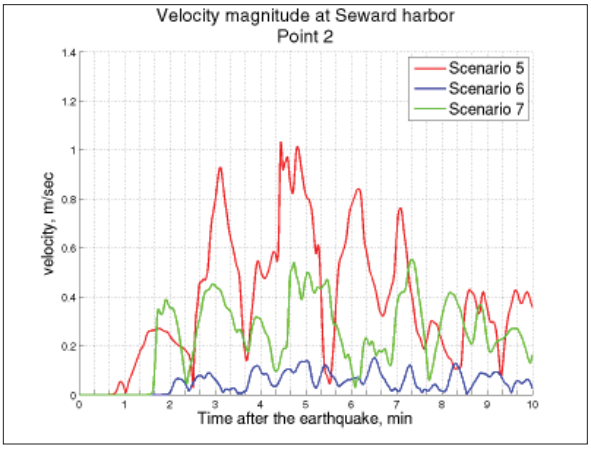
Velocity magnitude at Seward harbor
Point 2
Scenario 5
Scenario 6
Scenario 7
velocity, m/sec
Time after the earthquake, min

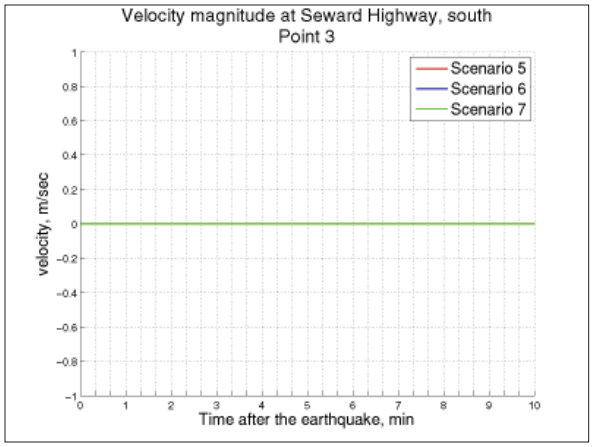
Velocity magnitude at Seward Highway, south
Point 3
Scenario 5
Scenario 6
Scenario 7
velocity, m/sec
Time after the earthquake, min

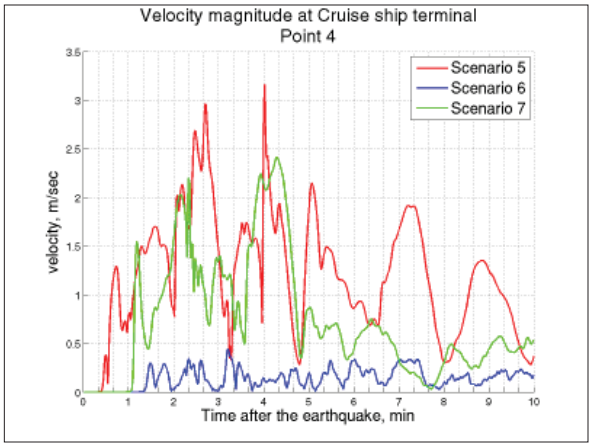
Velocity magnitude at Cruise ship terminal
Point 4
Scenario 5
Scenario 6
Scenario 7
velocity, m/sec
Time after the earthquake, min

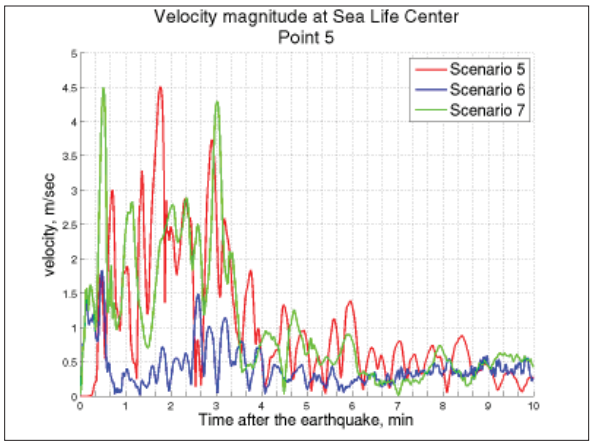
Velocity magnitude at Sea Life Center
Point 5
Scenario 5
Scenario 6
Scenario 7
velocity, m/sec
Time after the earthquake, min

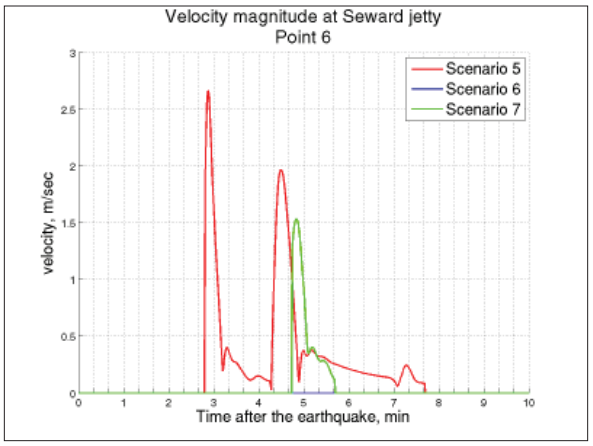
Velocity magnitude at Seward jetty
Point 6
Scenario 5
Scenario 6
Scenario 7
velocity, m/sec
Time after the earthquake, min

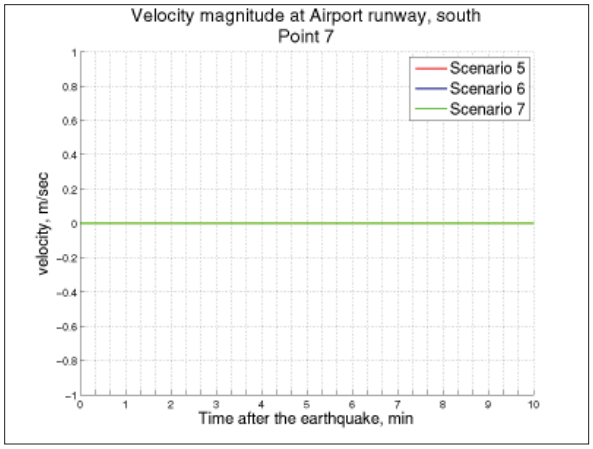
Velocity magnitude at Airport runway, south
Point 7
Scenario 5
Scenario 6
Scenario 7
velocity, m/sec
Time after the earthquake, min

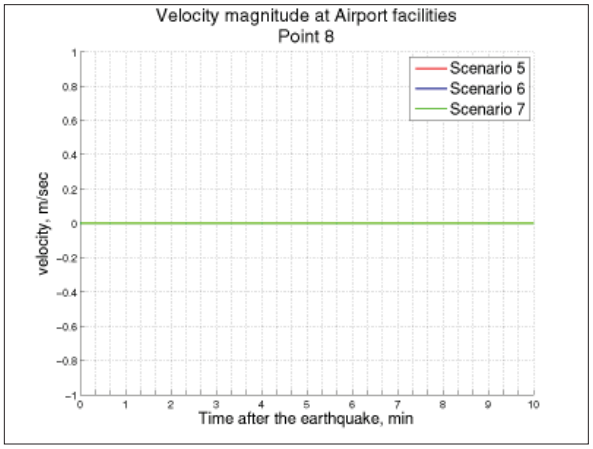
Velocity magnitude at Airport facilities
Point 8
Scenario 5
Scenario 6
Scenario 7
velocity, m/sec
Time after the earthquake, min

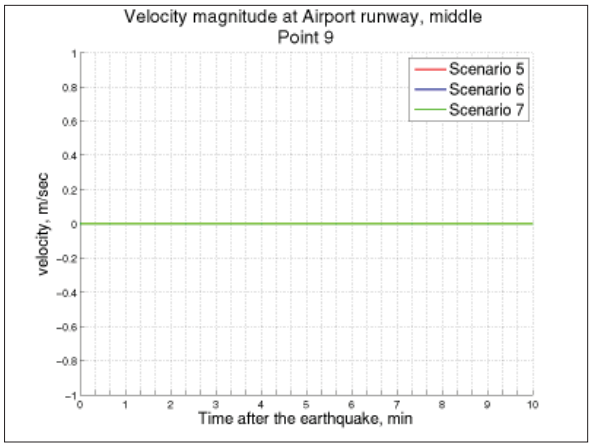
Velocity magnitude at Airport runway, middle
Point 9
Scenario 5
Scenario 6
Scenario 7
velocity, m/sec
Time after the earthquake, min

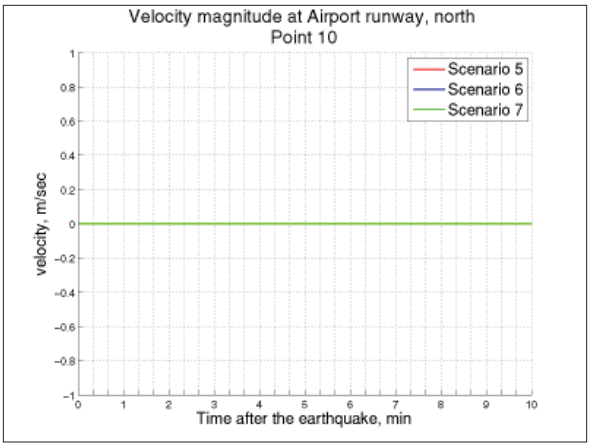
Velocity magnitude at Airport runway, north
Point 10
Scenario 5
Scenario 6
Scenario 7
velocity, m/sec
Time after the earthquake, min

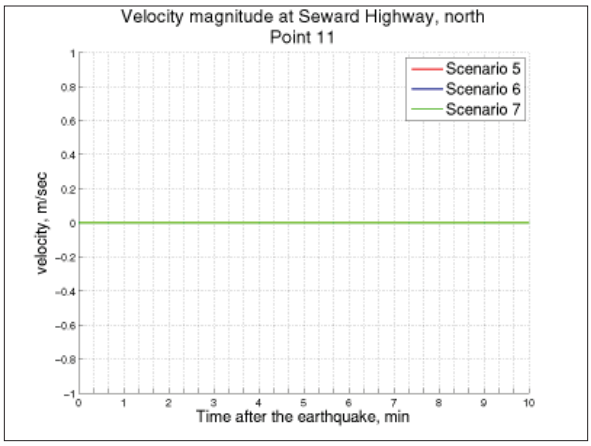
Velocity magnitude at Seward Highway, north
Point 11
Scenario 5
Scenario 6
Scenario 7
velocity, m/sec
Time after the earthquake, min

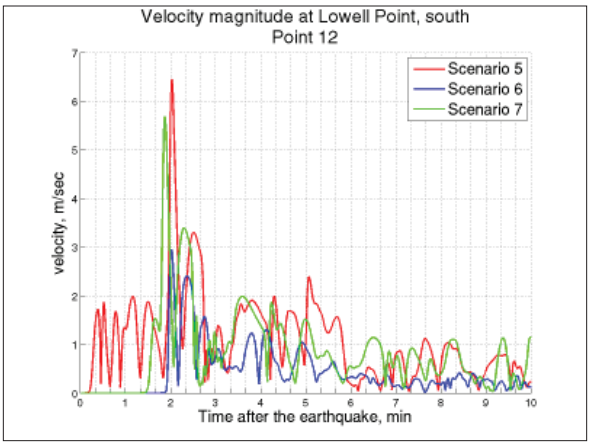
Velocity magnitude at Lowell Point, south
Point 12
Scenario 5
Scenario 6
Scenario 7
velocity, m/sec
Time after the earthquake, min

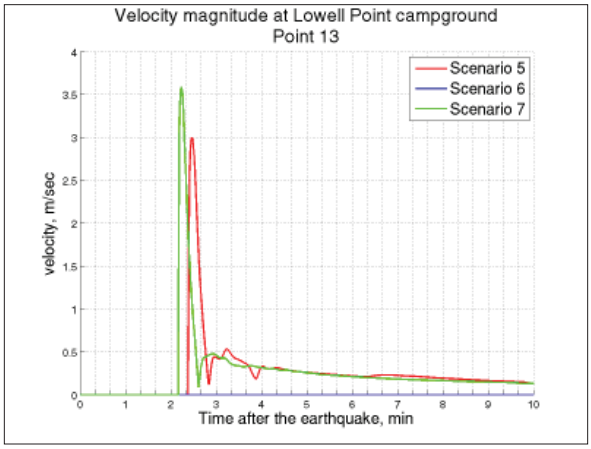
Velocity magnitude at Lowell Point campground
Point 13
Scenario 5
Scenario 6
Scenario 7
velocity, m/sec
Time after the earthquake, min

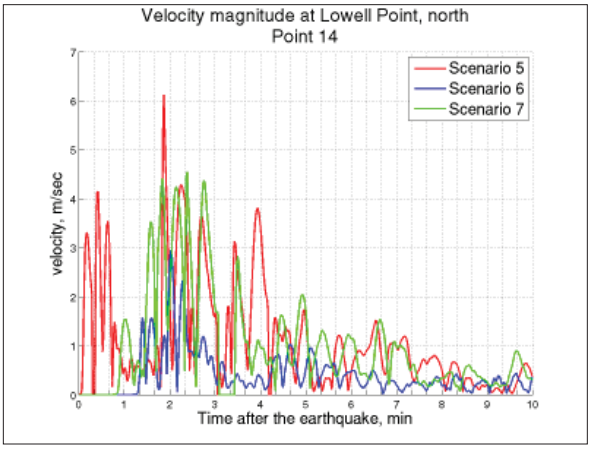
Velocity magnitude at Lowell Point, north
Point 14
Scenario 5
Scenario 6
Scenario 7
velocity, m/sec
Time after the earthquake, min

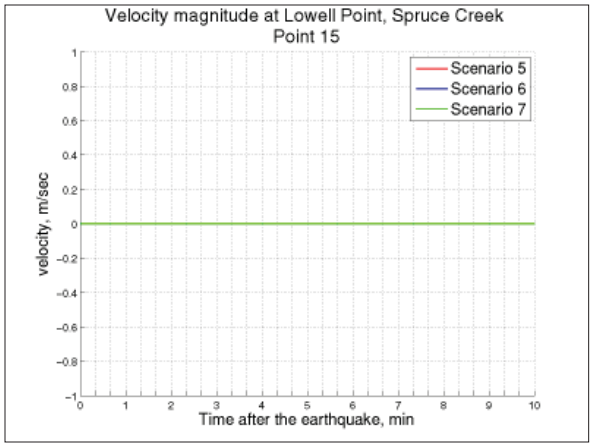
Velocity magnitude at Lowell Point, Spruce Creek
Point 15
Scenario 5
Scenario 6
Scenario 7
velocity, m/sec
Time after the earthquake, min

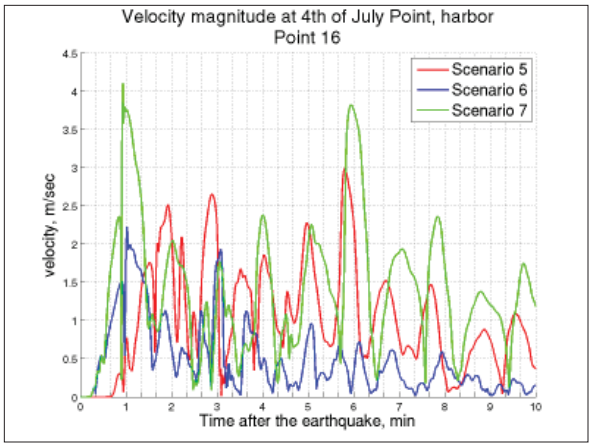
Velocity magnitude at 4th of July Point, harbor
Point 16
Scenario 5
Scenario 6
Scenario 7
velocity, m/sec
Time after the earthquake, min

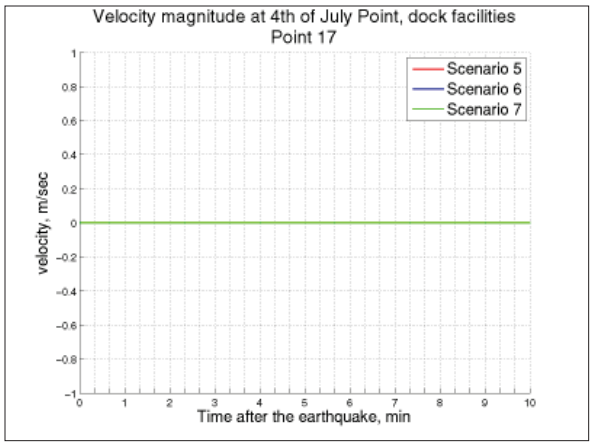
Velocity magnitude at 4th of July Point, dock facilities
Point 17
Scenario 5
Scenario 6
Scenario 7
velocity, m/sec
Time after the earthquake, min

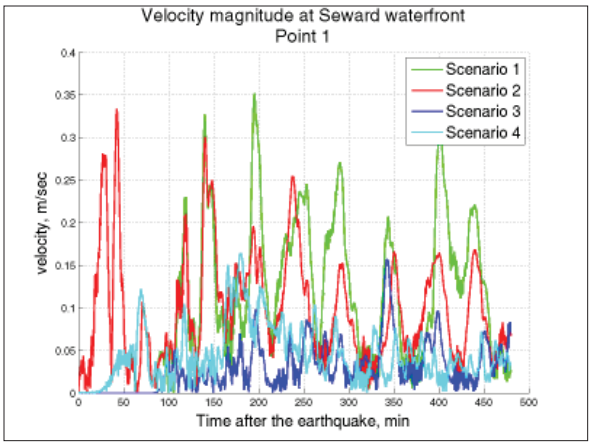
Velocity magnitude at Seward waterfront
Point 1
Scenario 1
Scenario 2
Scenario 3
Scenario 4
velocity, m/sec
Time after the earthquake, min

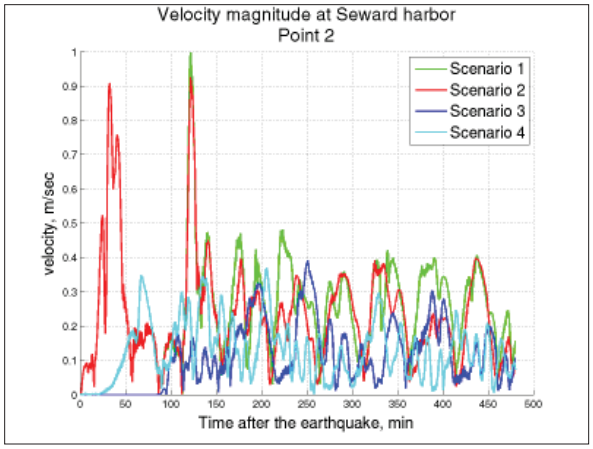
Velocity magnitude at Seward harbor
Point 2
Scenario 1
Scenario 2
Scenario 3
Scenario 4
velocity, m/sec
Time after the earthquake, min

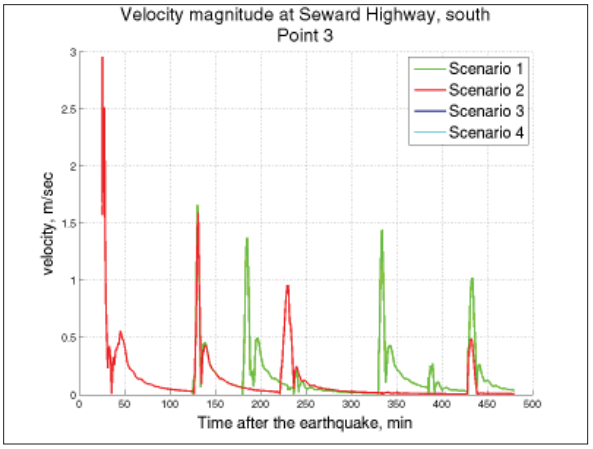
Velocity magnitude at Seward Highway, south
Point 3
Scenario 1
Scenario 2
Scenario 3
Scenario 4
velocity, m/sec
Time after the earthquake, min

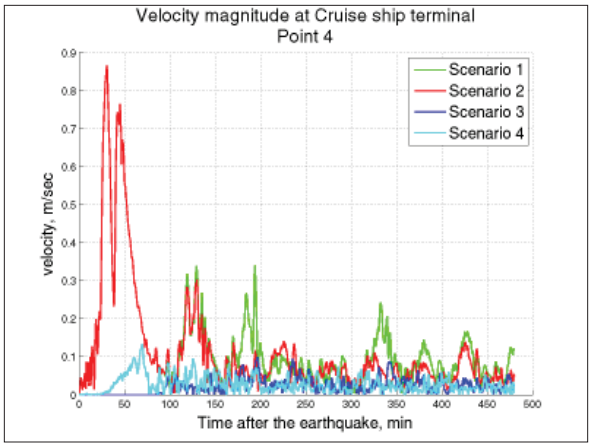
Velocity magnitude at Cruise ship terminal
Point 4
Scenario 1
Scenario 2
Scenario 3
Scenario 4
velocity, m/sec
Time after the earthquake, min

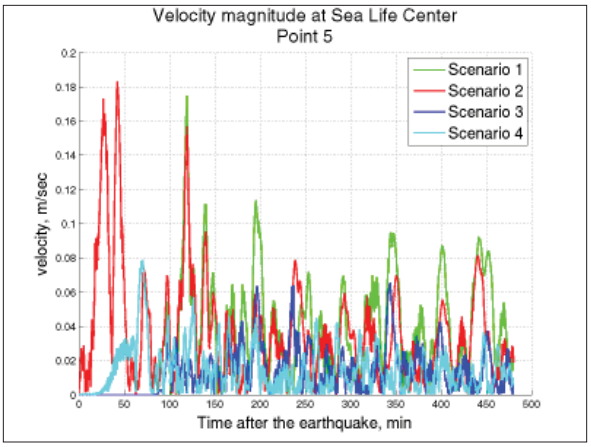
Velocity magnitude at Sea Life Center
Point 5
Scenario 1
Scenario 2
Scenario 3
Scenario 4
velocity, m/sec
Time after the earthquake, min

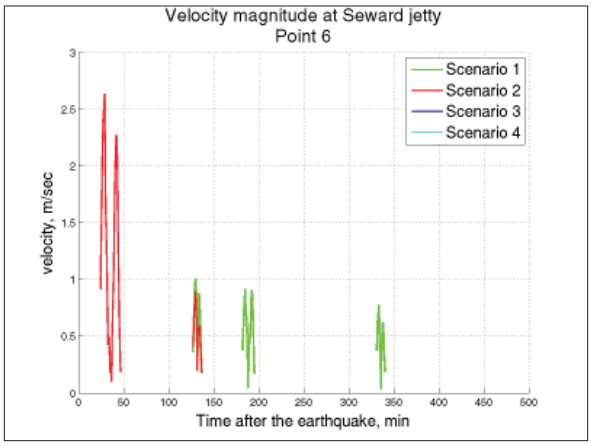
Velocity magnitude at Seward jetty
Point 6
Scenario 1
Scenario 2
Scenario 3
Scenario 4
velocity, m/sec
Time after the earthquake, min

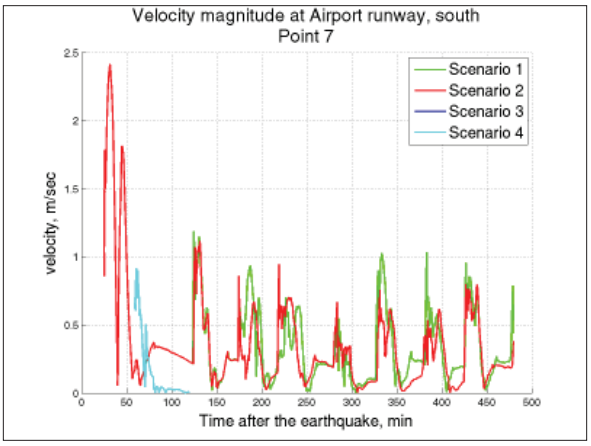
Velocity magnitude at Airport runway, south
Point 7
Scenario 1
Scenario 2
Scenario 3
Scenario 4
velocity, m/sec
Time after the earthquake, min

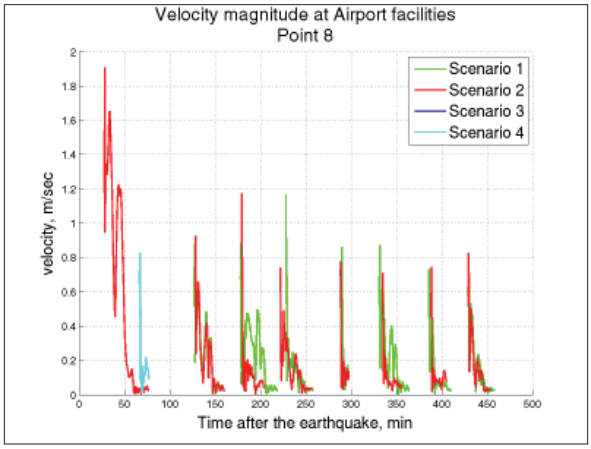
Velocity magnitude at Airport facilities
Point 8
Scenario 1
Scenario 2
Scenario 3
Scenario 4
velocity, m/sec
Time after the earthquake, min

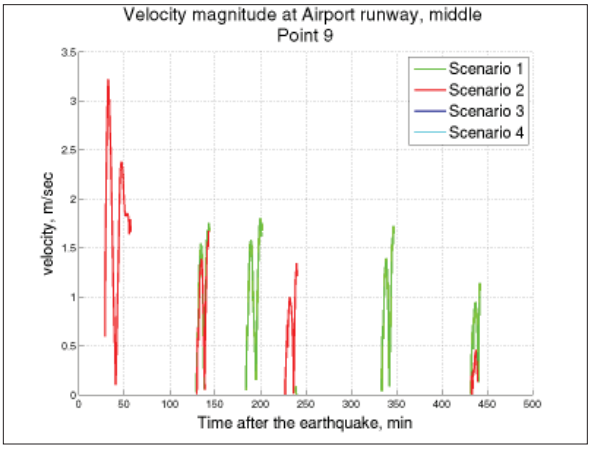
Velocity magnitude at Airport runway, middle
Point 9
Scenario 1
Scenario 2
Scenario 3
Scenario 4
velocity, m/sec
Time after the earthquake, min

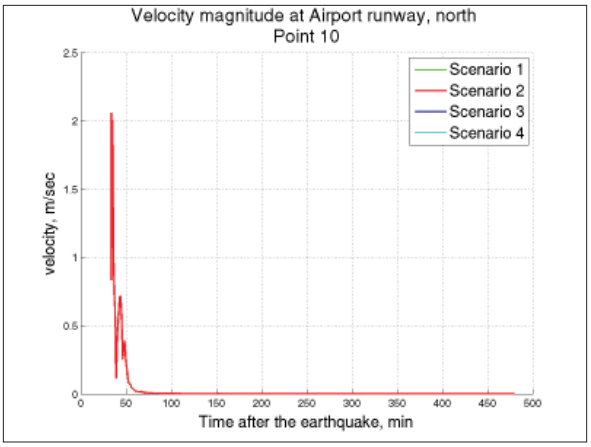
Velocity magnitude at Airport runway, north
Point 10
Scenario 1
Scenario 2
Scenario 3
Scenario 4
velocity, m/sec
Time after the earthquake, min

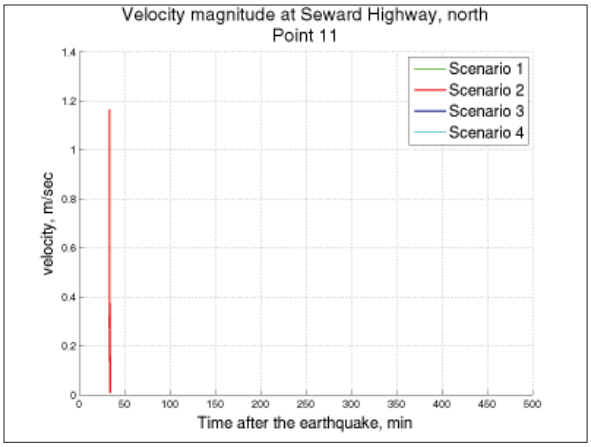
Velocity magnitude at Seward Highway, north
Point 11
Scenario 1
Scenario 2
Scenario 3
Scenario 4
velocity, m/sec
Time after the earthquake, min

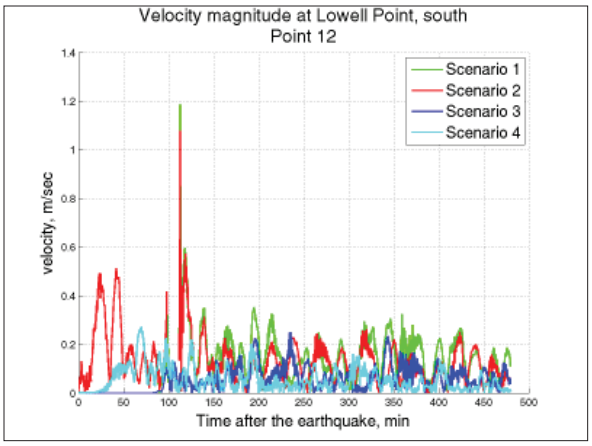
Velocity magnitude at Lowell Point, south
Point 12
Scenario 1
Scenario 2
Scenario 3
Scenario 4
velocity, m/sec
Time after the earthquake, min

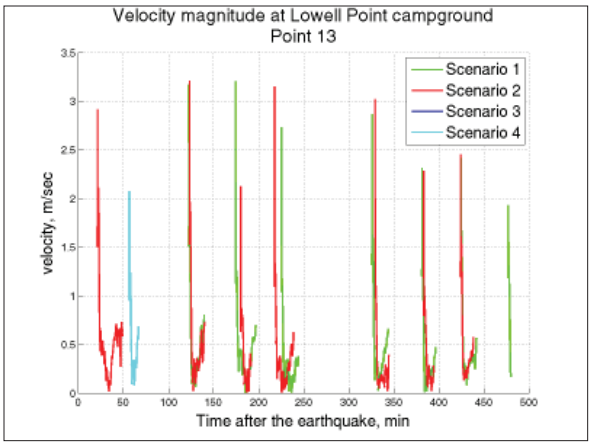
Velocity magnitude at Lowell Point campground
Point 13
Scenario 1
Scenario 2
Scenario 3
Scenario 4
velocity, m/sec
Time after the earthquake, min

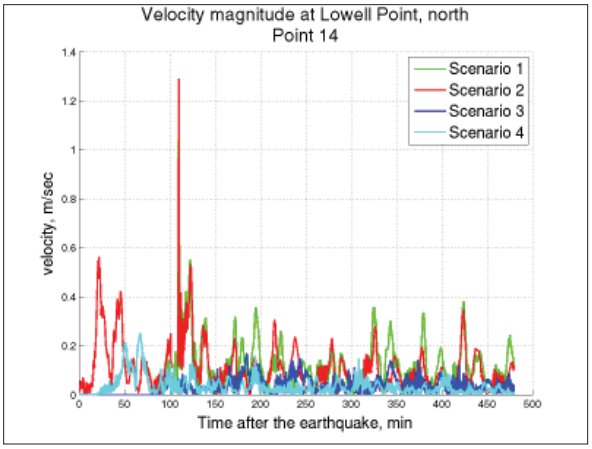
Velocity magnitude at Lowell Point, north
Point 14
Scenario 1
Scenario 2
Scenario 3
Scenario 4
velocity, m/sec
Time after the earthquake, min

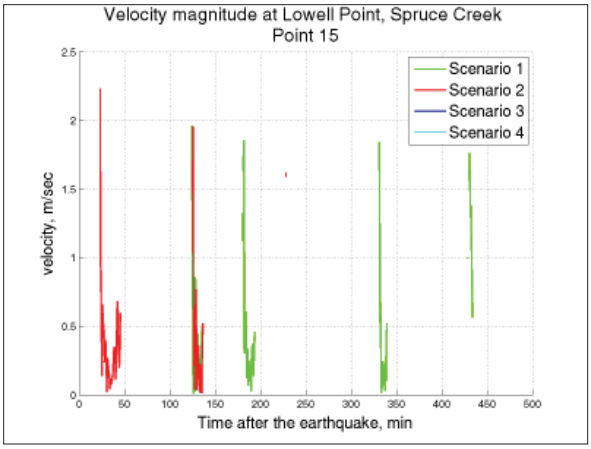
Velocity magnitude at Lowell Point, Spruce Creek
Point 15
Scenario 1
Scenario 2
Scenario 3
Scenario 4
velocity, m/sec
Time after the earthquake, min

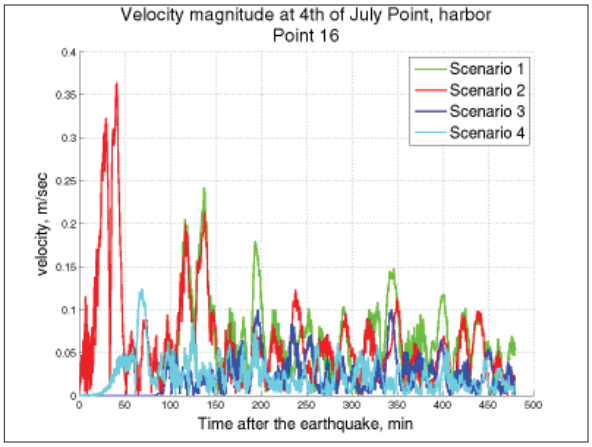
Velocity magnitude at 4th of July Point, harbor
Point 16
Scenario 1
Scenario 2
Scenario 3
Scenario 4
velocity, m/sec
Time after the earthquake, min

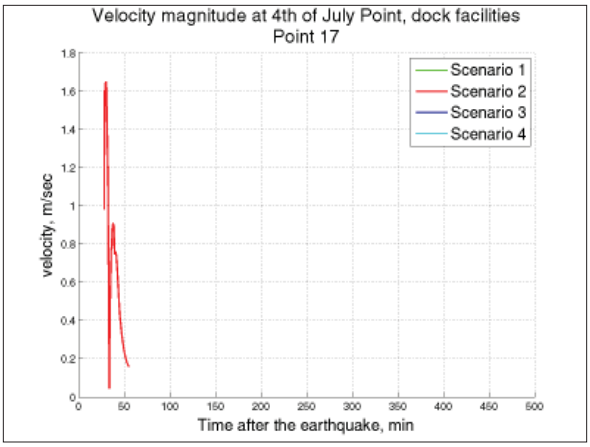
Velocity magnitude at 4th of July Point, dock facilities
Point 17
Scenario 1
Scenario 2
Scenario 3
Scenario 4
velocity, m/sec
Time after the earthquake, min